
Masters Theses

Student Theses and Dissertations

Spring 2016

Reprocessing and structural interpretation of multichannel seismic reflection data from Penobscot, Nova Scotia

Fulya Gizem Yagci

Follow this and additional works at: https://scholarsmine.mst.edu/masters_theses



Part of the [Geophysics and Seismology Commons](#)

Department:

Recommended Citation

Yagci, Fulya Gizem, "Reprocessing and structural interpretation of multichannel seismic reflection data from Penobscot, Nova Scotia" (2016). *Masters Theses*. 7528.

https://scholarsmine.mst.edu/masters_theses/7528

This thesis is brought to you by Scholars' Mine, a service of the Missouri S&T Library and Learning Resources. This work is protected by U. S. Copyright Law. Unauthorized use including reproduction for redistribution requires the permission of the copyright holder. For more information, please contact scholarsmine@mst.edu.

REPROCESSING AND STRUCTURAL INTERPRETATION OF MULTICHANNEL
SEISMIC REFLECTION DATA FROM PENOBSCOT, NOVA SCOTIA

by

FULYA GIZEM YAGCI

A THESIS

Presented to the Faculty of the Graduate School of the
MISSOURI UNIVERSITY OF SCIENCE AND TECHNOLOGY

In Partial Fulfillment of the Requirements for the Degree

MASTER OF SCIENCE IN GEOLOGY AND GEOPHYSICS

2016

Approved by

Stephen S. Gao, Advisor

Kelly H. Liu, Co-advisor

Wan Yang

© 2016

FULYA GIZEM YAGCI

All Rights Reserved

ABSTRACT

Penobscot area is located in the Scotian Basin, which was occurred as a result of extension in the eastern North America border. 2-D data set that was utilized for the study consists of three multichannel seismic profiles that were collected from Penobscot Parcel 8. The main purpose of the study was to enhance signal-to-noise ratio of the seismic reflection sections suppressing low and high frequency noise and multiples, and removing diffractions. In addition, while the resolution of the sections were enhanced, determining the correct processing techniques and parameters for better results was the another important criteria.

The processing steps included deconvolution, minimum phase filter, velocity analysis, NMO correction, stacking, Stolt and Gazdag migrations, band-pass and slope filters, and muting. The resolution of the seismic sections was increased using pre-stack spiking deconvolution and prediction error filter techniques. The low amplitude problem at the sea bottom reflections were recovered using the Butterworth minimum phase filter. Random noise were eliminated using band-pass and f-k dip filter. Stolt and Gazdag migrations were compared. Because Gazdag migration collapsed the diffractions at the shallow and deeper parts of the seismic sections at the same time and provided a better resolution for long dipping geological structures, the results of Gazdag were utilized for structural interpretation.

ACKNOWLEDGMENTS

I would like to thank Dr. Stephen Gao and Dr. Kelly Liu for their support and positive reinforcement during my study. I also thank Dr. Wan Yang, who is also my committee member, for his suggestions.

I am really grateful to my sponsors, Turkish Petroleum Corporation (TPAO) and Turkish Ministry of National Education. I had the chance to pursue my education in geology and geophysics in the USA because they provided this opportunity.

I would like to acknowledge Canada-Nova Scotia Offshore Petroleum Board for the Penobscot 2-D data set, which was used for the study. I thank Aamer Alhakem for the data set.

Thanks to Amy Ketterer who helped me to edit the language of this study and to improve the influence of the research.

I thank my husband Gorkem Yagci with my whole heart. He always looked out for me and treated me with great love and patience. I also thank my mother and father, Suzan Oztoplu and Yalcin Oztoplu, for their support and motivation.

DEDICATION

Dedicated to my grandmother and grandfather...

I will never forget them for their love and caring since my childhood.

TABLE OF CONTENTS

	Page
ABSTRACT.....	iii
ACKNOWLEDGMENTS	iv
DEDICATION.....	v
LIST OF ILLUSTRATIONS.....	viii
LIST OF TABLES.....	x
NOMENCLATURE	xi
SECTION	
1. INTRODUCTION.....	1
1.1. AREA OF STUDY	1
1.2. OBJECTIVES.....	4
2. GEOLOGY.....	5
2.1. GEOLOGICAL EVOLUTION OF THE SCOTIAN BASIN	5
2.2. TECTONIC DEVELOPMENT	14
3. DATA.....	17
3.1. DATA INFORMATION	17
3.1.1. Seismic Data.....	17
3.1.2. Well Data.....	20
4. PROCESSING METHODS	22
4.1.CONVENTION SEG Y TO SU	22
4.2. BUTTERWORTH FILTER.....	22
4.3. SPIKING DECONVOLUTION AND PREDICTION ERROR FILTER	26
4.3.1. Spiking Deconvolution.....	29
4.3.2. Prediction Error Filter (Predictive Deconvolution, PEF).....	29
4.3.3. Autocorrelation.....	29
4.4. VELOCITY ANALYSIS	36
4.5. NMO CORRECTION.....	38
4.6. STACKING	40
4.7. MIGRATION.....	44

4.7.1. The Frequency Wavenumber (f-k) Method.....	44
4.7.1.1. Stolt migration	47
4.7.1.2. Gazdag (phase shift) migration.....	49
4.8. BAND-PASS ZERO PHASE FILTER AND SLOPE FILTER	59
4.9. RMS AMPLITUDE AUTOMATIC GAIN CONTROL	65
4.10. MUTING.....	67
5. STRUCTURAL INTERPRETATION.....	73
5.1. PROCEDURE.....	73
5.2. GENERATION OF THE SYNTHETIC SEISMOGRAM AND MATCHING.....	74
5.3. HORIZON INTERPRETATION.....	74
5.4. FAULT INTERPRETATION.....	76
5.5. ATTRIBUTE ANALYSIS.....	80
5.5.1. Variance (Edge Method)	81
5.5.2. Instantaneous Phase.....	81
6. CONCLUSIONS AND RECOMMENDATIONS.....	87
BIBLIOGRAPHY	90
VITA	95

LIST OF ILLUSTRATIONS

Figure	Page
1.1. Location map of the Scotian basin.....	2
1.2. The structural map of the Scotian Basin.....	3
2.1. Location map of the Scotian Basin and its borders marked with black lines	6
2.2. The present day global map of the Scotian Basin.....	7
2.3. General stratigraphy of the Scotian basin	8
2.4. Salt structures in the Scotian basin in green	9
2.5. The map of the Scotian Basin 210 million years ago.	10
2.6. The map of the Scotian Basin 150 million years ago	12
2.7. The map of the Scotian Basin 30 million years ago	14
3.1. The base map of the research area	18
4.1. The processing flow chart for Line 45.....	23
4.2. The processing flow chart for Line 46.....	24
4.3. The processing flow chart for Line 3C	25
4.4. Line 45 before and after the Butterworth filter.....	27
4.5. Amplitude spectrum of Line 45 before and after the Butterworth filter.....	27
4.6. CDP 450 from Line 45 before and after the Butterworth filter	28
4.7. Autocorrelation window of Line 45.....	32
4.8. Autocorrelation window of Line 45 before and after deconvolution	33
4.9. Velocity spectrum of CDP 450 from Line-45 before and after deconvolution	34
4.10. CDP 450 from Line 46 before and after spiking deconvolution and PEF.	35
4.11. The amplitude spectrum of Line 45 before and after deconvolution.....	36
4.12. CDP 450 velocity spectrum and its CDP gather.....	39
4.13. Three CDPs before and after NMO correction and stretching mute	40
4.14. CDP 450 from Line 45 before and after NMO correction.....	41
4.15. CDPs from Line 45 after the NMO correction.	42
4.16. Lines 3C, 45, and 46 seismic sections after stacking.....	43
4.17. Three different situation for seismic section, Line 46.	45
4.18. Diffractions in time and frequency domain	46

4.19. The migration of OB event in w-kx and kz-kx domains	47
4.20. Seismic sections with strong diffractions	51
4.21. Random noise on seismic sections after migration.....	52
4.22. Line 46 before and after the Stolt migration with a velocity of 2025 m/s	53
4.23. Gazdag and Stolt migrations of Line 46.	54
4.24. Line 3C before and after Stolt migration	55
4.25. Line 45 before and after Stolt migration (with a velocity of 2100 m/s)	56
4.26. Line 45 after Stolt migration with a velocity of 2650 m/s	57
4.27. Line 45 after the Gazdag migration	58
4.28. The frequency ranges of the noise and signal in an amplitude spectrum.	59
4.29. The frequency spectrum of Line 45	61
4.30. Band pass and f-k dip filters for Line 45.	62
4.31. Band pass and f-k dip filters in Line 3C.	63
4.32. Band pass and f-k dip filters for Line 46.	64
4.33. Trace 342 from Line 3C post-stack section before and after AGC	66
4.34. RMS amplitude AGC for Line 3C.....	68
4.35. RMS amplitude AGC for Line 45.....	69
4.36. RMS amplitude AGC for Line 46.....	70
4.37. Three seismic lines with the processing artifacts.....	71
4.38. Muted Lines 45, 46, and 3C.....	72
5.1. The base map of the study area.....	73
5.2. The synthetic seismogram and logs from Well L-30.....	75
5.3. Interpreted horizons and faults in Line 45	77
5.4. Interpreted horizons and faults in Line 46	78
5.5. Interpreted horizons and faults in Line 3C	79
5.6. Interpreted horizons and faults from Lines 45,46, and 3C	80
5.7. The variance (edge method) attribute for Line 45	82
5.8. The variance (edge method) attribute of Line 46.....	83
5.9. Instantaneous phase attribute of Line 3C.....	84
5.10. Instantaneous phase attribute of Line 45	85
5.11. Instantaneous phase attribute of Line 46	86

LIST OF TABLES

Table	Page
3.1. Header information of seismic lines.	19
3.3. Check shot data information from wells L-30 and B-41	21
4.1. Maximum and minimum autocorrelation lags of the seismic Lines 45 and 46	31

NOMENCLATURE

<u>Symbol</u>	<u>Description</u>
CDP	Common Depth Point
NMO	Normal Move-out Correction
PEF	Prediction Error Filter
Fm	Formation
SEG	Society of Exploration Geophysicists
CALI	Caliper
DENS	Density
DRHO	Bulk Density Correction
DTC	Delta-T Compressional
DTS	Delta-T Shear
GR	Gamma Ray
NEUT	Neutron
SP	Spontaneous Potential
2-D	Two Dimensional

1. INTRODUCTION

In this study, three 2-D seismic reflection lines from Penobscot Parcel 8, Nova Scotia (Figure 1.1), obtained from CNSOPB-Geoscience Research Centre (GRC), were reprocessed using the Seismic Unix software. Structural interpretation was also conducted using the Kingdom Suite 8.8 software. Seismic attributes, such as variance, instantaneous phase, were generated by Petrel 2014 software for seismic interpretation.

Knowledge about surveying and the geology background of the Scotian Basin were used to determine specific processing steps to reveal targeted geologic features, such as faults and anticlines. The main purpose of this research was to perform several processing steps, with different sequences and parameters, to better display each seismic section by enhancing the layer continuity, signal-to-noise ratio, and fault visibility.

1.1. AREA OF STUDY

The Scotian Basin, which lies in the southeast of Nova Scotia, covers the Scotian Shelf and Slope. It consists of several subbasins. From northeast to southwest, the subbasins are Laurentian, Abenaki, Sable, and Shelburne subbasins. Penobscot Parcel 8 prospect area was located at the boundary where the Abenaki Subbasin and the Sable Subbasin joint (Figure 1.2). The previous studies conducted in the Scotian Basin covered approximately 400,000 km of 2-D seismic lines and 29,000 km² of 3-D seismic data (Catuneanu, 2006). The 2-D seismic lines used for this study are 3C, 45, and 46 with lengths of 29.4 km, 11.9 km, and 11.7 km, respectively.

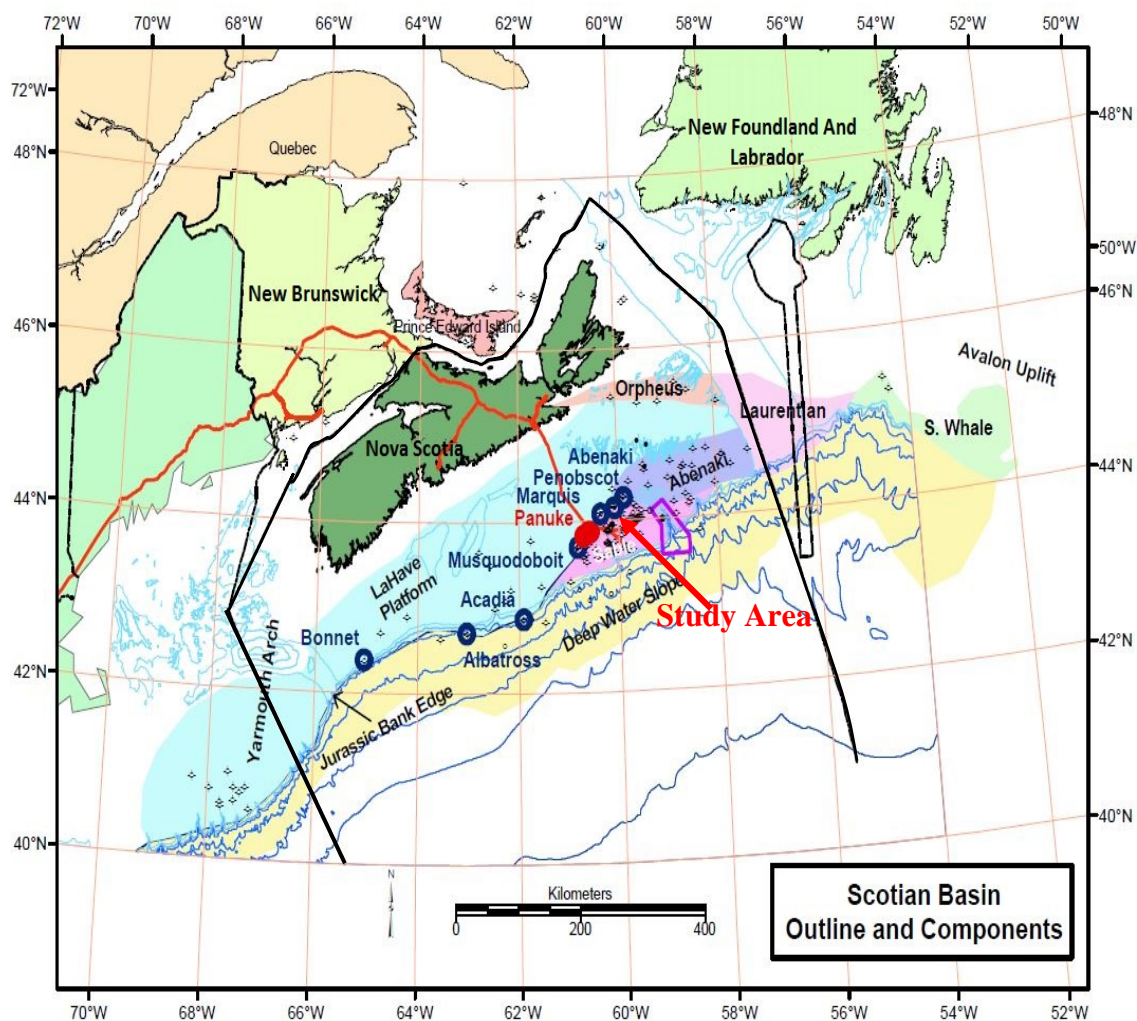


Figure 1.1. Location map of the Scotian Basin. The borders of the basin is shown with the black line (Kidston et al., 2005). Study area is marked with the red arrow.

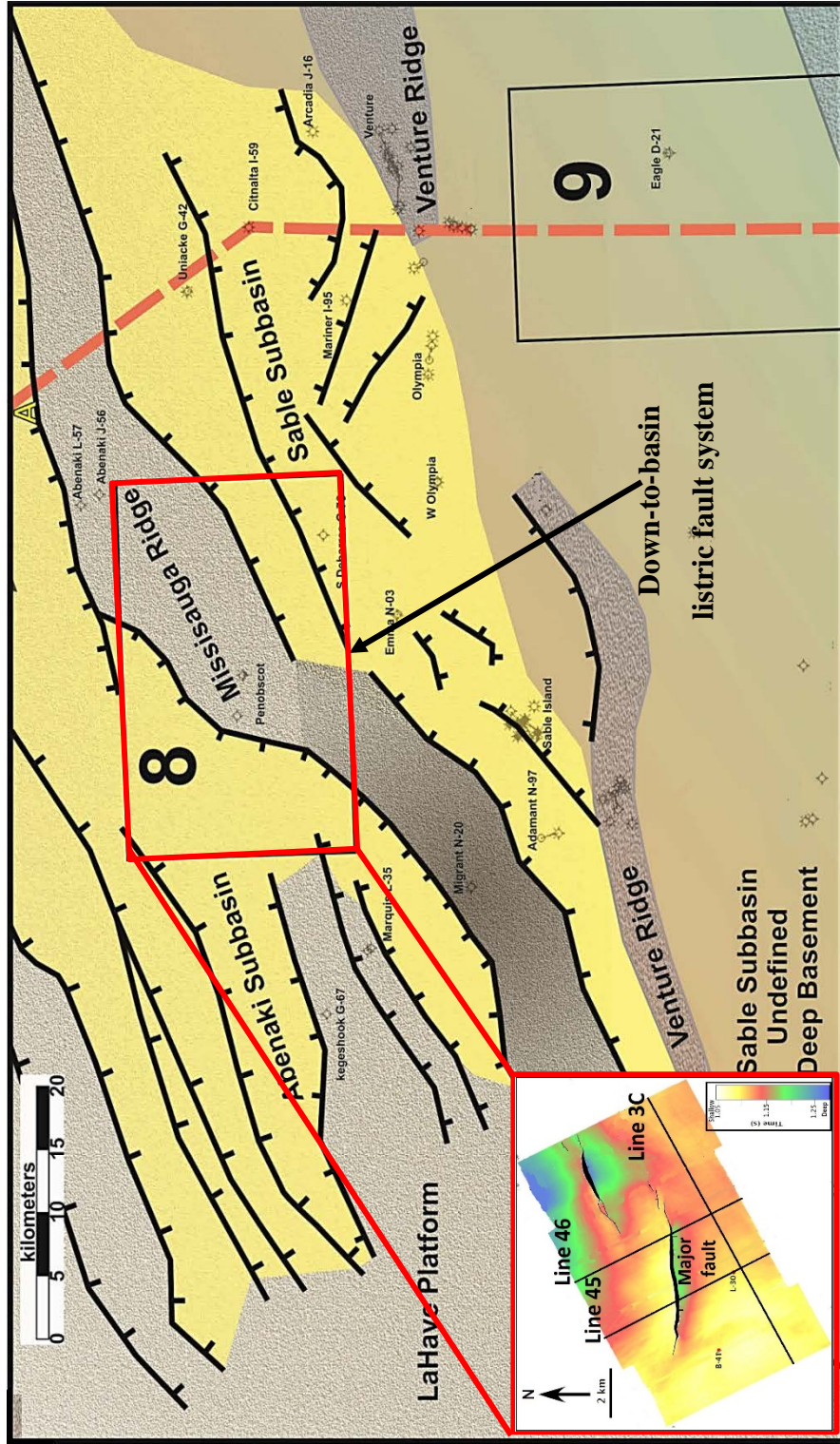


Figure 1.2. The structural map of the Scotian Basin. The research area is outlined in the rectangular box with number eight. Faults and basin hinge zones of the basin were also indicated in the figure. The wells and 2-D seismic profiles were located in the area between the Abenaki Subbasin and the Sable Subbasin and on the Mississauga Ridge (modified from Smith et al., 2015; modified from Etikha, 2012).

1.2 OBJECTIVES

Three 2-D seismic reflection profiles were acquired from the CNSOPB-Geoscience Research Centre (GRC) to conduct pre-stack and post-stack processing and to interpret the data in terms of structural features. Seismic UNIX, an open source software, was used to determine the processing sequence. Kingdom Suite 8.8 was used to interpret the three processed 2-D profiles to display faults and horizons, and Petrel 2014 was used to generate attributes to better display faults and layer continuity.

The aim of the research was to enhance the resolution of the seismic lines by conducting different processing sequences and parameters and to examine the importance of the order of in which the processing steps are applied. Pre-stack processing steps include the Butterworth minimum phase filter, spiking deconvolution, prediction error filter, velocity analysis, NMO correction and stacking. Post-stack processing steps include Stolt and Gazdag migration, slope filter, band-pass frequency filter, and muting. In addition, the research was interpreted using the Kingdom Suite's horizon and fault interpretation modules. The attributes, which are variance (edge method) and instantaneous phase, were generated using Petrel 2014 to better observe the major and minor faults and horizon continuity.

2. GEOLOGY

2.1 GEOLOGICAL EVOLUTION OF SCOTIAN BASIN

This study was conducted in the Scotian Basin, Nova Scotia. The basin covers approximately 300,000 km² (Hansen et al., 2004) and includes the Abenaki, Sable, Shelburne, and Laurentian subbasins. The borders of the basin span 1200 km from the Yarmouth Arch (which separates the Georges Bank Basin, located on the U.S. border, from the Scotian Basin) to Avalon uplift on the Grand Banks, United States border in the northeast (Figure 2.1). The water depth of the basin changes from 200 m to 4000 m (Colletta et al., 2011) throughout the shelf. The study area was located on the intersection of the Abenaki and Sable Subbasins and the Mississauga Ridge. Penobscot Parcel 8, in the vicinity of Sable Island, has a faultly blocked tectonic structure with highs and lows (Figure 1.2).

More than 225 million years ago, around the Middle Triassic Period, North America started to separate from the African continent and rifting had started (Figure 2.2). Before Pangea started breaking up, the Scotian Basin was positioned near the middle of Pangea. During the early Triassic Period, several tectonic forces caused lots of stress on the tectonic plates that led to the formation of grabens and extensive faults (Albertz et al., 2010; Wade & Maclean, 1990).

During the rifting, existing deposited formations were formed by red beds and evaporates (Figure 2.3.). Around the late Triassic and early Jurassic periods, Tethys Sea began spreading, and North American and African plates moved northward.

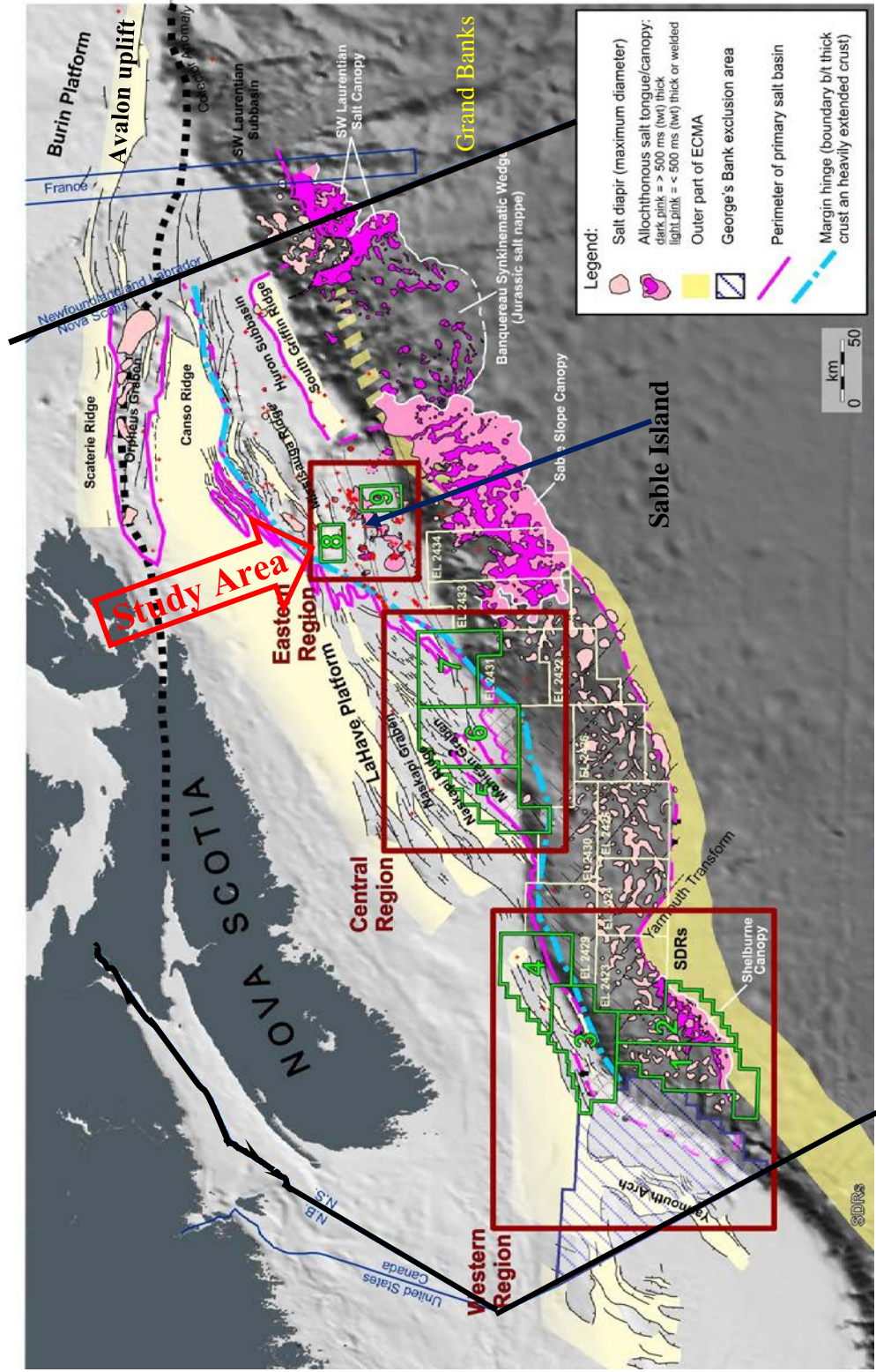


Figure 2.1. Location map of the Scotian Basin and its borders marked with black lines. The study area is shown with the red arrow in the vicinity of the Sable Island (modified from Smith et al., 2015).

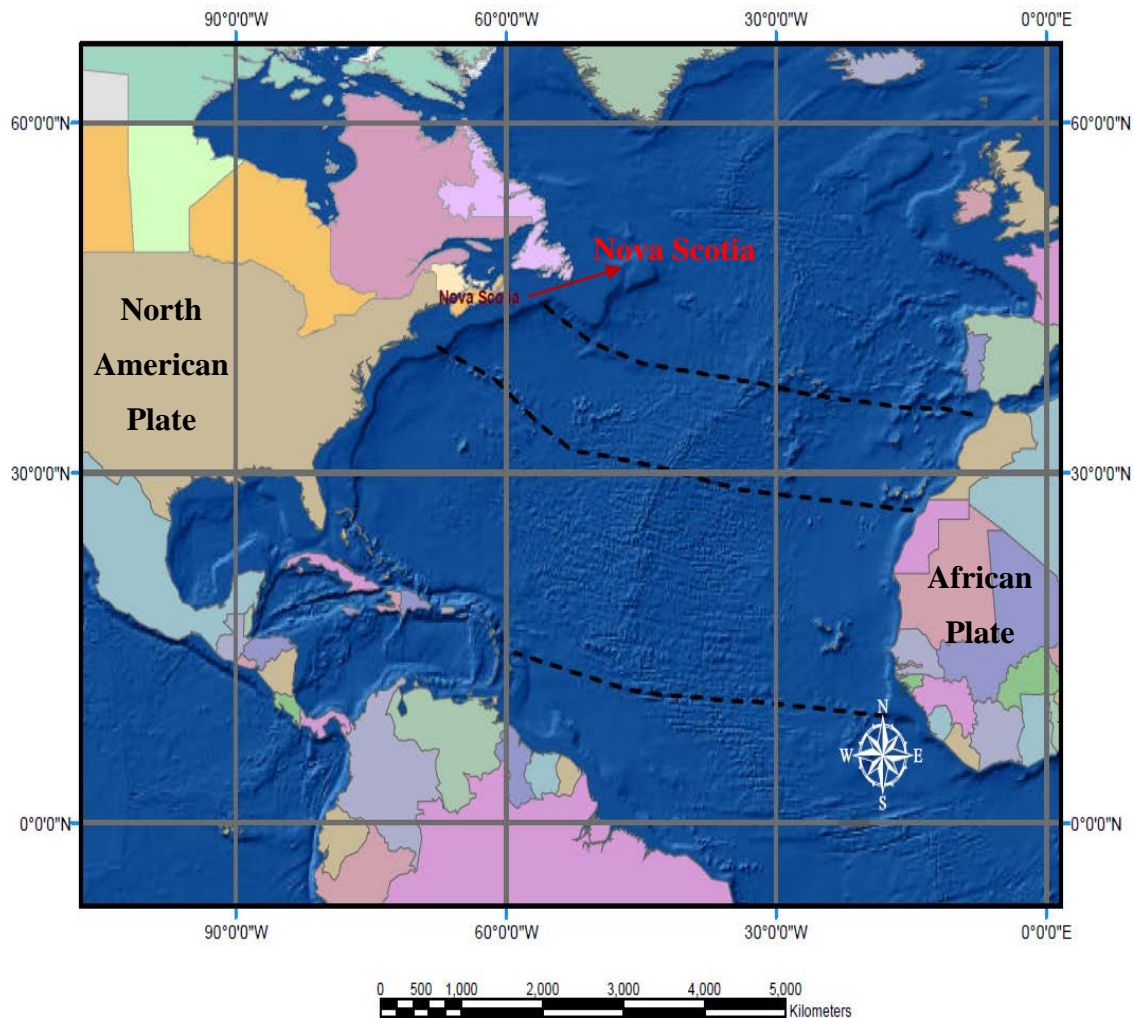


Figure 2.2. The present day global map of the Scotian Basin. The borders of North America and African Plates match well (modified from Kidston et al., 2005).

The Nova Scotia – Moroccan margin was driven into an arid, near equatorial region (Jansa & Wade, 1975a).

During the spreading, evaporates of the Argo Formation accumulated into half grabens and subbasins as a result of the arid climate (Wade et al., 1990; Welsink et al., 1989; Balkwill & Legall, 1989). The deposits of the Argo Formation in the half grabens

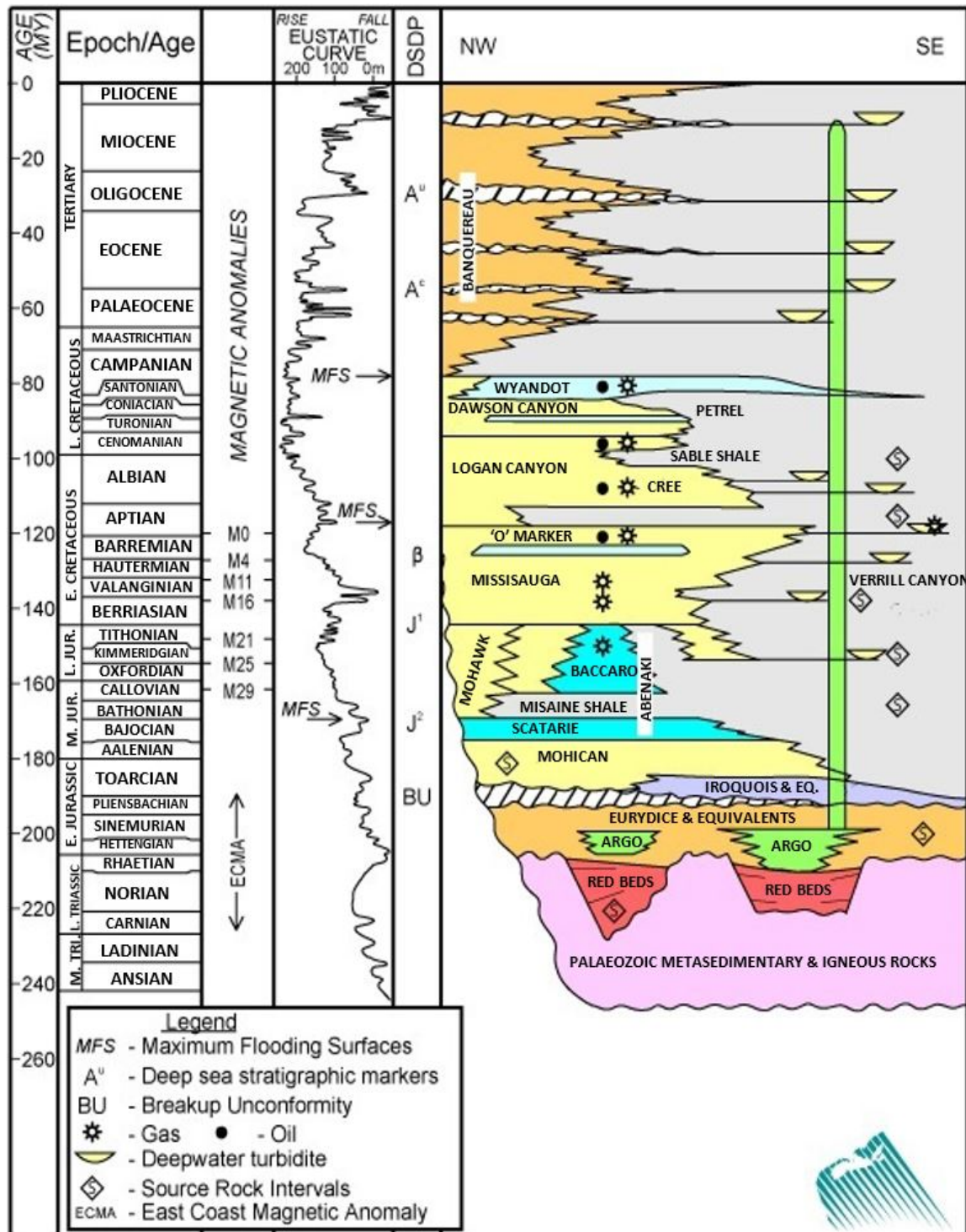


Figure 2.3. General stratigraphy of the Scotian Basin, offshore Nova Scotia (CNSOPB, 2008).

and subbasins contributed the formation of future petroleum systems (Jansa & Wade, 1975a). Figure 2.4 shows the location of present day evaporates of the Scotian Basin.

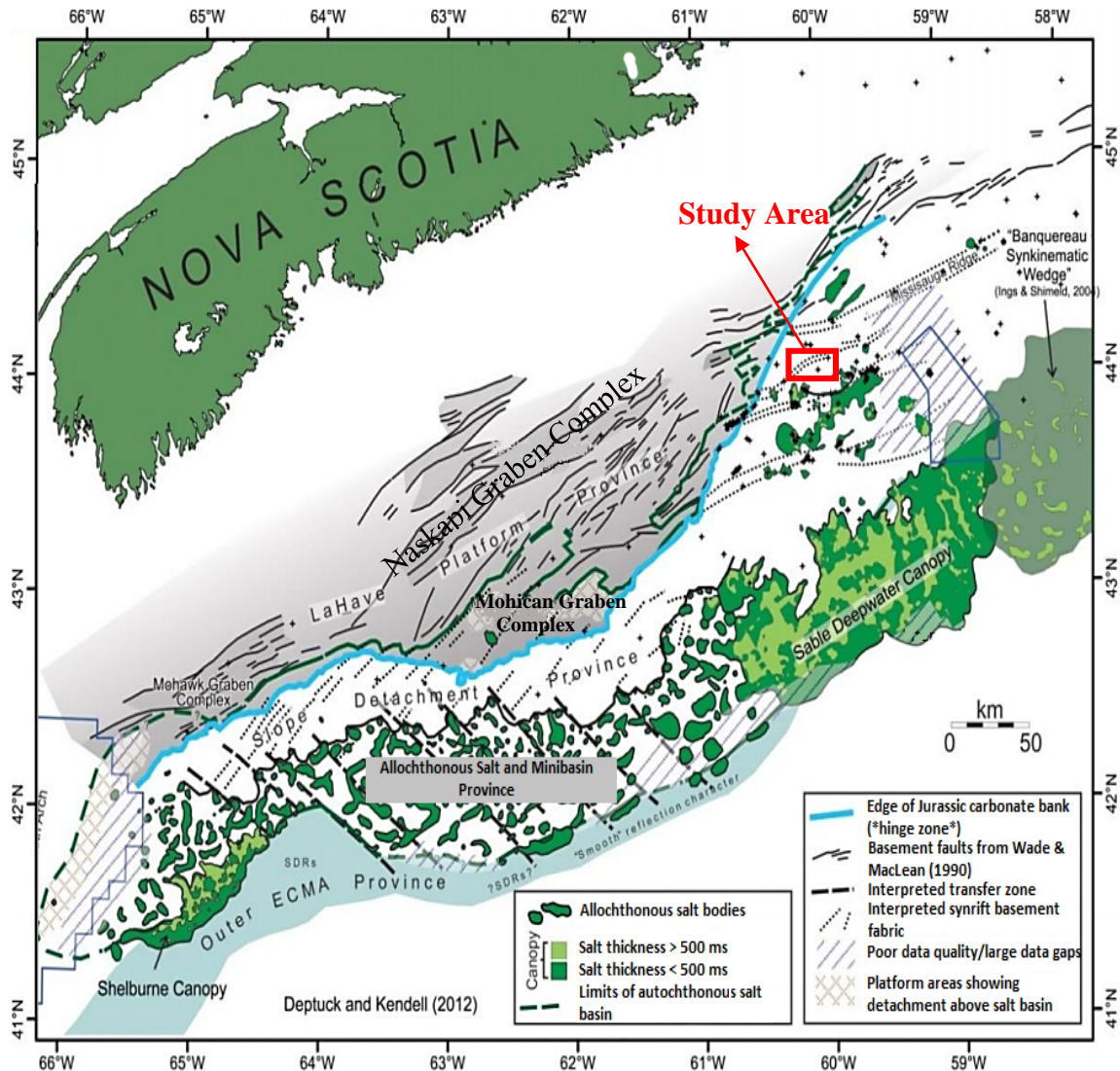


Figure 2.4. Salt structures of the Scotian Basin in green (modified from Sayers, 2013).

During the break-up of Pangea in the late Triassic Period, widening of the Fundy Basin (Figure 2.5) caused faulting. Consisted listric fault systems were located on the

Mohican and Naskapi grabens (Wade et al., 1996). These grabens acted like a deposition place for clastic sediments, which are found in present day Nova Scotia (GSC, 1991).

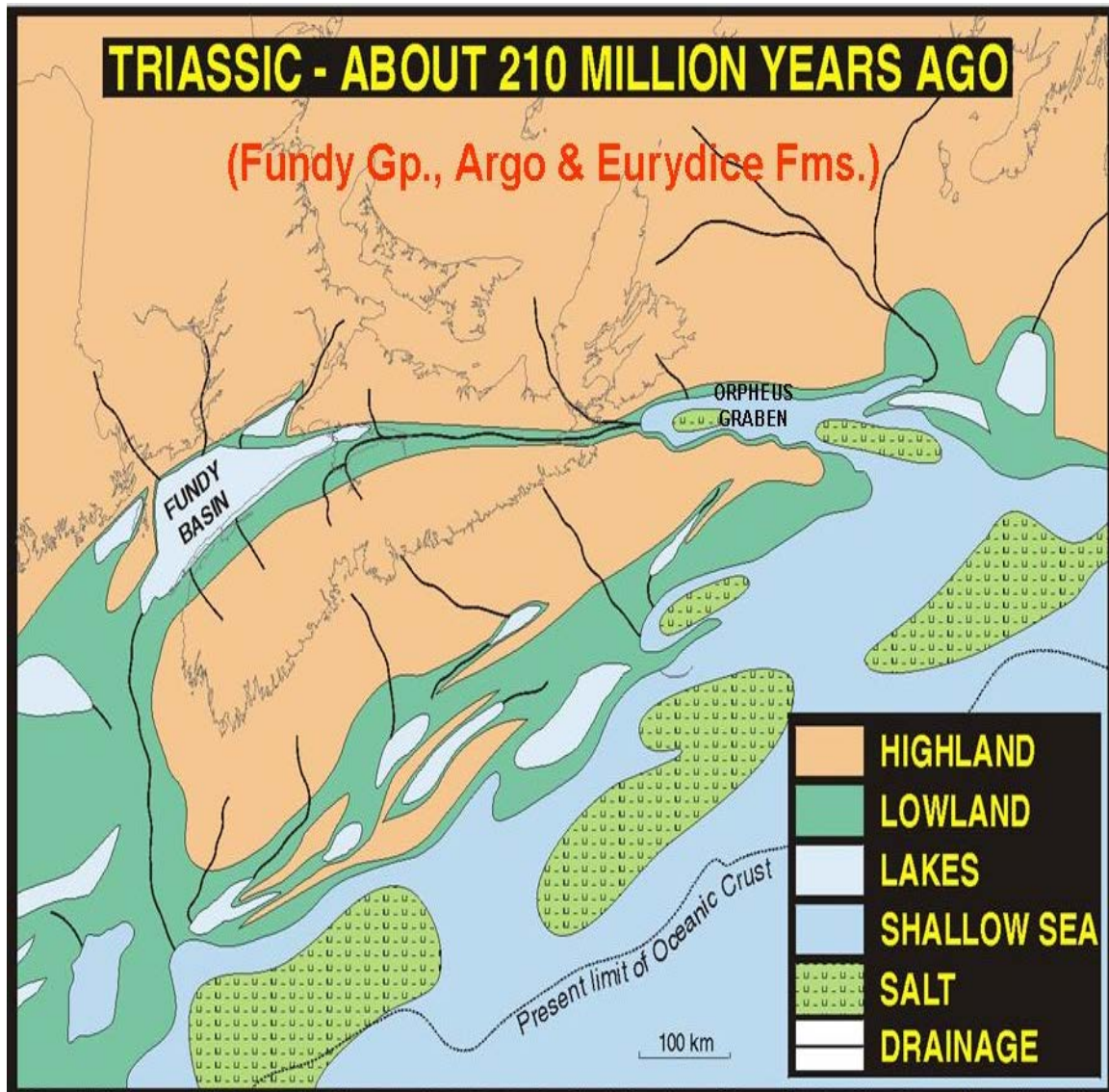


Figure 2.5. The map of the Scotian Basin 210 million years ago. The widening of the Fundy Basin and the salt formation in this period are shown (CNSOPB, 2008).

The separation of continents terminated in the Early Jurassic Period, and it was the inception of the sea floor spreading in the Sinemurian (Albertz et al., 2010).

During the Mid-Jurassic Period, the Atlantic Ocean started to extend and a carbonate bank began to form in the west of the Scotian Basin (McIver, 1972). The Upper Jurassic and Lower Cretaceous deltaic depocentres stimulated the formation of the carbonate bank and also locally covered the carbonate deposition. At the Middle Jurassic Period, the rising sea level collaborated with marine succession, and the sea water covered the shelf. The sea water carried the deep marine shales over the carbonate formation. The carbonate reef, bank, and platform environments proceeded to grow up from the Late Middle to the end of the Jurassic Period and formed Baccaro Member of the Abenaki Formation (Wade et al., 1990).

While the African plate was departing, sea floor spreading continued with the transgression of the sea. A significant transgression occurred throughout the eastern portion of North America and caused the accumulation of shale, sand, and limestone during the Late Jurassic Period (CNSOPB, 2008).

The Mississauga Formation, originated as a dominant formation in the Early Cretaceous Period, was formed by sand-rich deltaic deposits, strand plain, carbonate shoals, and marine successions. The shale of the Mississauga Formation drove marine sediments towards the land (Jansa & Wade, 1975a). The sedimentation environment changed with the regression of particular regions (Ings & Shimeld, 2006) and the drift of the European Plate from North America (Jansa & Wade, 1975a). This event determined the important features of the Scotian Basin that separate it from other basins. In the Late

Jurassic, Cretaceous sands accumulated in Scotian Subbasins and, during this period, the Sable delta started shaping (Figure 2.6).

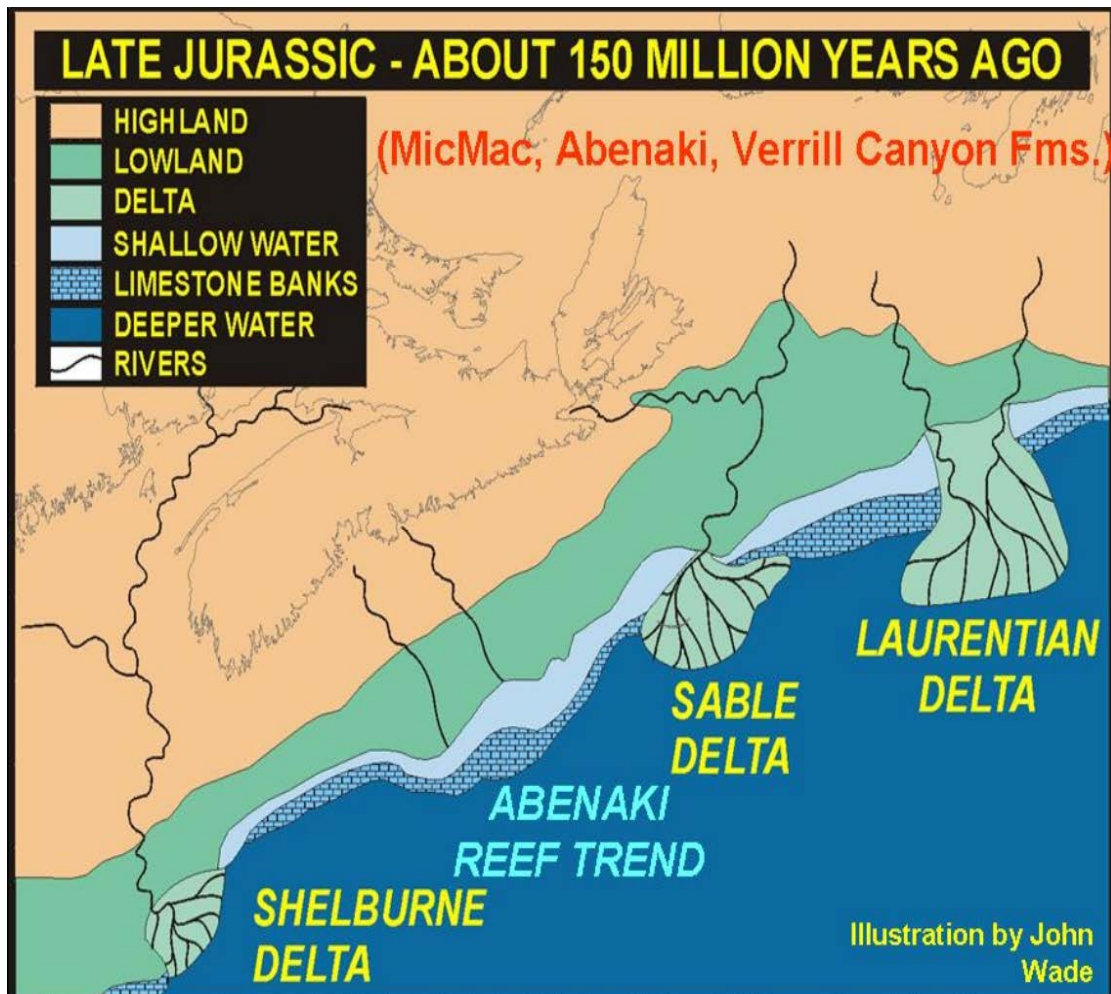


Figure 2.6. The map of the Scotian Basin 150 million years ago in the Late Jurassic. The figure shows the last period of the Abenaki carbonate margin, which is blanketed by the Mic Mac Formation delta systems at the next periods (CNSOPB, 2008).

Growing fault systems in the Sable and Laurentian Subbasins and high-speed sediment deposition thrived as a delta in the Early Cretaceous. Regression of the sea level

caused a large amount of sand to fill the outer regions of the delta (Cummings & Arnott, 2005). Excessive loading of sediments stimulated the formation of salt structures, such as diapirs, pillows, canopies, on the slope and in regions like the Sable and Shelburne deltas (Kidston et al., 2002; Shimeld, 2004) (Figure 2.6). Salt structures moved through the areas that had high deposition rates. The movement direction of the salt structures was vertically and in the seaward direction (Wade et al., 1990).

At the times of sea water regression, rivers cut into the sediments that were on the outer shelf-edge deltas (Cummings & Arnott, 2005). From Middle Jurassic to Cretaceous, these deltas carried turbidity currents and large amounts of sediments into the canyons and basins where they probably hosted potential reservoirs.

At the Early Cretaceous, Logan Canyon Formation, which overlies Mississauga Formation, was accumulated as sand and shale by a transgression. Laurentian Delta also formed during this period as a lagoon-marsh floodplain system (Jansa & Wade, 1975a).

At the Early Late Cretaceous period, deltaic sedimentation was stopped after a marine transgression. Also Dawson Canyon Formation, formed by deeper marine shale and limestones, represents the evidence of sea level rising. The Dawson Canyon Formation formed over Logan Canyon Formation (Jansa & Wade, 1975b). A Change in the sediment environment is shown by Wyandot Chalk, which overlies Dawson Canyon Formation.

Wyandot Formation was created by the loading of marine marls and chalky mudstones during a rise in sea level at the end of the Cretaceous period. Subsidence, which occurred because of high-speed sediment accumulation, caused the shelf to incline basinward (Jansa & Wade, 1975a). As a following process, Banquereau Formation

(Figure 2.7), formed by marine shelf mudstones and later shelf sands and conglomerates, blanketed Wyandot Formation during the Tertiary period.

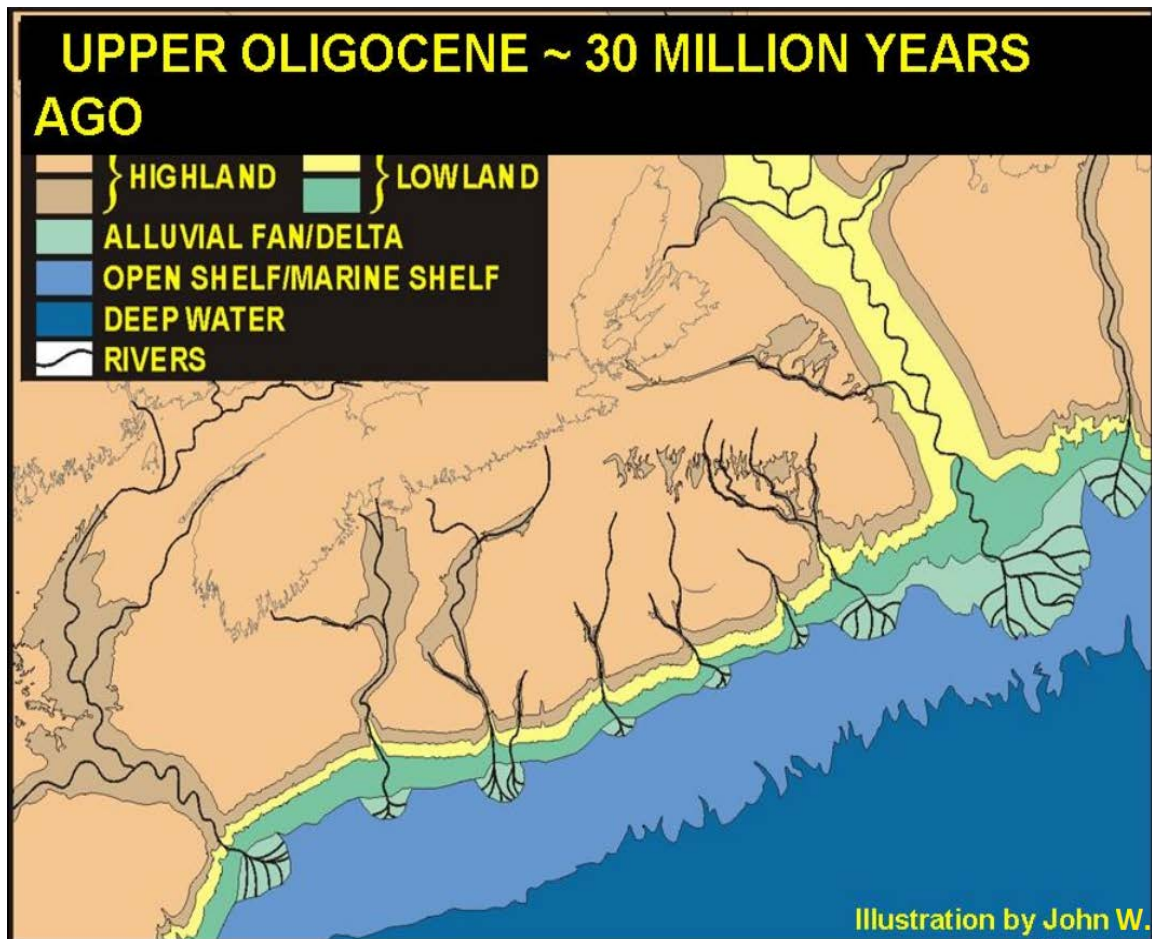


Figure 2.7. The map of the Scotian Basin 30 million years ago. The figure represents the results of the sea level falls and deposition of the Banquereau Formation. Small and larger deltas were illustrated (CNSOPB, 2008).

2.2 TECTONIC DEVELOPMENT

The Scotian Basin is located in southeastern Nova Scotia and is an accumulation terrace with sediments from the Mesozoic-Cenozoic ages. During this time span, the

Yarmouth Arch, the southwest of the Scotian Basin, acted as the west wall of this important salt-related basin, and the Avalon Uplift was also as a border in the northeastern.

Jansa and Wade (1975a) defined the tectonic evolution of the Scotian Basin in terms of plate tectonics. While the Atlantic Ocean was opening through sea floor spreading, large amounts of sediments began to accumulate in many hinged subbasins of the Scotian Basin in the Middle Triassic. The studies of Officer and Ewing (1954), Dainty et al. (1966), Keen et al. (1975), and Keen and Cordsen (1981) suggest that a north-east directed graben complex was forming the Scotian Basin during Middle and Late Triassic when the red beds formed.

As mentioned before, the Scotian Basin hosts many grabens and faults connected to each other in the northeast direction. These graben-half graben structures present different shapes such as small, and shallow, and they subsume various amounts of redbeds and salt. During the significant continental break-up, many faults formed due to sea floor spreading. The early Jurassic basement hinge zone, which lies in the northeast direction, consists of these faults and various bended structures. In some cases, the hinge zone cuts off the faults, indicating that the hinge zone formed after rifting (Wade & MacLean, 1990).

The major structures of the Scotian Basin are salt-related structures and fault zones. When the rifting ended in the Nova Scotia region, several normal faults were created by a primary hinge zone under the Abenaki reed trend (Wade & MacLean, 1990 hereafter). The Scotian Basin has two fault zones that run from the northeast to the southwest and one in the northern part, which was active from mid-Jurassic to the Tertiary. These two main fault zones coalesce into one zone in the west of the basin in the east-northeast direction. The development of these fault systems occurred between middle Jurassic to the Tertiary. The

faults in the southern part stimulated the newly coming deposits towards the deeper sea. The west part of the Sable Subbasin has the main listric faults, toward sea in a less depth. The main tectonic activity of these listric faults occurred in the Late Jurassic, Early Cretaceous, and Late Cretaceous. A very deep listric fault system, which reached the level of the Wyandot formation, is located in the vicinity of the eastern part of Sable Island, and these faults were considerably close to each other. These faults show the level of the extension in the outer shelf terrace.

3. DATA

3.1. DATA INFORMATION

3.1.1. Seismic Data. The data were acquired in a marine offshore environment by Western Geophysical Company on behalf of the Nova Scotia Resources on 8 June 1985. 2-D seismic lines were obtained from the CNSOPB-Geoscience Research Centre (GRC). The length of 2-D seismic profiles i.e. 3C, 45, and 46, are 29.4 km, 11.9 km, and 11.7 km, respectively. Figure 3.1 shows the base map of the research area and locations of the seismic profiles and wells. Preprocessing of the data was done by Kelman Seismic Processing in 2008. The preprocessing steps included (obtained from the header files of the data by Seisee Software):

- 1) Reformatting to KTI internal format
- 2) Merging navigation and geometry
- 3) Designature processing: signal extracted from seismic data
- 4) Eliminating surface related multiples
- 5) Suppressing random noise
- 6) Predictive deconvolution
- 7) Scaling surface consistence
- 8) Analyzing velocity at 1.0 km
- 9) Multiple attenuation (hyperbolic radon)
- 10) Analyzing velocity at 0.5 km
- 11) SEG-Y output

The seismic data utilized in this research is a pre-stack non-nmo, multichannel, and 6000% folded marine data set. Pre-stack and post-stack processing were conducted to enhance signal-to-noise ratio of the Penobscot marine 2-D data set. The important acquisition parameters for the lines can be found in Table 3.1.

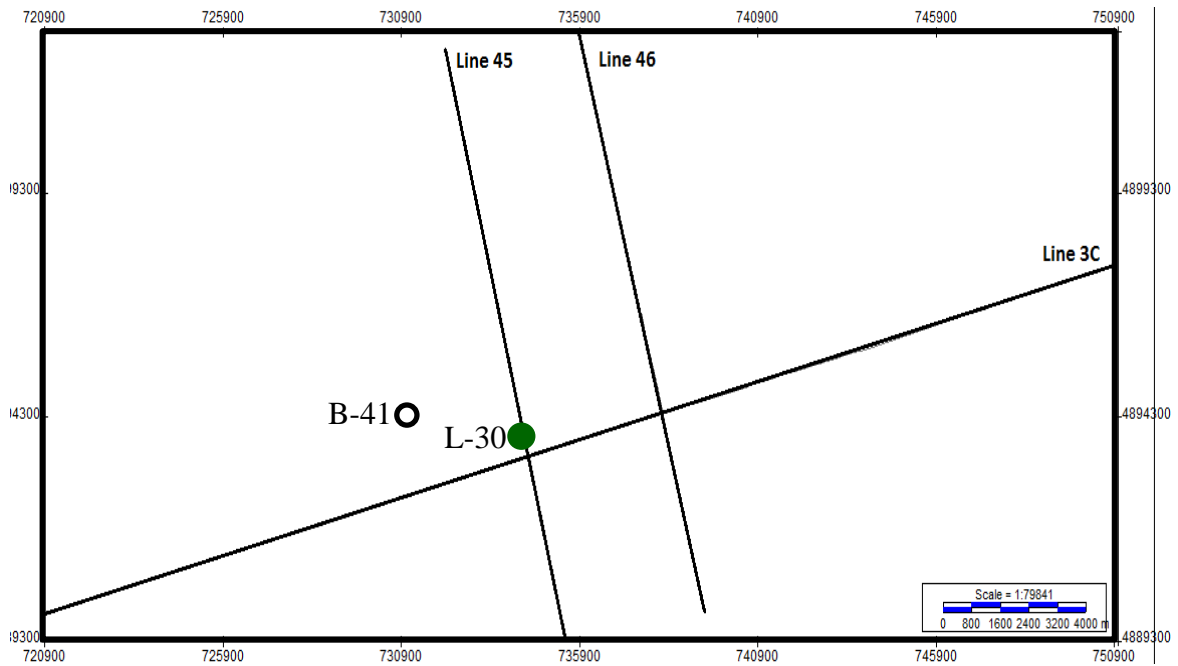


Figure 3.1. The base map of the research area. Lines 45 and 46 intersect with Line 3C. Well L-30 is located on Line 45. The distance between Well L-30 and Well B-41 is 3.2 km.

Reprocessing was conducted in this study to improve resolution, sharpen the faulted structures, and increase the layer continuity for structural interpretation. In the research area, Wells L-30 and B-41 were drilled in 1976 and 1977 respectively by PetroCanada-Shell. Well L-30 was located on Line 45 and used to generate a synthetic seismogram for horizon interpretation.

Table 3.1. Header information of seismic lines. Some of the information were changed after post-stack processing (Goodman, 1985).

Line Name	Line 3C	Line 45	Line 46
Trace Number	131880	53640	52800
Shot Point Number	101-1205	101-549	101-540
Shot Number	8300-124650	8300-59050	15150-65000
CDP Number	169-2495	166-1181	302-1299
Offset Number	222-3410	222-3410	222-3410
X-source Coordinate	750939 - 720910	732127 - 735477	750939 - 720910
Y-source Coordinate	4897684-4889930	4902506-4889397	4897684-4889930
X-receiver Coordinate	750939 - 720910	732127 - 735477	750939 - 720910
Y-receiver Coordinate	4897684-4889930	4902506-4889397	4897684- 4889930
Sampling Number	1751	1751	1751
Sampling Interval	4000 ms	4000 ms	4000 ms
Length of the Line	29.4667 km	11.973 km	11.733 km
Shot Interval	26.67 m	26.67 m	26.67 m
Receiver Interval	26.67 m	26.67 m	26.67 m
CDP Interval	13.33 m	13.33 m	13.33 m

Both lines 45 and 46 contain highly faulted structures due to a fact that they are perpendicular to the major down-to-basin listric fault system (Figure 1.2). Line 3C was located parallel to the faulted region. As a result, Line 3C exhibits horizontal formations

with no termination, such as faults or angled structures. Lines 45 and 46 have major uplifted faulted structures merged with a low relief anticline, which was drilled by Well L-30, which encountered hydrocarbons in the Mississauga Formation Sands (CNSOPB, 2008).

3.1.2. Well Data. Well L-30 was drilled on a low relief anticline in 1976 that is attached to a major down-to-basin fault. Hydrocarbons were explored in the Mississauga Group. Well B-41 was drilled about 3 km northwest of Well L-30 in 1977. No hydrocarbons were discovered in the well. Check shot data can be found in Table 3.3. Both of the wells consist of the same logs, such as caliper, density, sonic, gamma ray, resistivity, and SP.

Table 3.3. Check shot data information from wells L-30 and B-41.

L-30				
MD (Meter)	TVD (Elev. R) (Meter)	TVD (Seismic)	Subsea (Meter)	Time (2-way) (s)
0	0	-29.9	29.9	0
837	837	807.1	-807.1	0.891
922	922	892.1	-892.1	0.943
1049	1049	1019.1	-1019.1	1.057
2378	2378	2348.1	-2348.1	1.955
3375	3375	3345.1	-3345.1	2.45
3990	3990	3960.1	-3960.1	2.9
B-41				
MD (Meter)	TVD (Elev. R) (Meter)	TVD (Seismic)	Subsea (Meter)	Time (2-way) (s)
0	0	-29.9	29.9	0
828	828	798.1	-798.1	0.869
935	935	905.1	-905.1	0.935
1063	1063	1033.1	-1033.1	1.055
2380	2380	2350.1	-2350.1	1.943
3391	3391	3361.1	-3361.1	2.432
3990	3990	3960.1	-3960.1	2.9

4. PROCESSING METHODS

For each seismic line, a different processing sequence was applied. The different geological structures of each seismic profile causes different responses to the same processing method. The best results were chosen between several different processing flows. Figures 4.1, 4.2, and 4.3 show the different processing flows for Lines 3C, 45, and 46

4.1 CONVERTING FROM SEG Y TO SU

All three seismic lines that were received from the Canadian-Nova Scotia Offshore Petroleum Board Data Management Center were already preprocessed by Western Geophysical Company. The geometry of the data were set and some of the important preprocessing steps were conducted by the company. Some of the multiples and noise were removed during the preprocess.

Seismic data were not stacked or NMO corrected. The data format was first converted from the segy format to the Seismic Unix format (su).

4.2 BUTTERWORTH FILTER

The Butterworth minimum phase band-pass filter was applied during the prestack processing by assuming the source wavelet as minimum phase. The Butterworth filter is a very popular filter that gives very good results.

The amplitude spectrum of a band-pass Butterworth filter is (Crosson, 2014):

$$\left| G_{passband}(f) \right|^2 = \frac{1}{1 + \left[\frac{(|f| - f_b)}{f_c} \right]^{2n}} \quad (1)$$

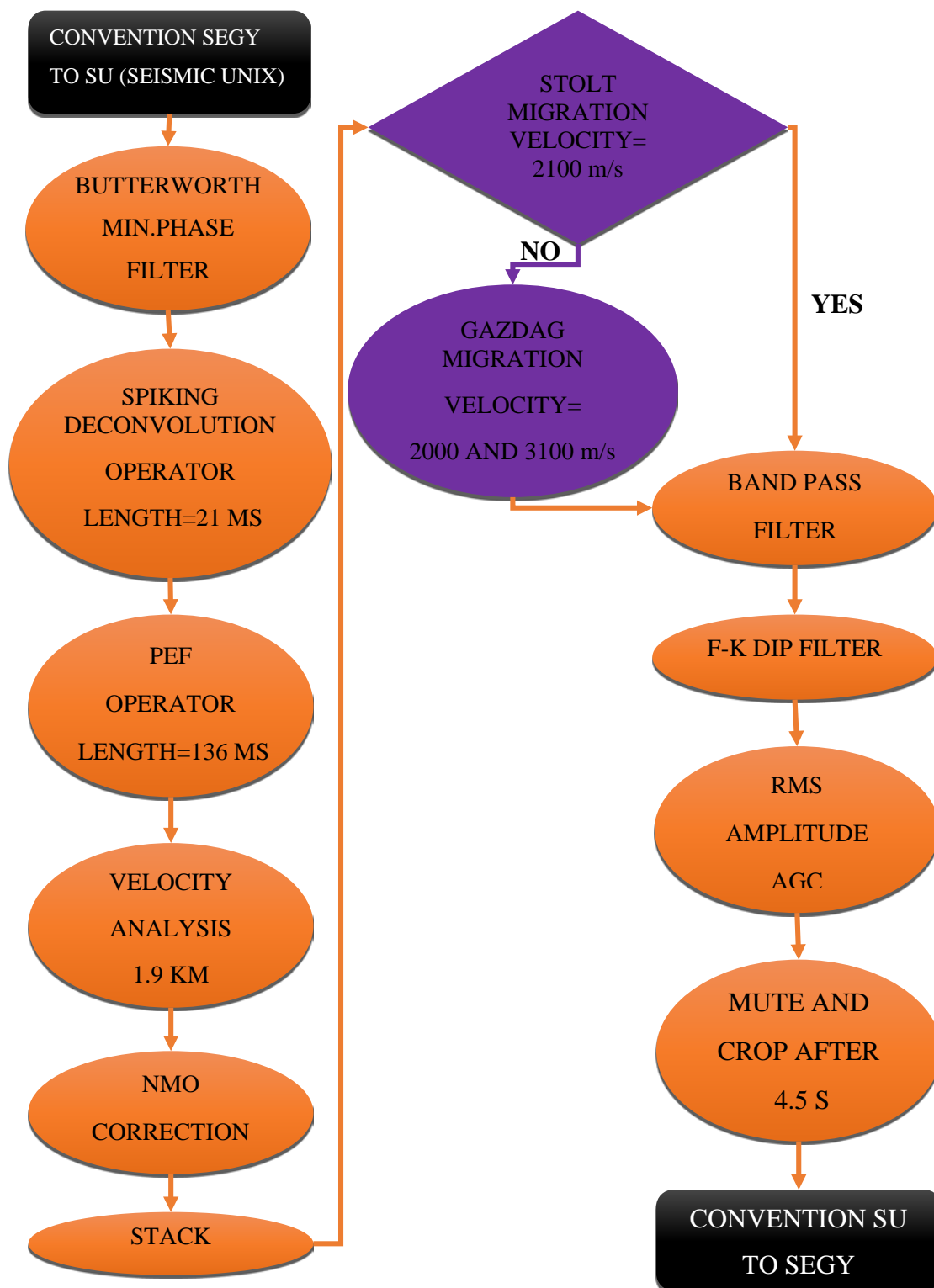


Figure 4.1. The processing flow chart for Line 45. PEF: Prediction error filter.

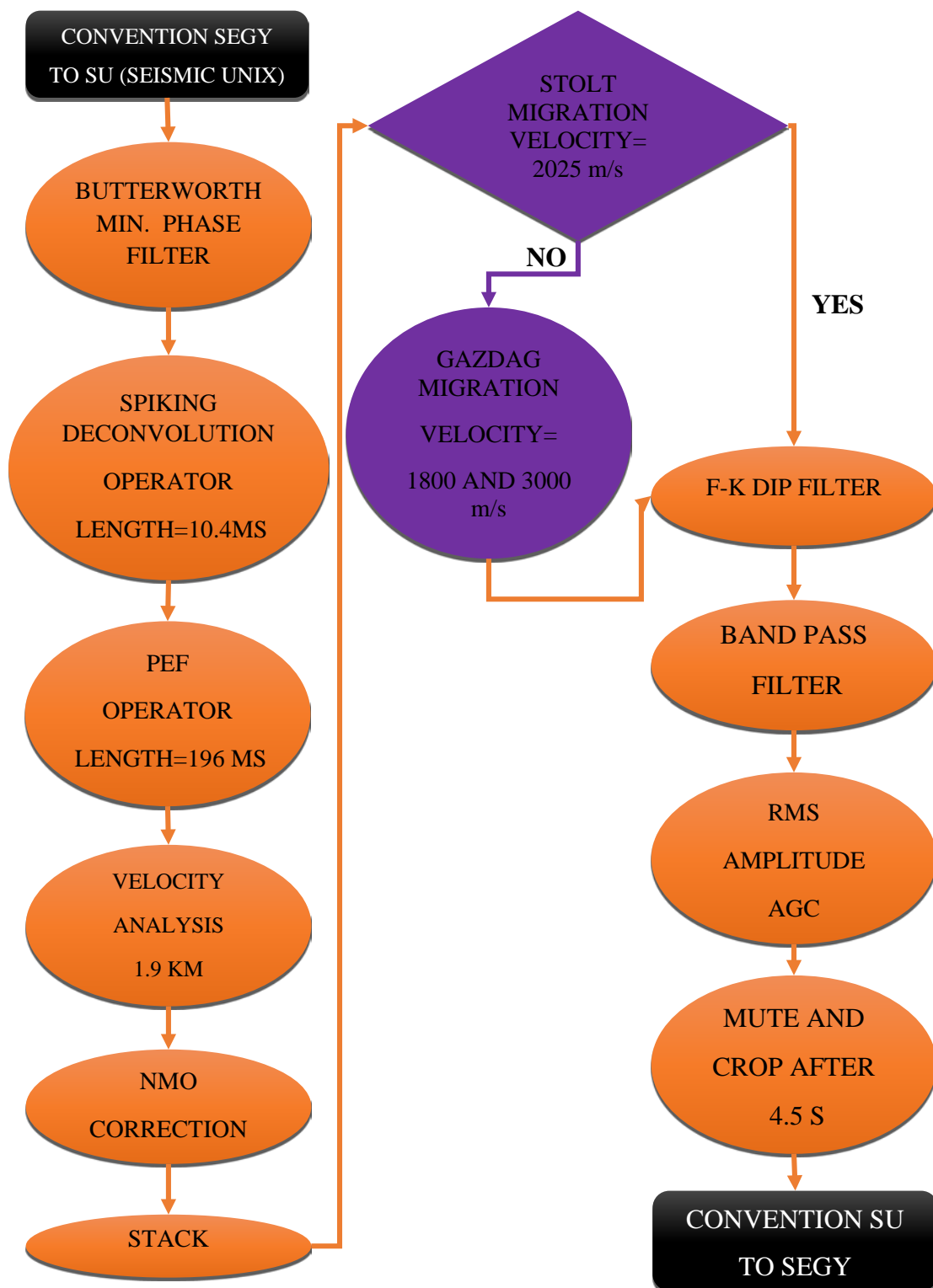


Figure 4.2. The processing flow chart for Line 46. PEF: Prediction error filter.

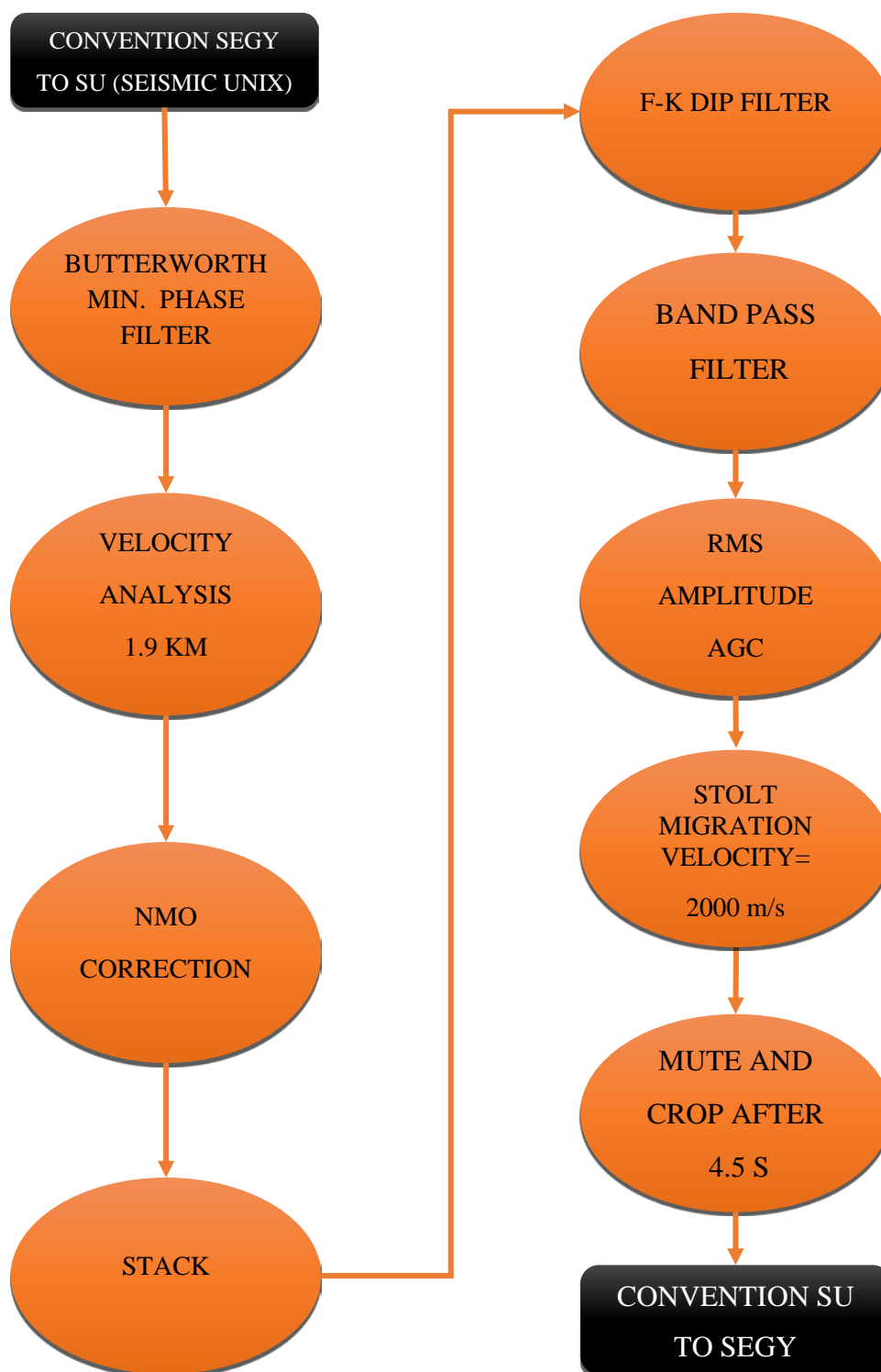


Figure 4.3. The processing flow chart for Line 3C.

where f_b is the center value of the pass band and f_c is the half width of the pass band. Like other frequency filters, frequency values are determined to design a band-pass filter. These values include two cut-off frequencies. The Butterworth filter's corner frequencies are 3 dB down, which are less powerful than the other frequency filters.

The Butterworth minimum phase band-pass filter was applied to all three seismic lines to remove some of the low and high frequency noise, and to enhance the water bottom peaks (Figure 4.4). The Butterworth minimum phase filter solved the low amplitude problem of the ocean bottom peaks after stacking. This was one of the major problems during processing. Figure 4.4 shows ocean bottom of Line 45 before and after Butterworth filter. This filter was applied as minimum phase because in pre-stack process, data is assumed to be minimum phase. The Butterworth filter was designed using the frequency values from the frequency spectrum. The filter removed the frequencies lower than 10 Hz and higher than 70 Hz. The amplitude spectrum of Line 45 shows the frequencies of the seismic section before and after the Butterworth filter (Figure 4.5). The signals with high amplitudes are located between 20 Hz and 45 Hz. Figure 4.6 shows CDP 450 before and after filtering. Low and high frequency noise were removed from all sections.

4.3. SPIKING DECONVOLUTION AND PREDICTION ERROR FILTER

Deconvolution is one of the most important steps of data processing. The equation for deconvolution is expressed as (Yilmaz, 1987):

$$x(t) = w(t) * e(t) + n(t) \quad (2)$$

where $x(t)$ is recorded seismogram, $w(t)$ is basic seismic wavelet, $e(t)$ is earth's impulse response, $n(t)$ is random ambient noise, $*$ is denotes convolution.

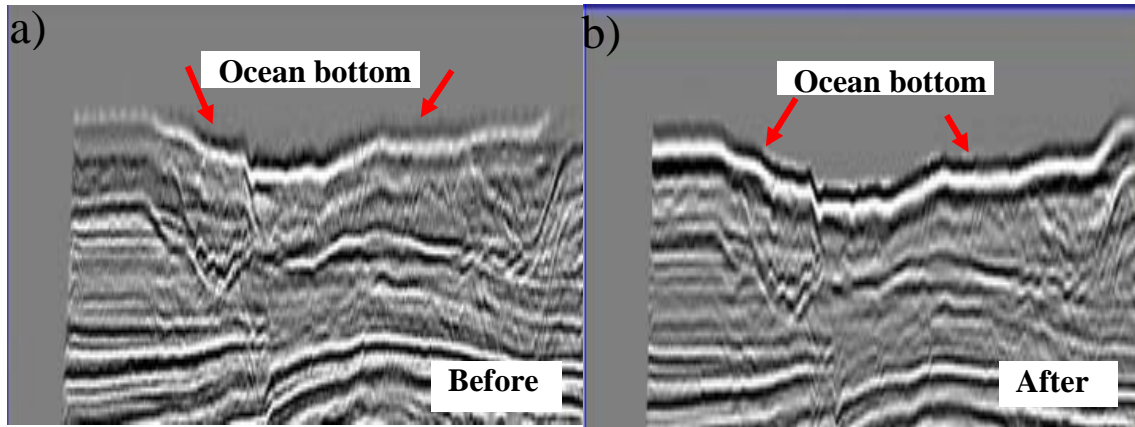


Figure 4.4. Line 45 before and after the Butterworth filter. Sea bottom peaks have higher amplitudes in Figure B.

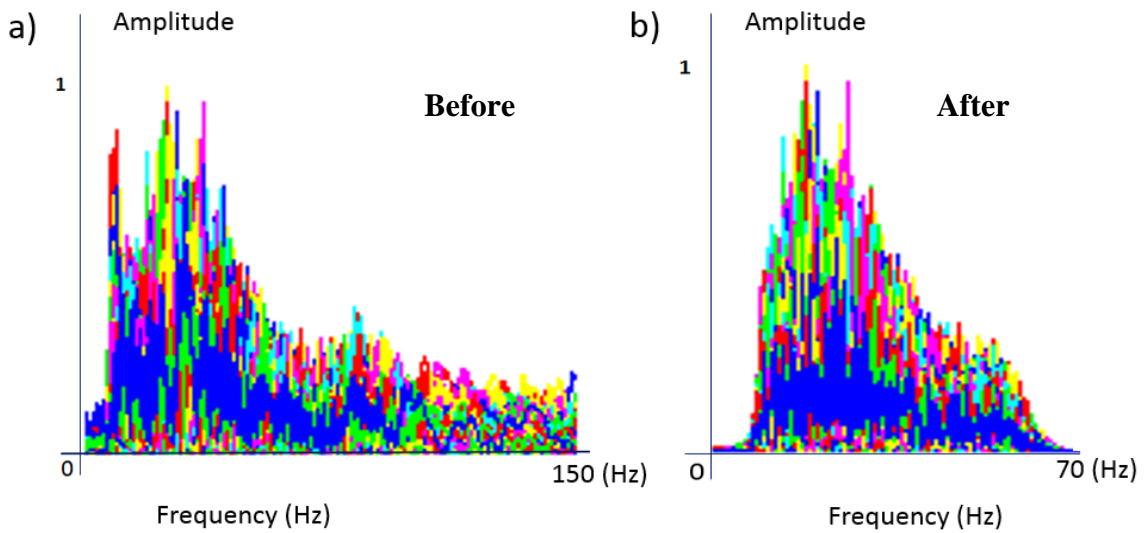


Figure 4.5. Amplitude spectrum of Line 45 before and after the Butterworth filter. The frequencies lower than 10 Hz and higher than 70 Hz were removed. High amplitude signals range between 20 Hz and 45 Hz.

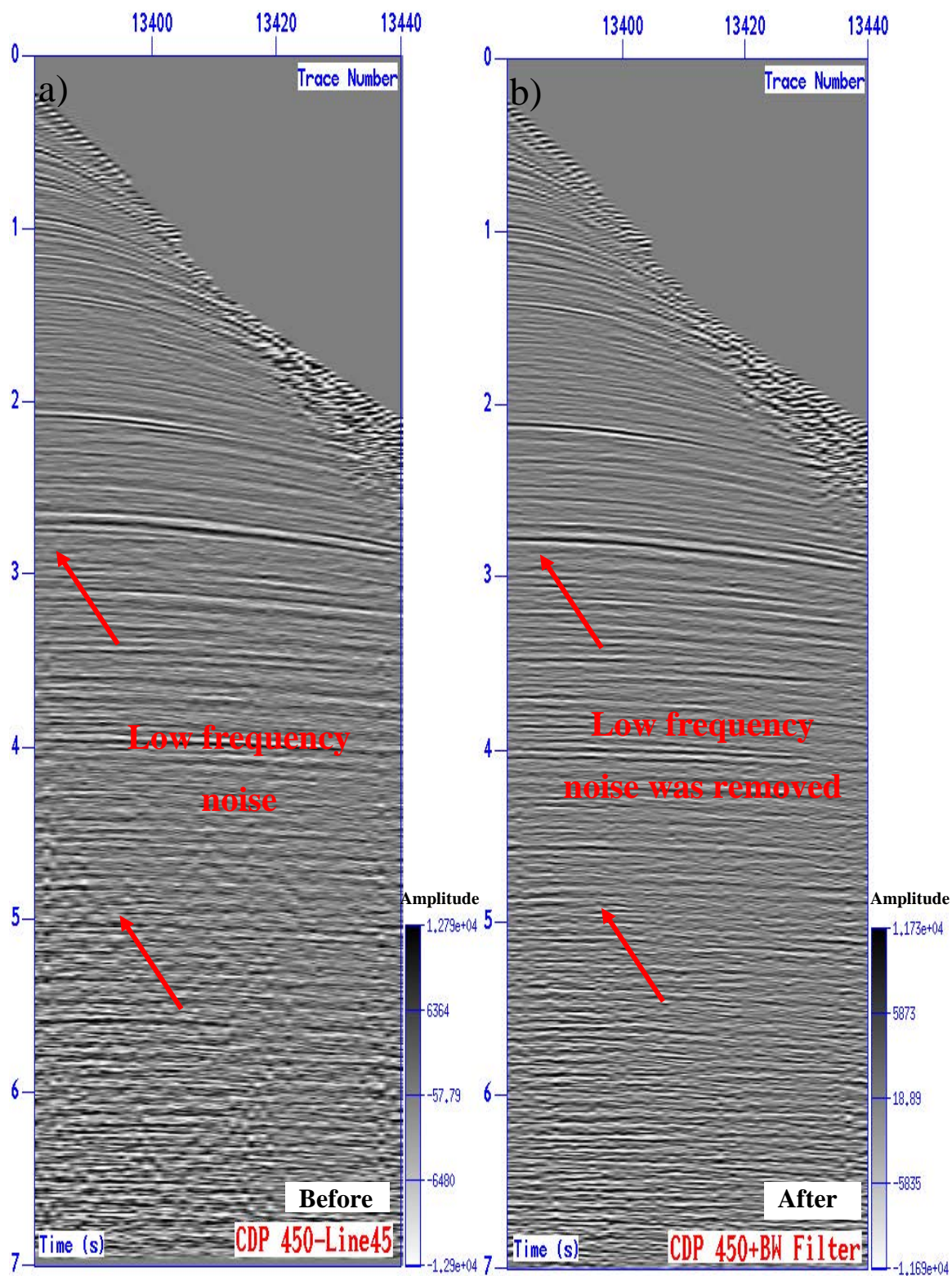


Figure 4.6. CDP 450 from Line 45 before and after the Butterworth filter. High frequency noise that is higher than 70 Hz and low frequency noise that are lower than 10 Hz were removed.

4.3.1. Spiking Deconvolution. In the spiking deconvolution step, a basic wavelet of the seismic data is compressed and tried to make the wavelet a spike to obtain a higher resolution and remove the multiples. The wavelet $w(t)$ from a source is exposed to interference by the earth's impulse response, and spiking deconvolution compresses the seismic wavelet by removing the source wavelet and leaving the earth's reflectivity series $e(t)$ and seismic traces $s(t)$ (Yilmaz, 1987).

4.3.2. Prediction Error Filter (Predictive Deconvolution, PEF). Random noise and multiples that interfere with the real signal can be determined using the autocorrelation window and PEF can be designed using period of the repetitions of multiples. The prediction error filter (Peacock & Treitel, 1969) mostly preserves the frequency differences between the real signal and noise, which allows this application to provide convenience for the determination of the real signal (Bormann, 2013).

The prediction error filter shortens a $(n+\alpha)$ long wavelet to an α -long wavelet, where a is the prediction lag (Peacock and Treitel, 1969).

4.3.3. Autocorrelation. Autocorrelation of the signal provides the necessary parameters, such as maximum and minimum prediction lags, to apply spiking deconvolution and the prediction error filter. Autocorrelation shows the similarity between seismic data and itself as a function of time-shift. The result of an autocorrelation is a zero-phase wavelet, symmetrical at the both sides of the wavelet's origin (Figure 4.7). During the calculation of an autocorrelation of a wavelet, the signal is multiplied with itself by shifting the second signal. After multiplication, the results are summed to gather a single autocorrelation wavelet (Antsey, 1977).

The prediction error filter and spiking deconvolution use autocorrelation window to produce a template for multiples. The autocorrelation window is produced for predicting the width of the wavelet from beginning to end, not from trough to trough (Figure 4.7). In addition, the repetition period of the multiples can also be determined using the autocorrelation window. A larger autocorrelation window that covers more data, can show the repetitions of the multiples from peak to peak and is used as prediction lag (Peacock & Treitel, 1969).

In order to remove the random noise and compressing the wavelet to a spike, the spiking deconvolution and predictive error filtering were applied to Lines 45 and 46. Every line have their own nature and Line 3C showed minor distortions when the deconvolution was applied. Line 3C provided better results without the deconvolution, therefore, deconvolution step was removed from the processing flow chart.

During the application of the spiking deconvolution, autocorrelation windows for each of the seismic lines were used to represent the autocorrelation wavelet. Figure 4.7 shows the strong autocorrelation wavelet of Line 45, which is symmetrical in both sides and multiples can be observed clearly.

After determining the gap (minimum autocorrelation lag) and operator length (maximum autocorrelation lag) (Table.4.1), spiking deconvolution and the prediction error filter were designed, respectively.

Autocorrelation window of Line 45 shows the multiple removal after the deconvolution in Figure 4.8. Filter was designed using the repetition period of the multiples as 136 ms for Line 45.

Table 4.1. Maximum and minimum autocorrelation lags of the seismic Lines 45 and 46, respectively.

LINE NAME	Line 45	Line 46
Width of the Autocorrelation Wavelet	0.021=21 ms	0.0104 = 10.4 ms
Period of the Repetitions	0.136=136 ms	0.196 = 196 ms

Deconvolution created very bright results for velocity picking. Before the deconvolution procedure, velocity semblance of two seismic data had many noise and the picking of the correct velocities for the primary reflectors was challenging (Figure 4.9a). Deconvolution enhanced amplitudes of the primary reflections between 1 and 2 seconds (Figure 4.9b). NMO correction was conducted successfully because increasing the resolution provided a more accurate velocity analysis. Figure 4.10 shows a CDP from Line 46 before and after deconvolution. The primary reflections among the noise and interval multiples were revealed.

In addition, deconvolution gave a flattened amplitude spectrum and increased the amplitudes of the higher frequencies (Figure 4.11). One problem with this process is that amplitudes of the noise are also increased along with the real signal.

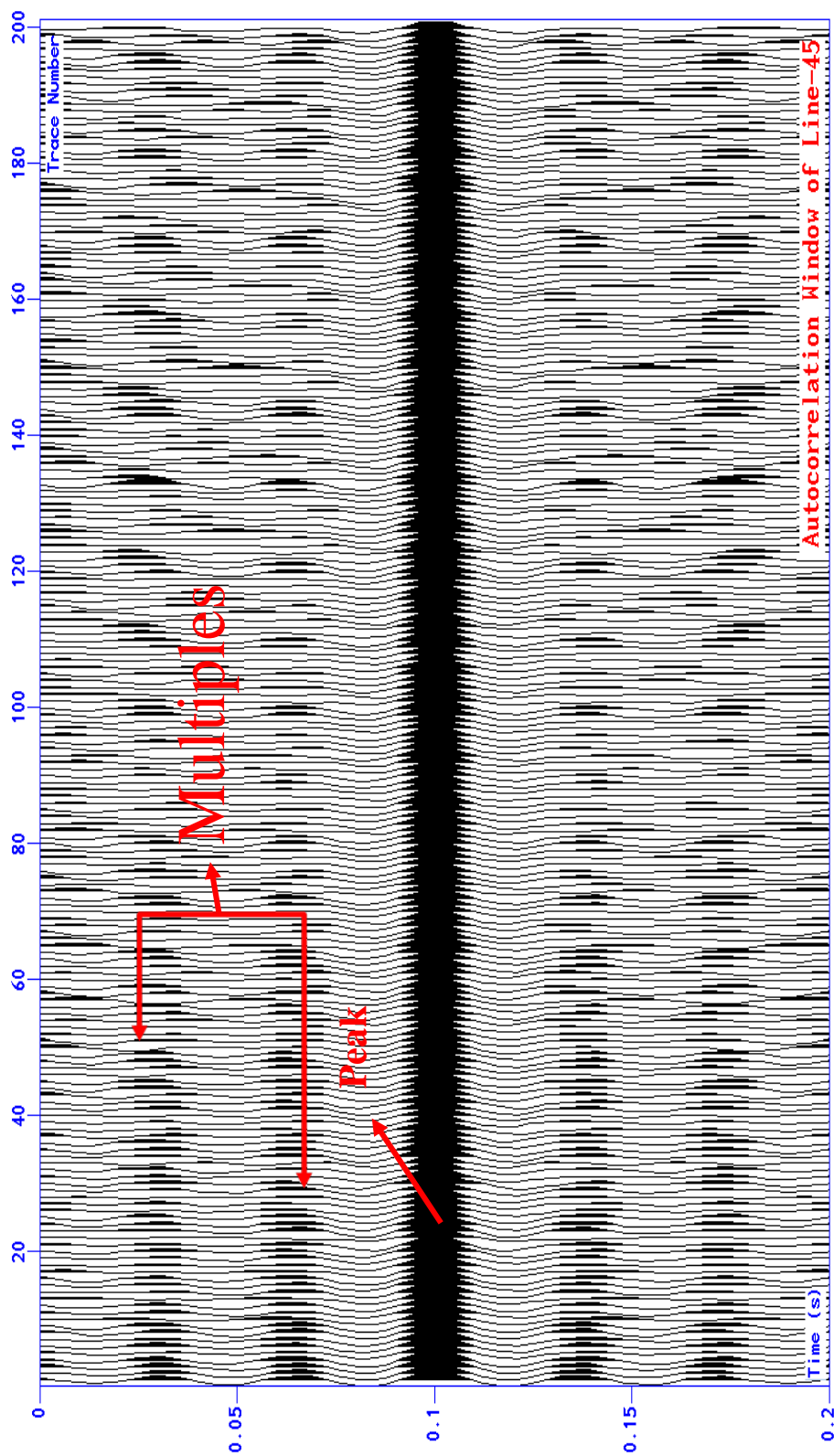


Figure. 4.7. Autocorrelation window of Line 45. There is a large peak where the two seismic data are correlated. The width of this strong wavelet (minimum lag) and the repetition times of the multiples (maximum lag) were used to design the deconvolution filter.

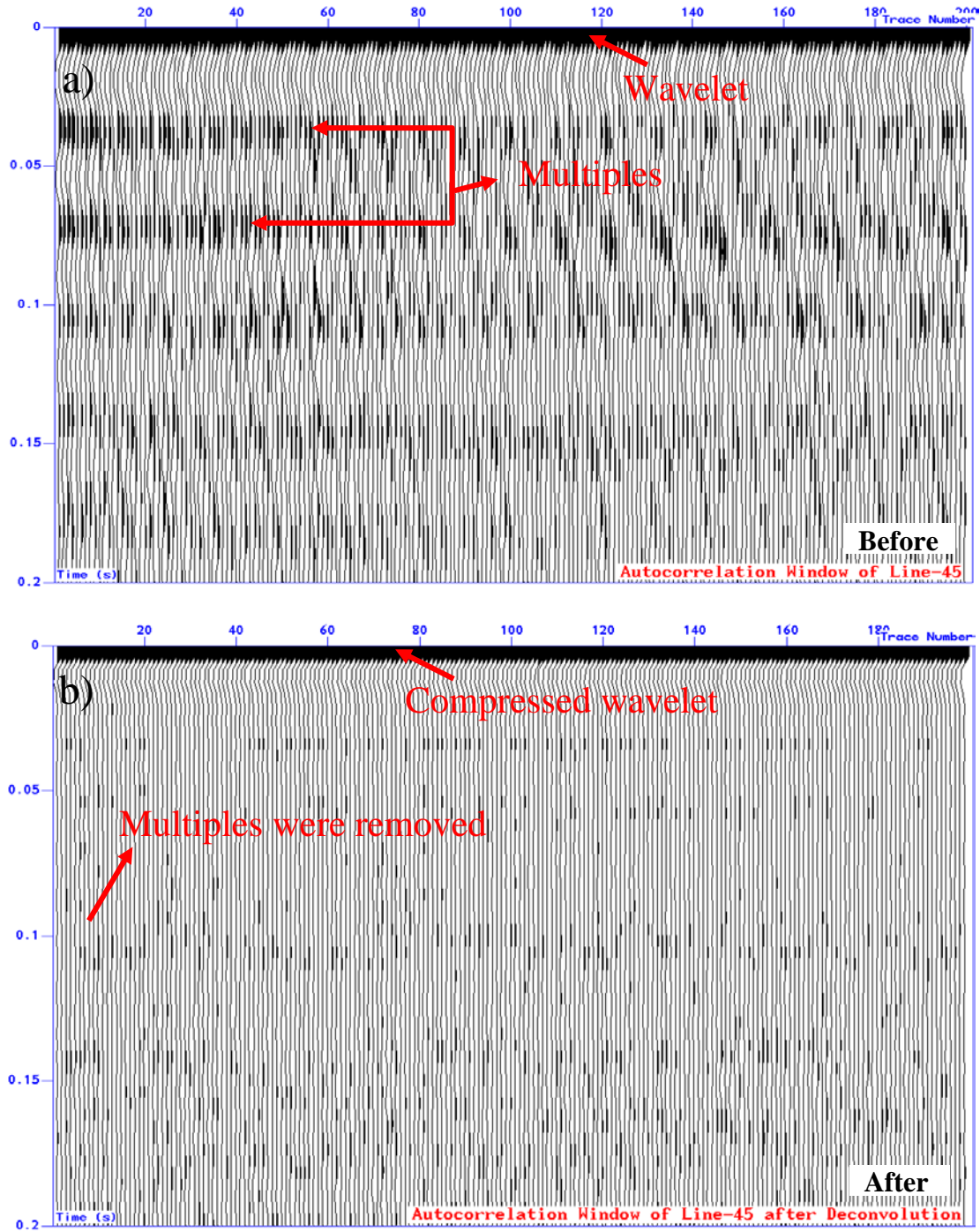


Figure 4.8. Autocorrelation window of Line 45 before and after deconvolution. A: The autocorrelation of Line 45 before deconvolution. B: The multiple removal after deconvolution.

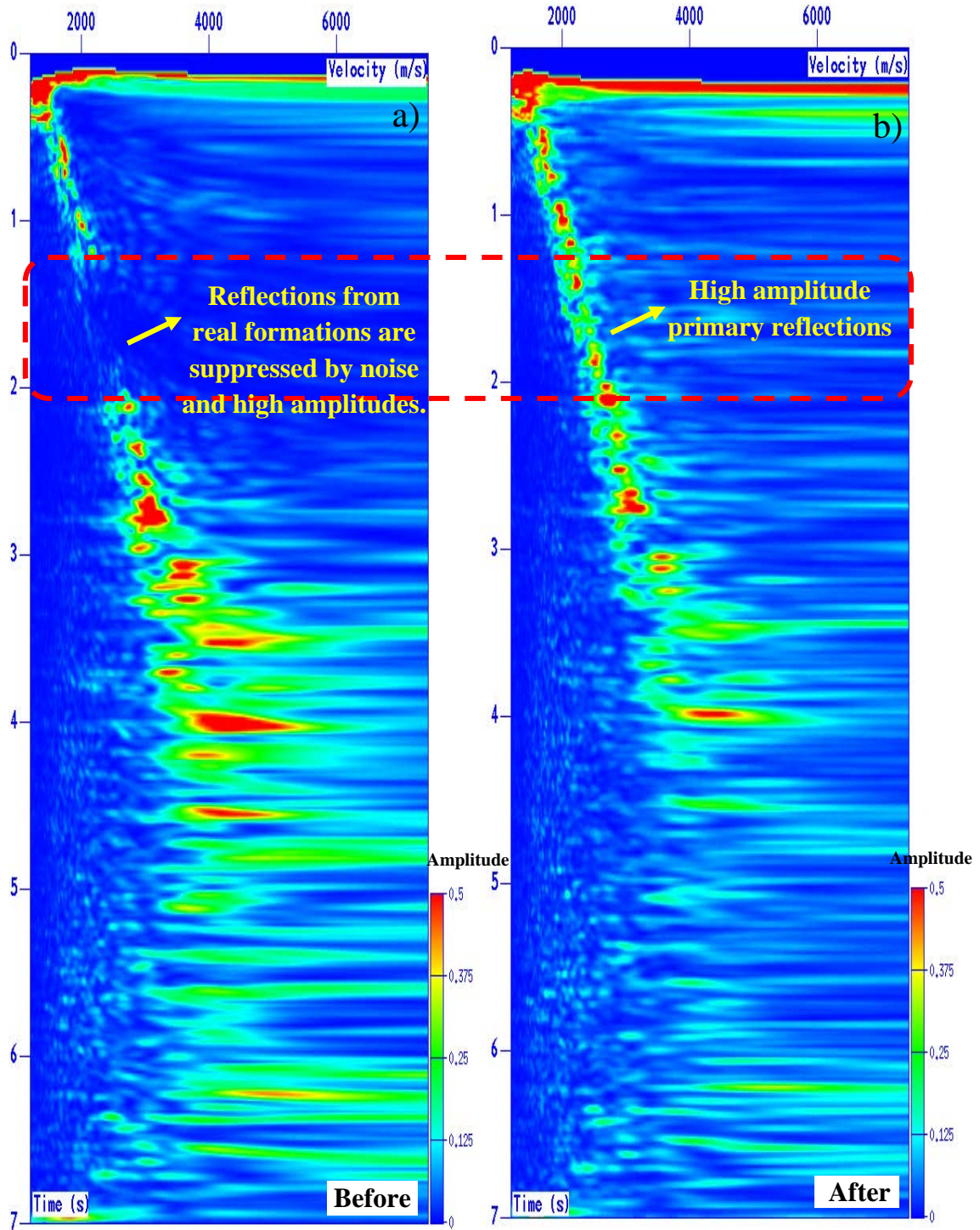


Figure 4.9. Velocity spectrum of CDP 450 from Line-45 before and after deconvolution. A : Many noises and interval multiples interfere with the primary reflections and prevent picking the correct velocities. B: The reflections between 1 seconds and 2 seconds become visible because the deconvolution increased the resolution. The noise after 3 seconds were mostly removed and the primary reflections were visible.

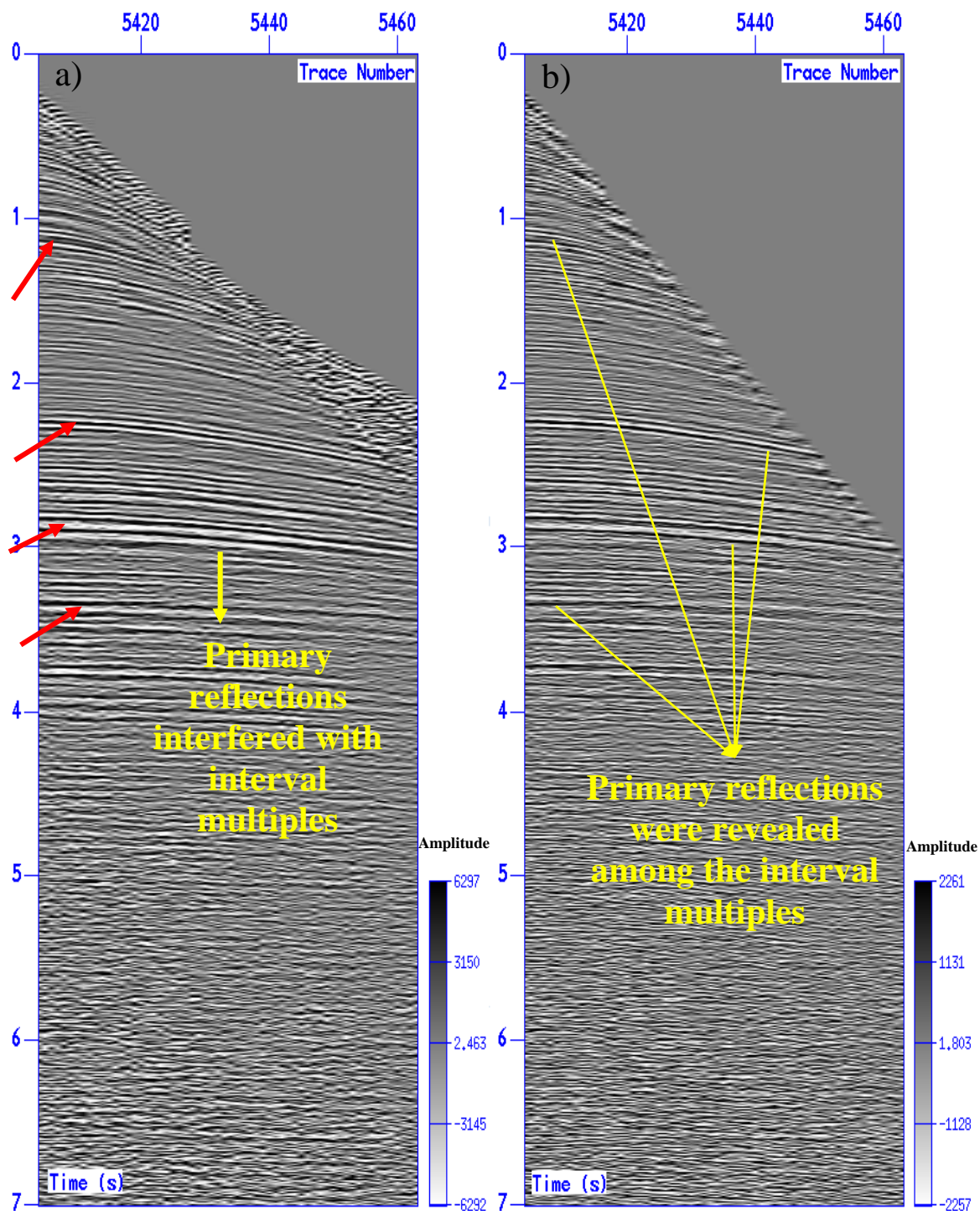


Figure 4.10. CDP 450 from Line 46 before and after spiking deconvolution and PEF. Deconvolution increased the resolution and the primary reflections from real layers that were lost in interval multiples become apparent.

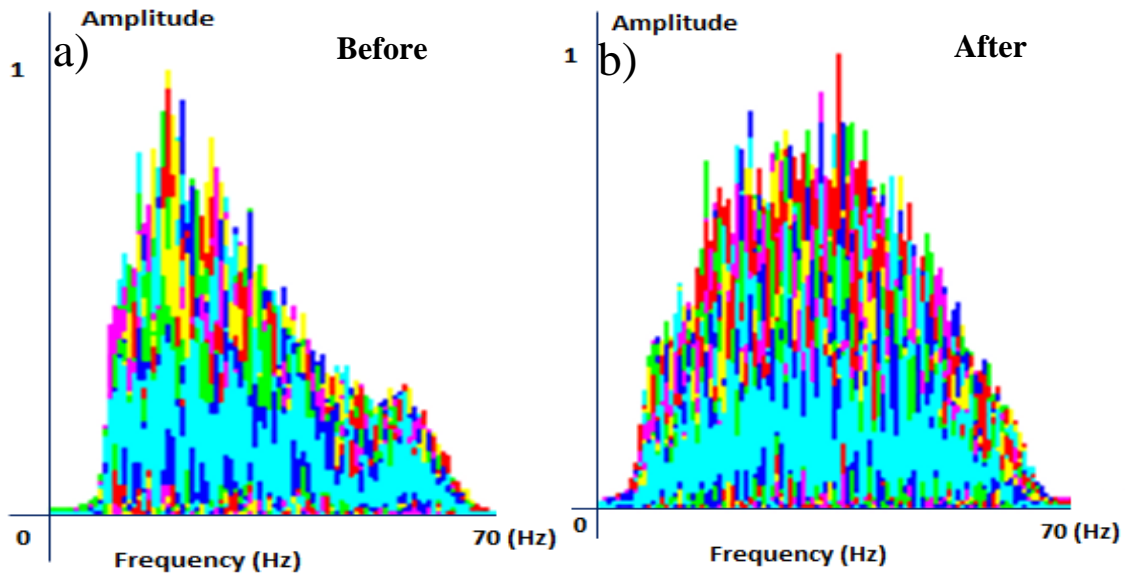


Figure 4.11. The amplitude spectrum of Line 45 before and after deconvolution. A: The amplitudes of higher frequencies are low. B: The amplitude spectrum of the Line 45 between 10 Hz and 70 Hz were flattened after deconvolution.

4.4 VELOCITY ANALYSIS

In this study, the conventional semblance approach (Taner & Koehler, 1969) was used. The conventional semblance was first proposed by Taner and Koehler (1969) and defined as a measurement of coherency (Sheriff, 1984). Semblance is used to determine the approximate velocity values for NMO correction. Neidell and Taner (1971) computed the semblance as:

$$S_{NT}[i] = \frac{\sum_{j=i-M}^{i+M} \left(\sum_{k=0}^{N-1} q[j,k] \right)^2}{N \sum_{j=i-M}^{i+M} \sum_{k=0}^{N-1} q[j,k]^2} \quad (3)$$

where i and j are the time sample values, k is the number of traces, $q[j,k]$ is the amplitude of a trace at time j and trace number k on an NMO corrected CDP. The inner and outer sums are N and $2M+1$. A smoothing in time is conducted using a boxcar. In addition, velocity semblance can be expressed as (Thomas, 1999):

$$\text{Semblance} = \frac{(\text{Amplitude})^2 \text{ of Stacked Trace}}{\text{Sum of } (\text{Amplitude})^2 \text{ of Unstacked Traces}} \quad (4)$$

The real events have mostly increasing velocities with depth. Incorrect velocities may cause an improper normal move-out correction. There are some rules to pick the velocities properly (Cochran, 1973). One of the most important rules is that RMS velocities generally have an increasing pattern towards the deeper parts of the seismic section. The second one is that the interval velocity between two formations must be higher than 2%.

Velocity picking is more accurate if the number of CDPs used for velocity picking is increased. Instead of using just one or two CDPs for velocity picking, ten CDPs from each seismic line were extracted for velocity analysis. CDPs were chosen with approximately 2 km intervals for Lines 45 and 46, and 3 km interval for Line 3C. Figure 4.12 shows a velocity semblance along with respective CDP gather. After the deconvolution, noise were removed and the low amplitudes of the reflections between 1 and 2 seconds were enhanced.

Generated velocity semblances only gives a prediction for the velocities of the primary reflections, the more accurate velocities can be determined using wells.

4.5. NMO CORRECTION

NMO correction is needed to remove the effect of the distance between the source and far offsets. The velocities acquired from the seismic section are used to apply the normal move-out correction and are called the normal move-out velocities (Yilmaz, 1987).

If the velocity is larger than the real velocity of the formation, then the reflection hyperbola will be undercorrected, or if the velocity is smaller than the real velocity of the formation, the reflection hyperbola will be overcorrected. If the velocity is close to the real velocity of the formation, the reflection hyperbola will be correctly flattened.

After applying NMO correction, especially for the far offset traces with small travel times, the frequencies are deteriorated (Figure 4.13) because the frequency values are decreased.

Severely deteriorated CDP gathers after the NMO correction should be muted to clear far offsets from distorted frequencies. The geological structures in shallow areas will be damaged if the mute is not applied, and this will make the interpretation impossible. In this study, an automatic mute was done during the NMO correction.

NMO correction was applied using the picked RMS velocities. After many trials, RMS velocities that flattened the reflections were determined. Figure 4.14 represents CDP 450 from Line 45 before and after NMO correction. Figure 4.15 shows multiple CDPs after the NMO correction. Primary reflections from the formations were flattened.

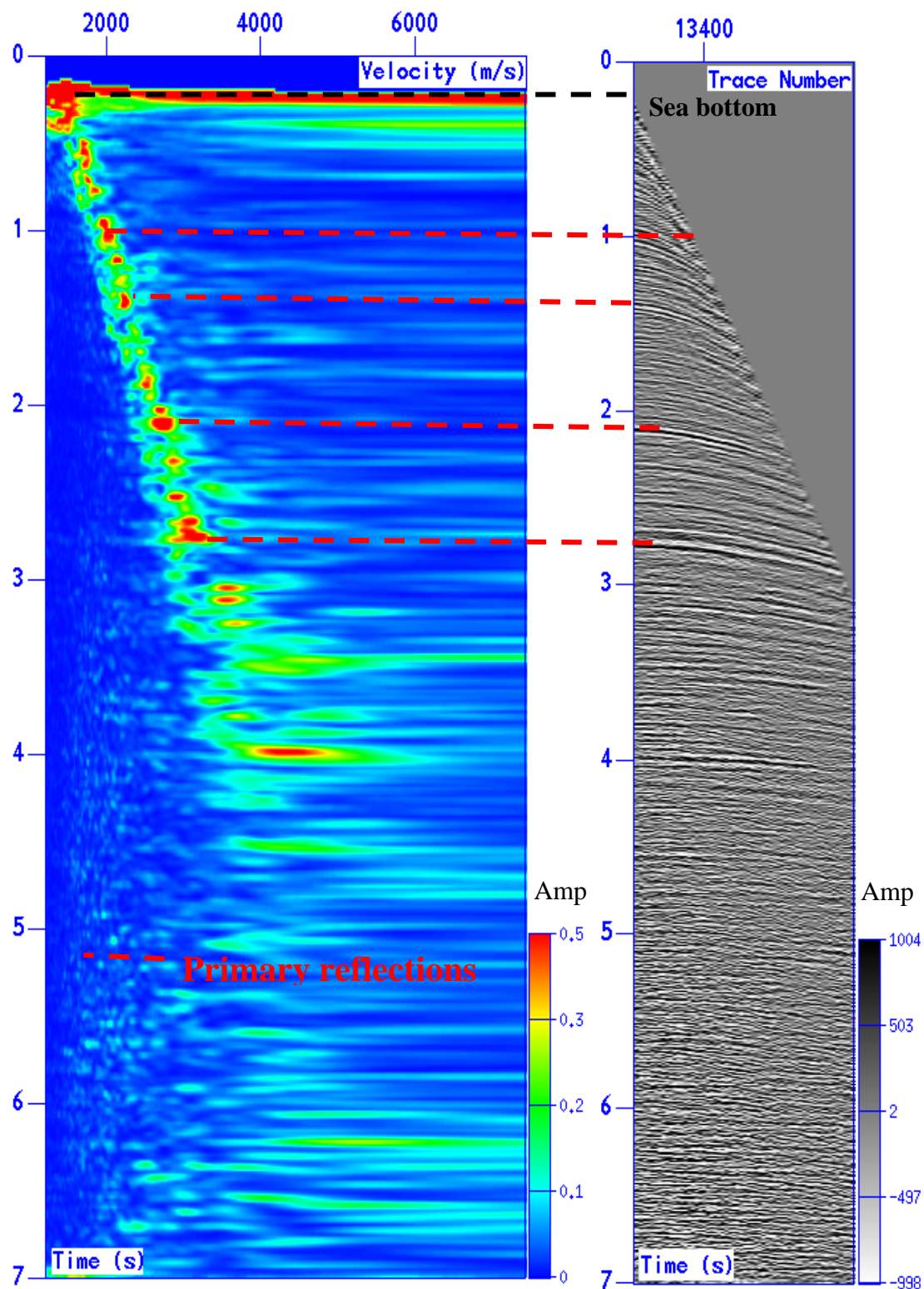


Figure 4.12. CDP 450 velocity spectrum and its CDP gather. The values of the semblance range from 1200 m/s to 7200 m/s. The scale shows the amplitude values for reflections.

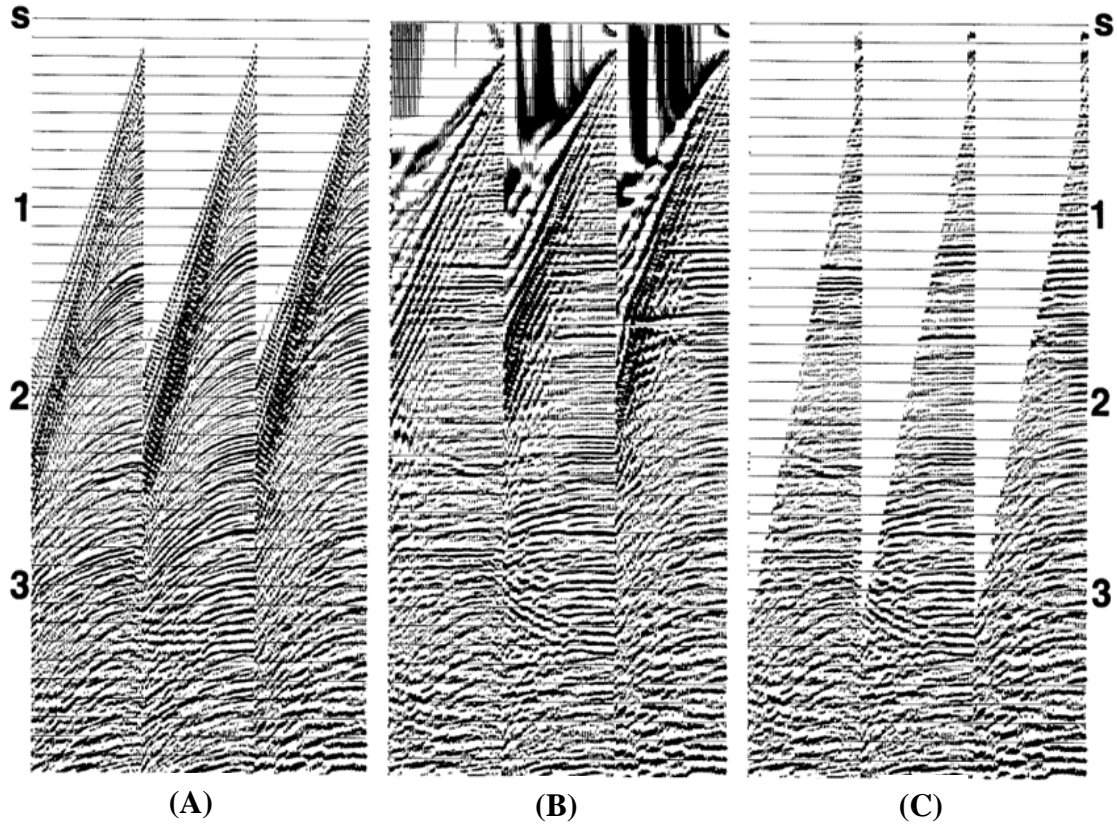


Figure 4.13. Three CDPs before and after NMO correction and stretching mute. A: CDPs before NMO correction. B: The deteriorated frequencies after NMO correction. Because frequencies are lower after NMO correction, a frequency stretching occurs and needs to be muted. C: The same CDPs after the deterioration of the frequencies have been muted (Yilmaz, 1987).

4.6. STACKING

After NMO correction, primary reflections were aligned in the CDP gathers. Aligning seismic reflections and suppressing the main noises provided a series of stacking-ready-CDP gathers. Entire traces of a seismic line became one stacked trace after all the traces were summed. Stacking is a significant method used to obtain a higher signal-to-noise ratio by suppressing much of the random noise. After stacking, data was transferred from pre-stack to post-stack data (Zhou, 2014).

By summing the CDP traces, seismic sections with higher resolution were acquired. Stacked sections of Lines 3C, 45, and 46 can be found in Figure 4.16. After 4.5 s, the data quality was really low for all three lines. During the processing, the target sections were chosen as faulted structures and anticlines. The data were removed for all three seismic lines since the absence of the geological structures that can be displayed after 4.5 s.

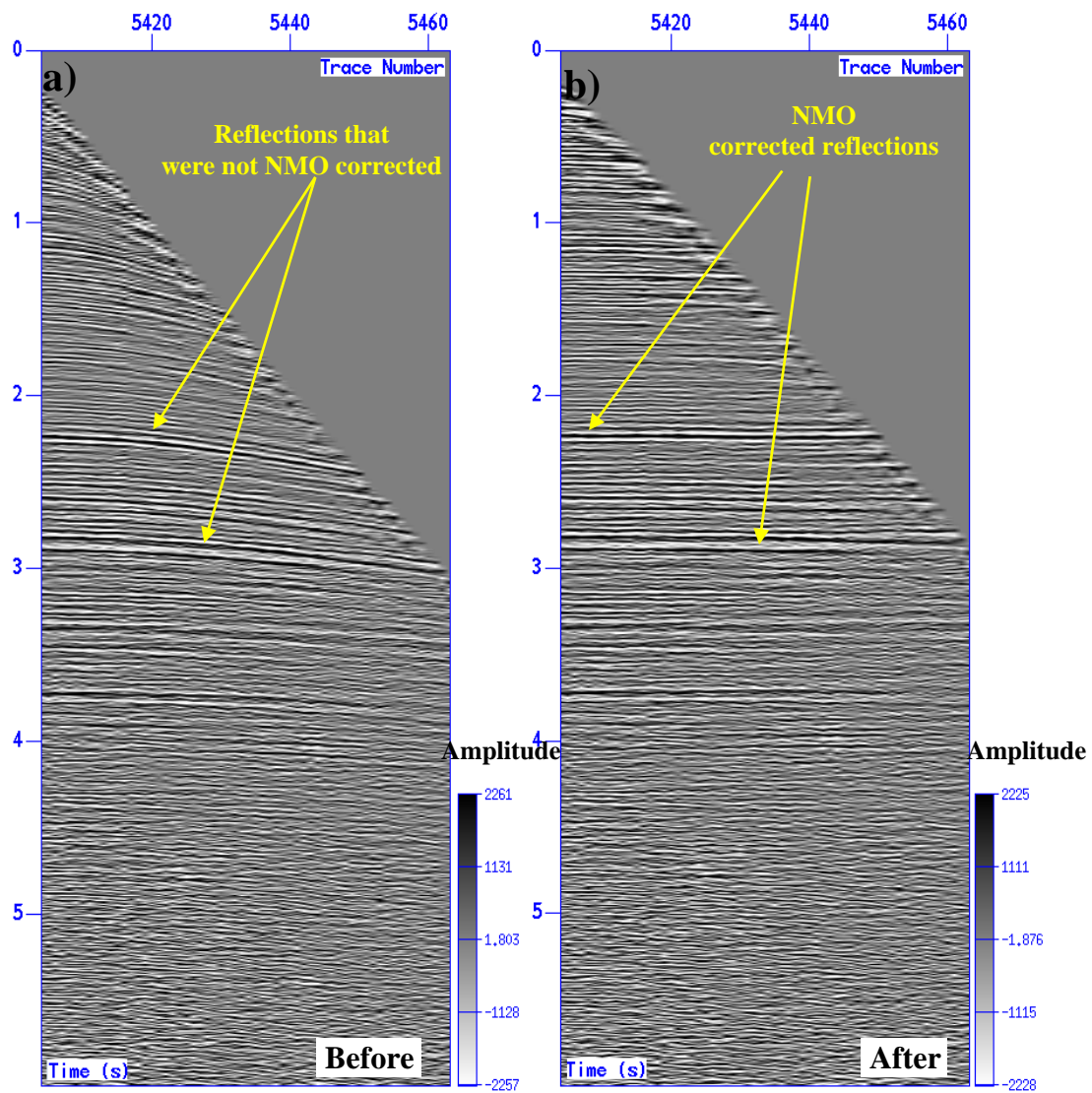


Figure 4.14. CDP 450 from Line 45 before and after NMO correction.

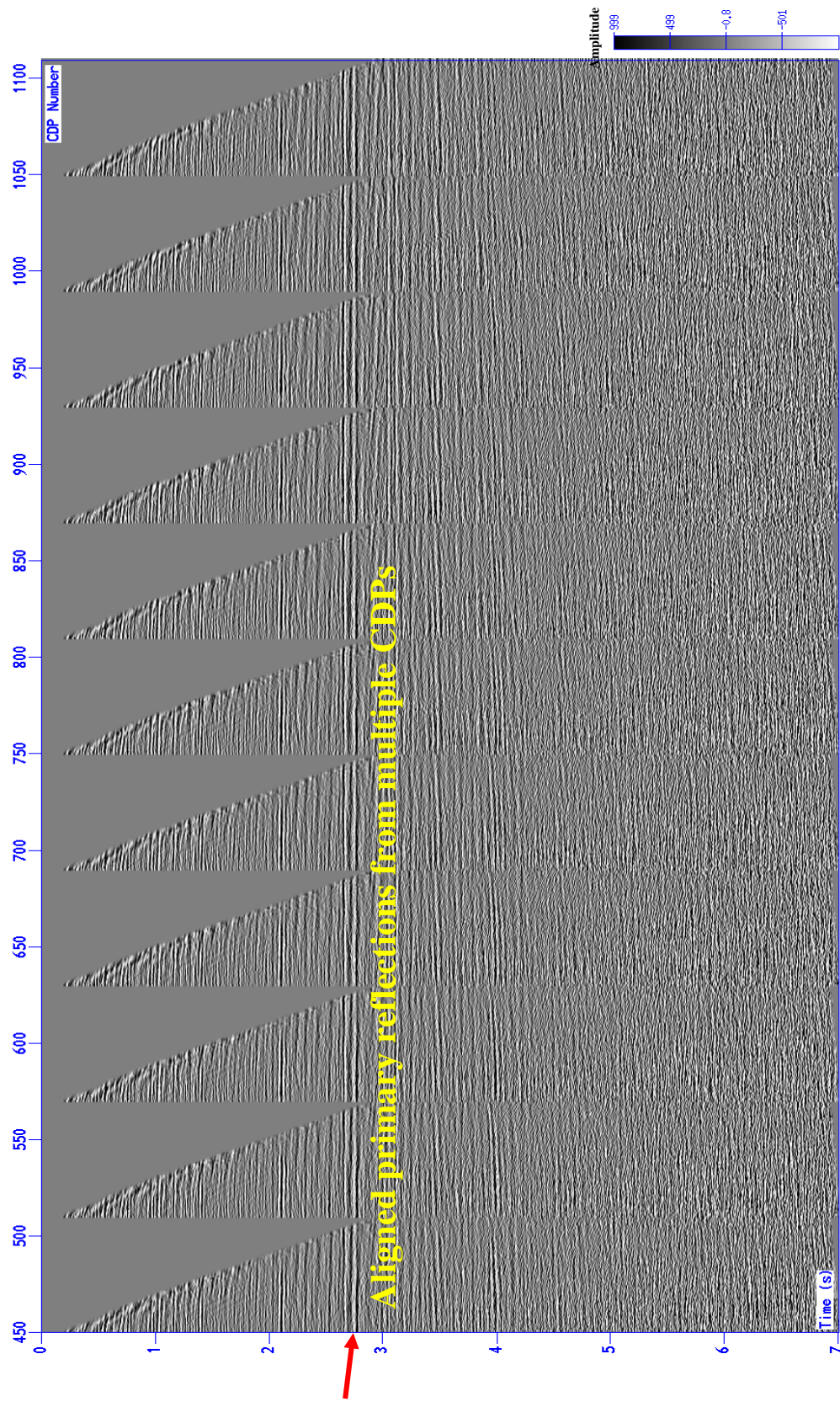


Figure 4.15. CDPs from Line 45 after the NMO correction. Aligned reflection from primary formation are shown with the red arrow.

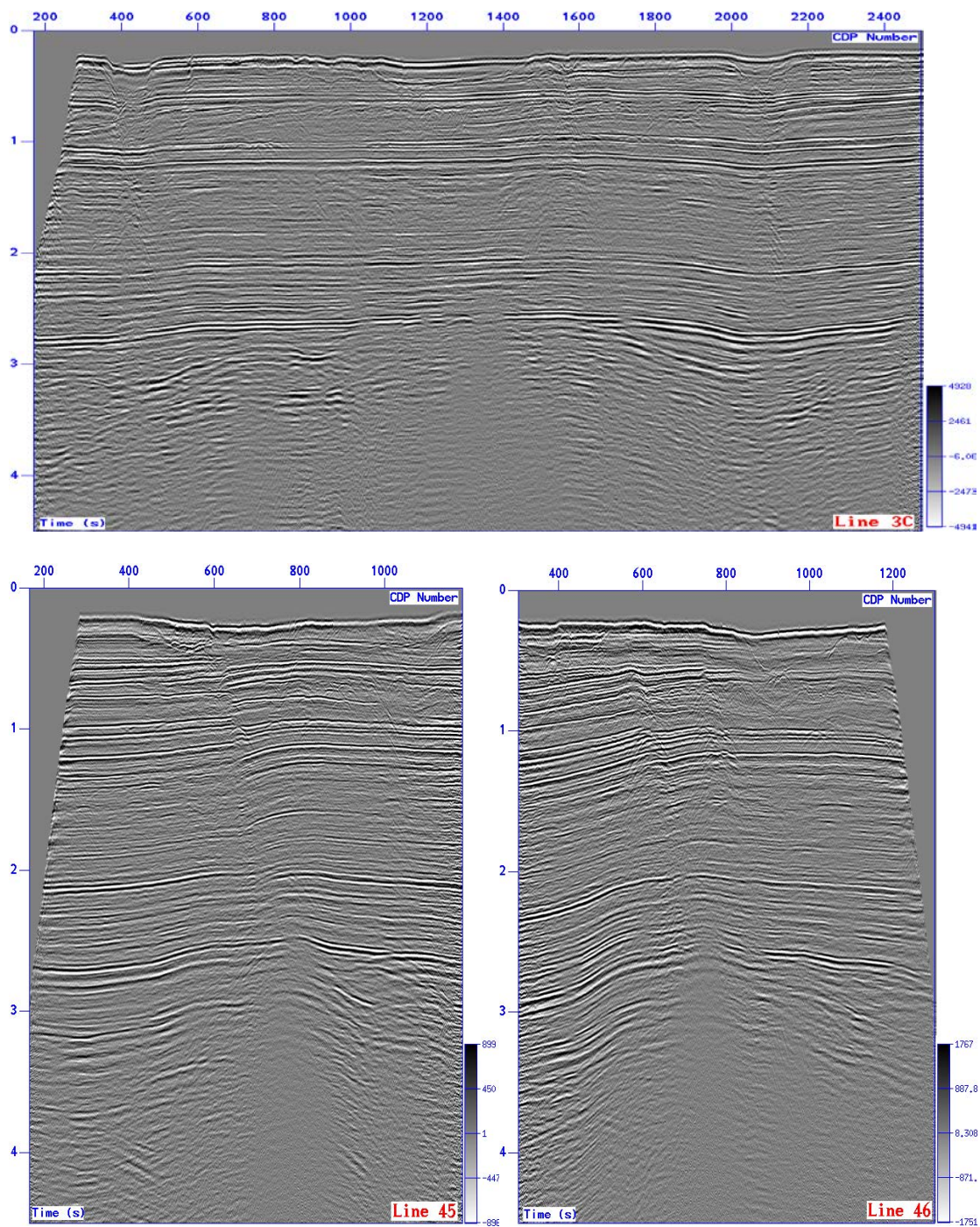


Figure 4.16. Lines 3C, 45, and 46 seismic sections after stacking.

4.7. MIGRATION

Geological structures such as faults, unconformities, and erosional surfaces in the target area may cause many diffractions. Most of the time, structures may not be in the real positions on the seismic section. Migration is used to bring geological structures to their true positions by removing diffractions and enhancing the temporal resolution.

Migration velocities are chosen very carefully because velocities that are higher than the true velocities create overmigrated sections. On the other hand, lower velocities than the real ones create undermigrated seismic sections. Figure 4.17 shows three different situation for seismic section of Line 46. Figure 4.17A has many diffractions that were not removed with migration. Figure 4.17B is the same figure, but it has many smileys that are occurred because of using high migration velocities. Figure 4.17C is a proper migration. The faults and sharp edges of the fracture surfaces can be observed.

One of the migration techniques, which is the base of the Stolt and Gazdag migration is the frequency-wavenumber method (Yilmaz, 1987).

4.7.1. The Frequency-Wavenumber (f-k) Method. The frequency-wavenumber (f-k) method is related to the migration methods of Stolt (1978) and Gazdag (1978). F-k migration gives faster results and is not affected by low signal-to-noise ratios as much as other methods. It provides better results if there are steeply dipping events in the seismic data (Chun & Jacewitz, 1981).

This method is conducted by importing the seismic data to the frequency domain using the Fourier transformation method. A structure with an angle in the time domain will be in the shape of radial lines in the f-k domain (Figure 4.18).

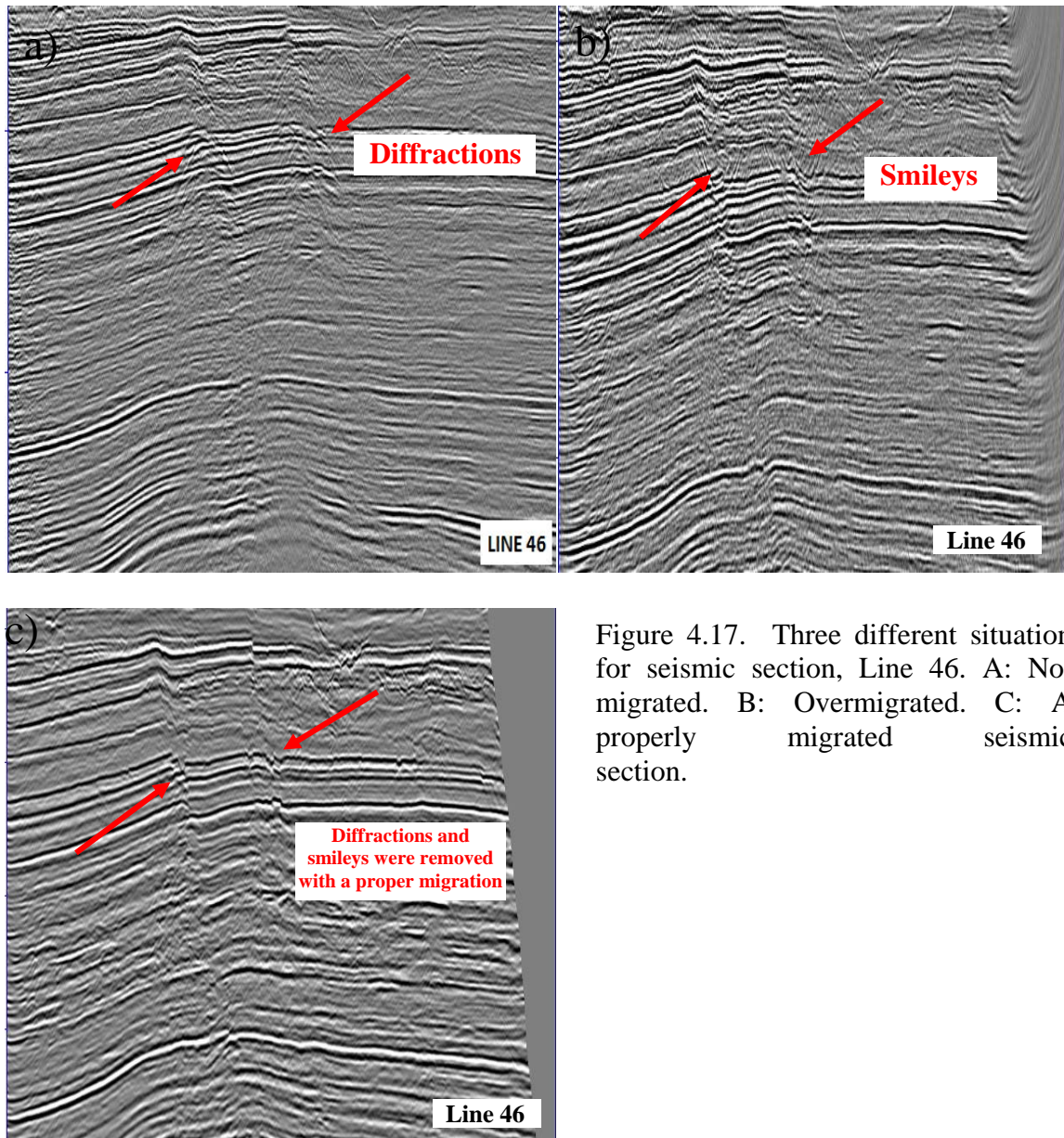


Figure 4.17. Three different situation for seismic section, Line 46. A: Not migrated. B: Overmigrated. C: A properly migrated seismic section.

Figure 4.18A shows the structures with angles in the time domain, and Figure 4.18B shows these events after migration in the f - k domain as lines. While the angle of the dipping event is increasing, the radial line in the f - k domain will go further away from the frequency axis (Yilmaz, 1987).

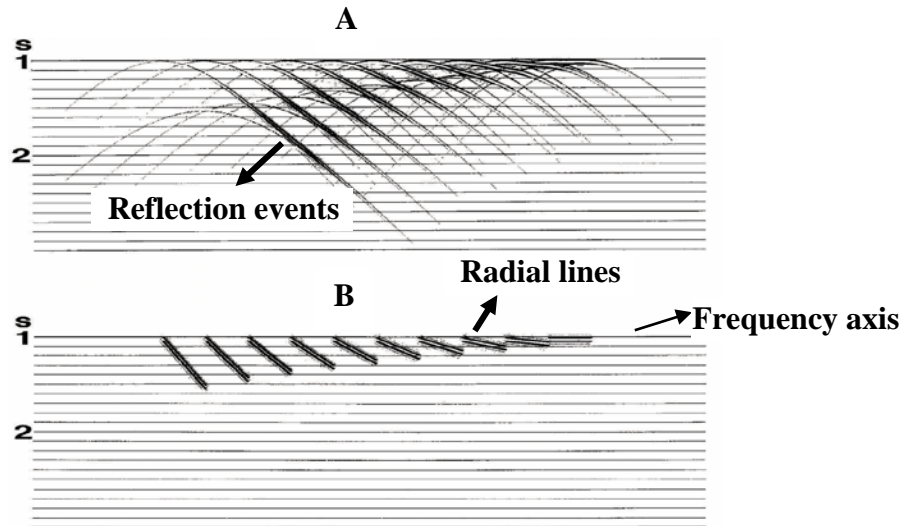


Figure 4.18. Diffractions in time and frequency domain. A: The diffractions in time domain. B: The diffractions as radial lines in f-k domain after migration (modified from Yilmaz, 1987).

In Figure 4.19, dipping event OB is shown in the frequency-wavenumber domain, after migration, OB is migrated to OB' in the vertical wavenumber (k_z) and the horizontal wavenumber (k_x) domains (Figure 4.19B). The frequency before migration is A, and Θ is the dip angle before migration. After migration, the dipping angle of the OB, Θ , is changed to $\bar{\Theta}$ but the wavenumber stays the same. The constant frequency in the ω - k_x domain is AB. After migration, A'B' is represented in the circle as the constant frequency in the k_z - k_x domain. F-k migration affects the dipping angle, and after the migration is performed, the f-k domain is converted to the t-x domain (Robinson, 1983).

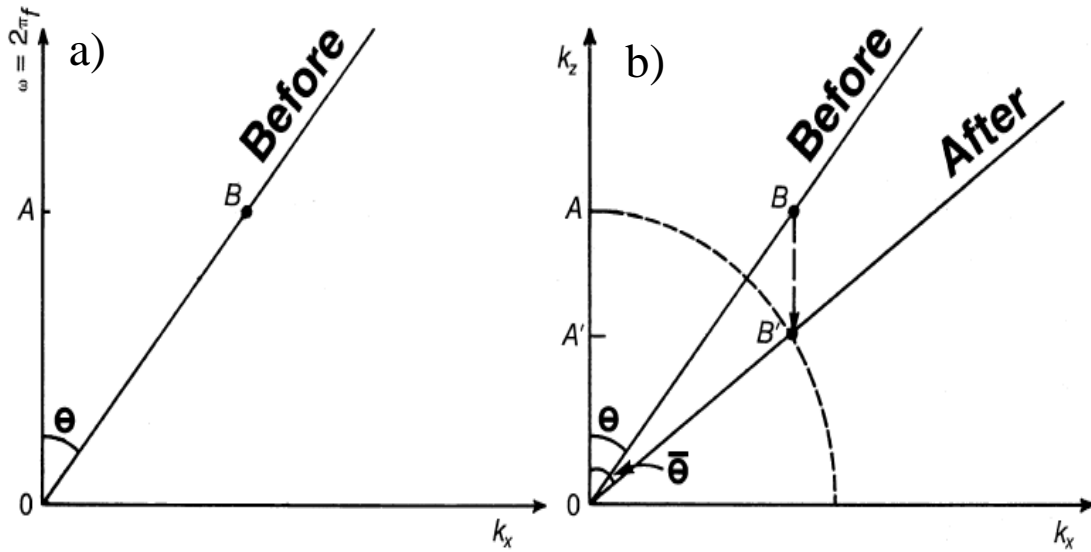


Figure 4.19. The migration of OB event in ω - k_x and k_z - k_x domains (Yilmaz, 1987).

4.7.1.1. Stolt migration. This method is designed to conduct migration in the f - k domain using the Fourier transformation (Stolt, 1978). During the application of the Stolt migration, the frequency axis is transferred into the vertical wave number axis, and the horizontal wave number axis stays the same as the horizontal wavenumber itself. The Stolt migration uses a constant velocity for the target area, and Stolt and Benson (1986) integrated this method with f - k methods (Yilmaz, 1987). The Stolt migration provides good results for the seismic section with vertical velocity variations (Margrave, 1998). The Stolt migration transfers the seismic data to the f - k domain, applies interpolation, and then makes a move-out correction (Burnett & Ferguson, 2008). By this approach, Stolt migration system reminds NMO correction process (Burnett, 2008a). The equation for the Stolt migration is (Stolt, 1978):

$$P(k_x, k_z, t=0) = \left(\frac{v}{2} \frac{k_z}{\sqrt{k_x^2 + k_z^2}} \right) \quad (5)$$

$$P \left(k_x, 0, \omega = \frac{v}{2} \sqrt{k_x^2 + k_z^2} \right)$$

The migrated zero-offset seismic section in the frequency wavenumber domain is represented by $P(k_x, k_z, t=0)$ (Yilmaz, 1987). The wavenumbers at the x and z directions are k_x , and k_z . Applying Fourier transform to the $P(k_x, z=0, \omega)$ immigrated section allows $P(k_x, k_z, t=0)$ to be acquired in Equation 5. Dispersion relation (Berryman, 1979; Thomsen, 1986) is then applied to convert temporal frequency (ω) domain to the k_z wavefield domain using Equation 6:

$$\omega = \frac{v}{2} \sqrt{k_x^2 + k_z^2} \quad (6)$$

S scaling factor is then used with Equation 7 for a necessity of conversion:

$$S = \left(\frac{v}{2} \frac{k_z}{\sqrt{k_x^2 + k_z^2}} \right) \quad (7)$$

Where $P(k_x, k_z, t=0)$ is obtained by giving 0 to t. The inverse Fourier transform is applied to $P(k_x, k_z, t=0)$, and the final migrated section is gathered.

The velocity of the layers beneath the surface changes with depth, and the Stolt migration assumes that a constant velocity is valid for all the layers. To compensate the velocity variation problem, Stolt added a stretching factor that is added in the time direction

and provided a solution for this problem (Yilmaz, 1987). A stretching factor was chosen as 1 in this study to compensate velocity variations.

4.7.1.2. Gazdag (phase shift) migration. The Gazdag migration brings the dipping structures to their true positions on seismic sections using a phase shift in the Fourier domain. Gazdag is a wave-equation based method (Gazdag, 1978; Gazdag & Sguazzero, 1984). The phase-shift method was discovered by Gazdag (1978). This method handles small lateral velocity changes and ray bending problems caused by seismic refraction. The Gazdag migration is expressed using Equation 8 (Gazdag, 1978):

$$q(\tau, k) = \frac{1}{2\pi} \int d\omega e^{-i\omega \int_0^\tau d\sigma \sqrt{1 - \frac{v^2(\sigma)k^2}{4\omega^2}}} P(\omega, k) \quad (8)$$

where q is the migrated data. First data (q) is Fourier transformed and multiplied by a complex exponential, which consists of an integral, and integrated over frequency ω (Mikulich & Hale, 1992). The Fourier transformed data is $P(\omega, k)$. The two way vertical (migrated) time is τ and k is the wavenumber.

After CDP stacking many diffractions were observed especially around the sharp edges of the faulted structures (Figure 4.20). As a result, major fault and minor fractures were covered by diffractions, which makes the structural interpretation impossible. Line 3C had diffractions mostly between horizontal layers (Figure 4.20).

The Stolt migration was utilized to remove diffractions. Compared to other migration methods, Stolt migration was a powerful method with a shorter processing time. However, a constant velocity was applied to whole section in the Stolt migration. Therefore it did not compensate the velocity variations. Formations and geological structures that

have higher velocities and lower velocities than the constant velocity were not migrated properly.

After migration, many scattered noises were observed on Lines 45 and 46 because of the low and high frequency noise content (Figure 4.21). Migration were applied to Line 3C after frequency filtering because the application of the migration before filtering created unexpected noise that cannot be removed by any filter.

The migration velocity for Line 46 was determined to be 2025 m/s around 2 seconds, and the chosen velocity revealed the faults between 1 and 1.5 seconds with sharper edges after migration. The rest of the main fault between 2 and 3 seconds was not sharp enough. The attempts to make the faults sharper were only successful for shallow parts of the seismic section using the Stolt migration (Figure 4.22). Next, the Gazdag migration was applied to collapse the diffractions around the fractures. The velocities for the Gazdag migration were chosen to be 1800 m/s between 0 to 2 seconds and 3000 m/s between 2 and 4 seconds (Figure 4.23).

Line 3C has a different processing sequence because of its different structural nature. Stolt with a velocity of 2000 m/s removed the diffractions successfully between the horizontal layers (Figure 4.24). Band-pass and f-k dip filter with RMS amplitude AGC were applied before the Stolt migration decreased the artifacts that occurred as a result of migration. Low frequency (<10 Hz.) and high frequency noise (>50 Hz) content of Line 3C were removed before the migration.

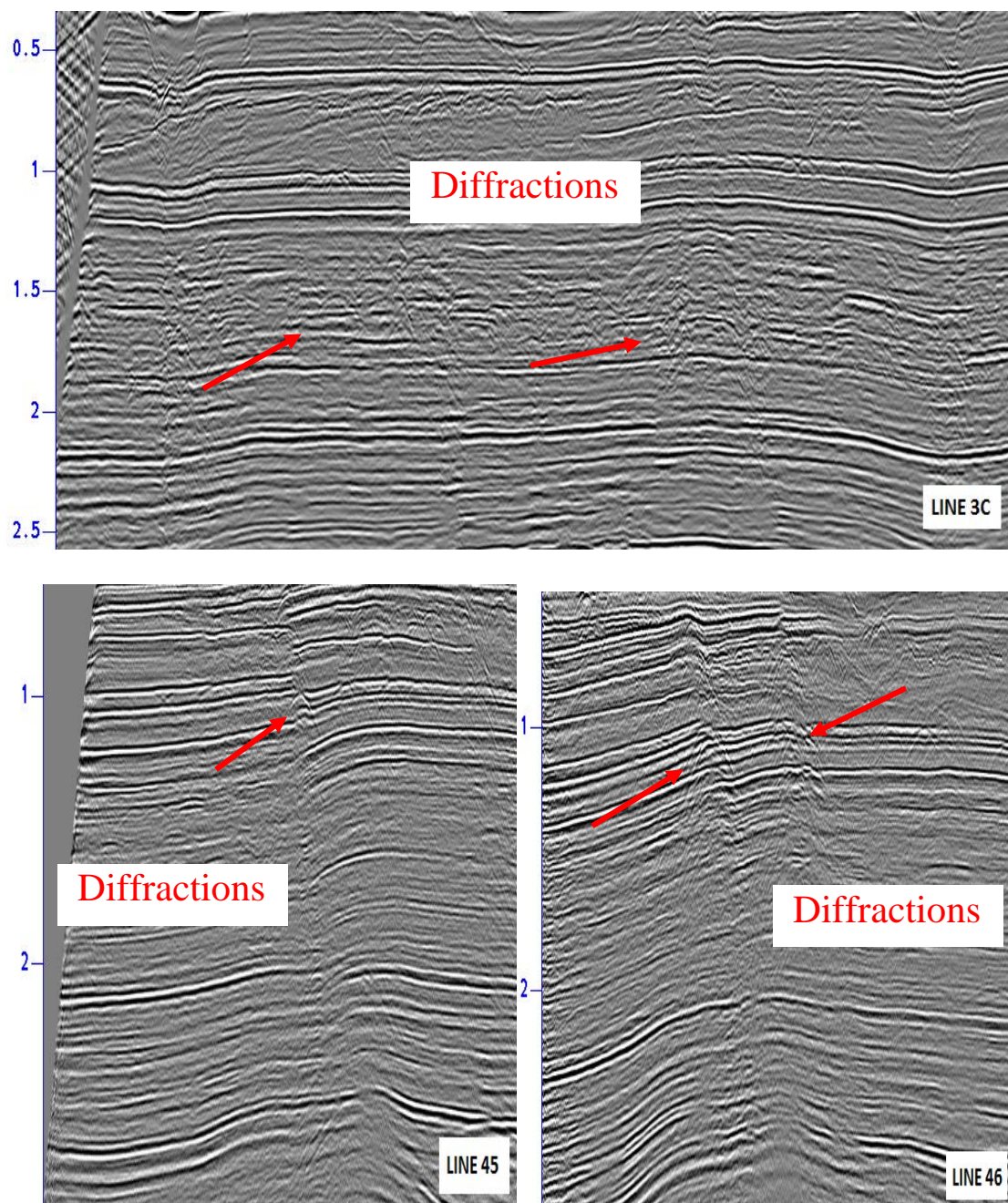


Figure 4.20. Seismic sections with strong diffractions. Line 3C has diffractions mostly between the primary reflections (red arrows) between 1.2 and 2.1 seconds. Lines 45 and 46 have strong diffractions around faults for the entire seismic sections.

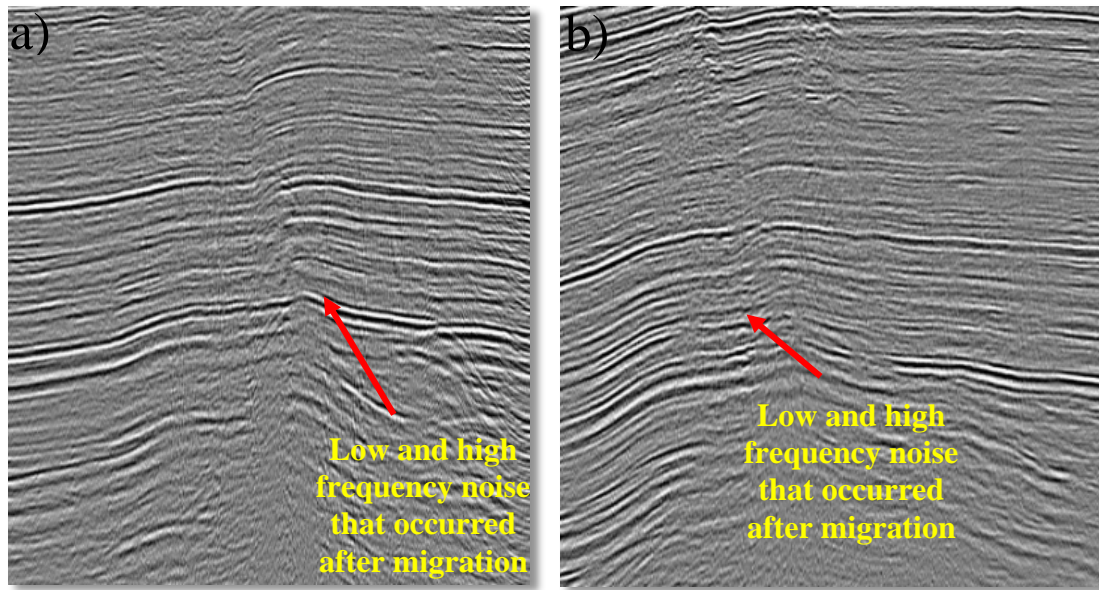


Figure 4.21. Random noise on seismic sections after migration. A: Line 45, B Line 46. Vertical scattered noise was observed after the migration because the data still has low and high frequency noise.

The Stolt migration velocity for Line 45 was determined as 2100 m/s. The migration removed the diffractions until 2 seconds. However, high velocity formations still had diffractions after 2 seconds, and the main fault was not as sharp as it needed to be (Figure 4.25). Stolt migration was applied again using 2650m/s velocity (Figure 4.26). Figure 4.26 shows that the main fault is sharper after 2 seconds (Yellow arrows). However, this trial showed that 2650 m/s is a high velocity for shallower parts of the seismic section and, at 1 second, smileys occurred (Purple arrow) because of a higher than the real velocity. Minor faults between CDPs 590 and 675 at 0.8 seconds are also less visible than Stolt migration with a velocity of 2100 m/s (Yellow Square) (Figure 4.26).

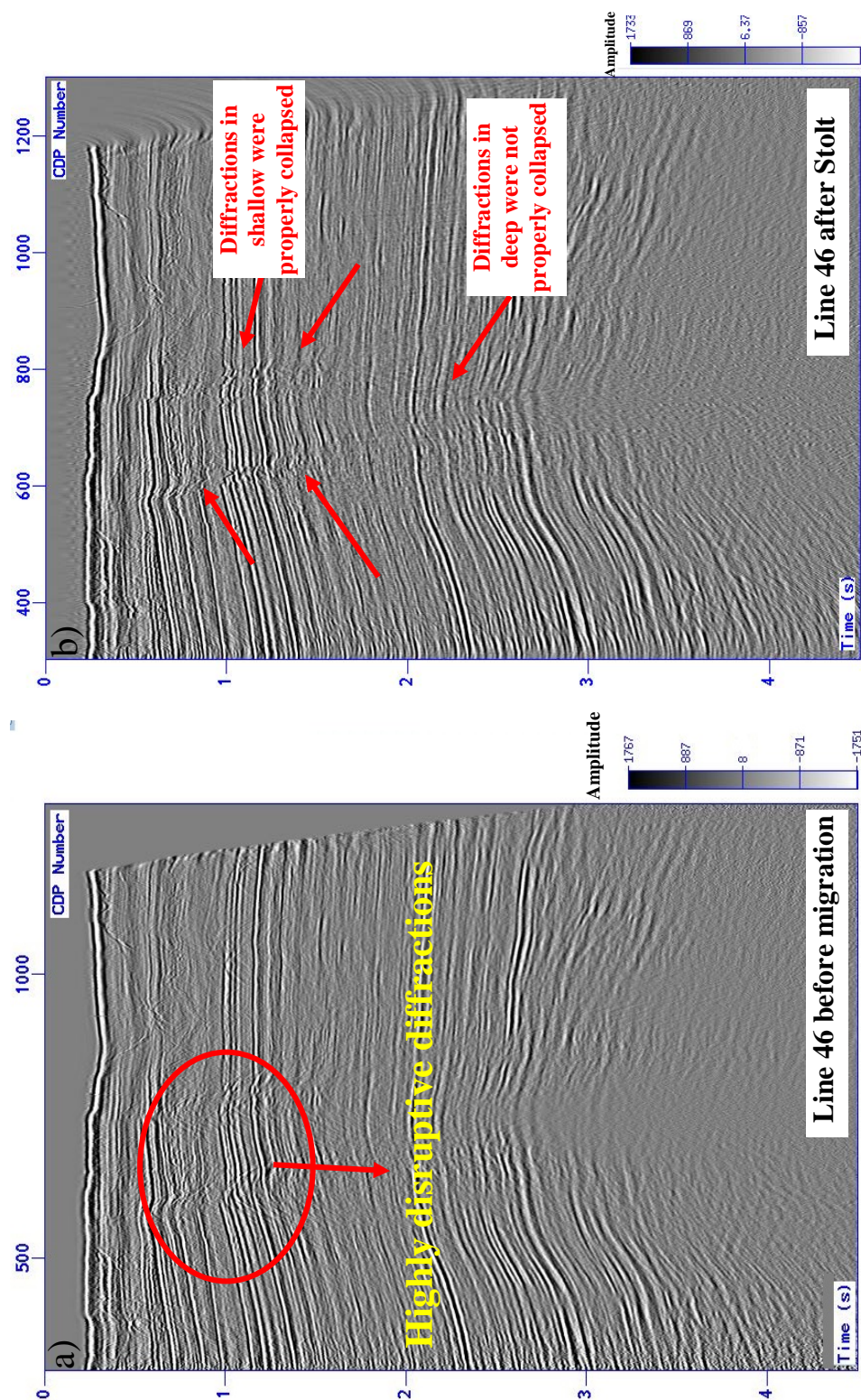


Figure 4.22. Line 46 before and after the Stolt migration with a velocity of 2025 m/s. Diffractions around the faults were removed and the edges of the faults around 1.1 seconds are visible. The Stolt migration did not reveal the fault well deeper than 2 seconds for Line 46 (Line 46 is 11.7 km long).

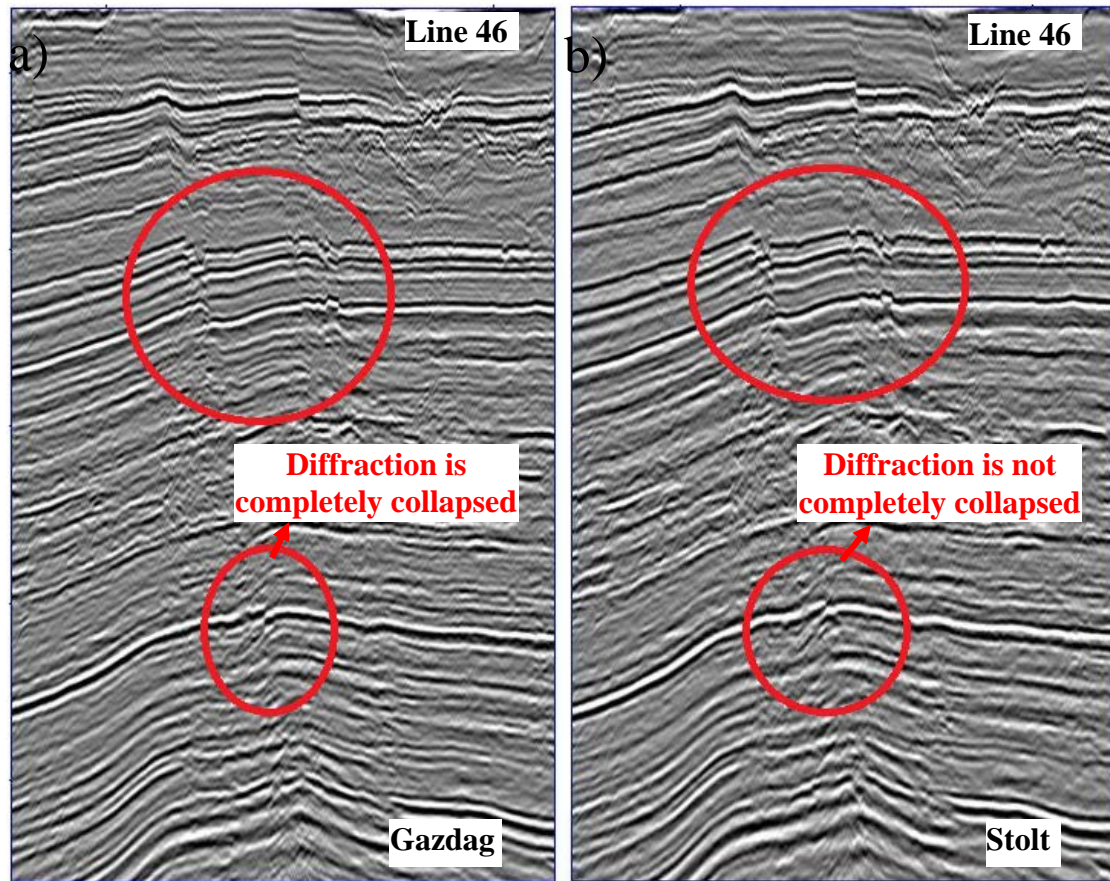


Figure 4.23. Gazdag and Stolt migrations of Line 46. A: Gazdag migration with velocities of 1800 and 3000 m/s. B Stolt migration with a velocity of 2025 m/s. In Gazdag migration, the diffractions were collapsed around the major fault in the deeper part, which was shown in small red circle. However, improvements are not significant between Gazdag and Stolt migrations.

Gazdag were applied to Line 45 with velocities of 2000 and 3100 m/s (Figure 4.27). Gazdag removed the diffractions successfully from both the shallow and deep parts at the same time (Figure 4.27). As a result, Gazdag migration were chosen as the migration type for structural interpretation.

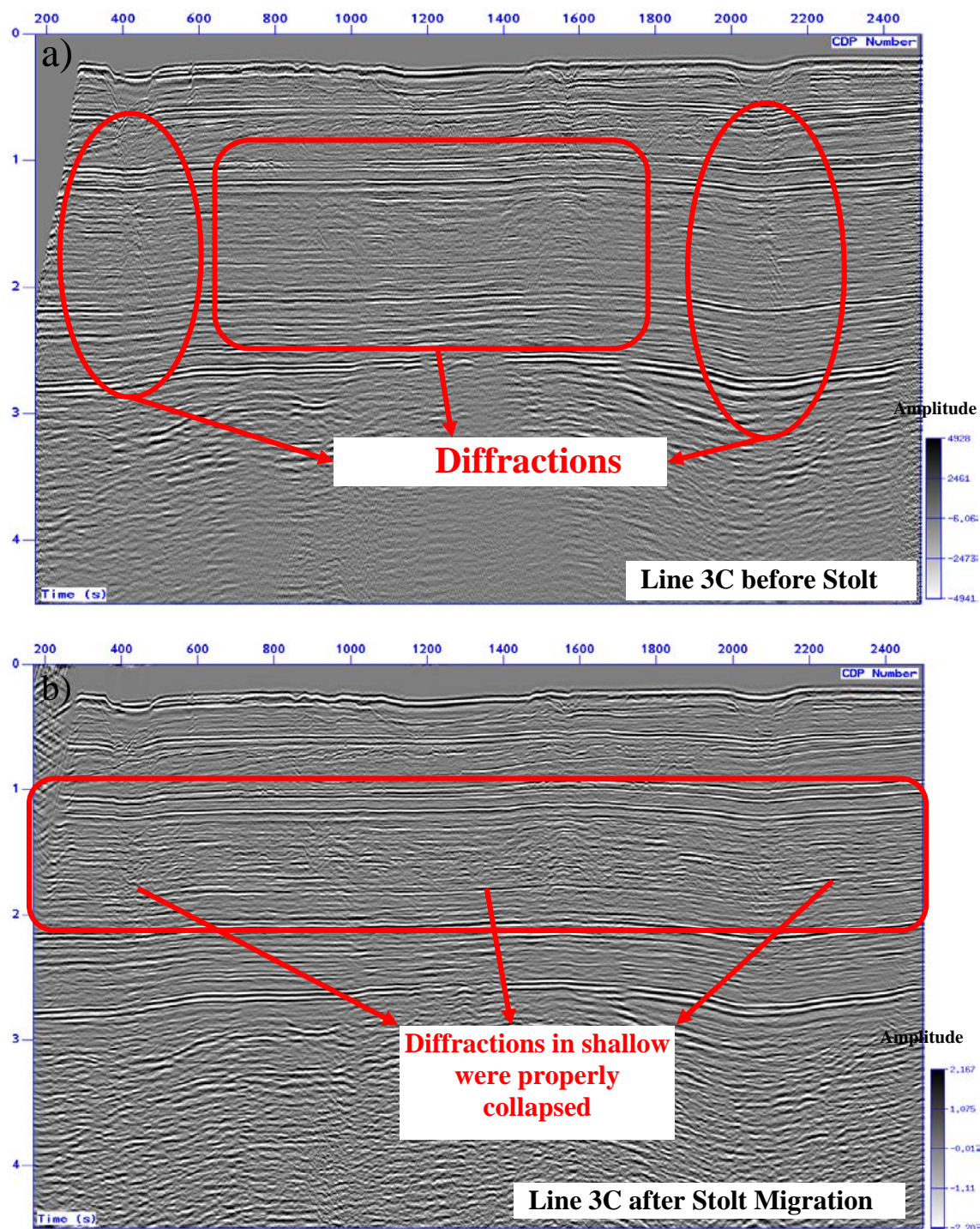


Figure 4.24. Line 3C before and after Stolt migration. A: Line 3C before Stolt migration. B: Stolt migration with a velocity of 2000 m/s for Line 3C (Line 3C is 29.9 km long).

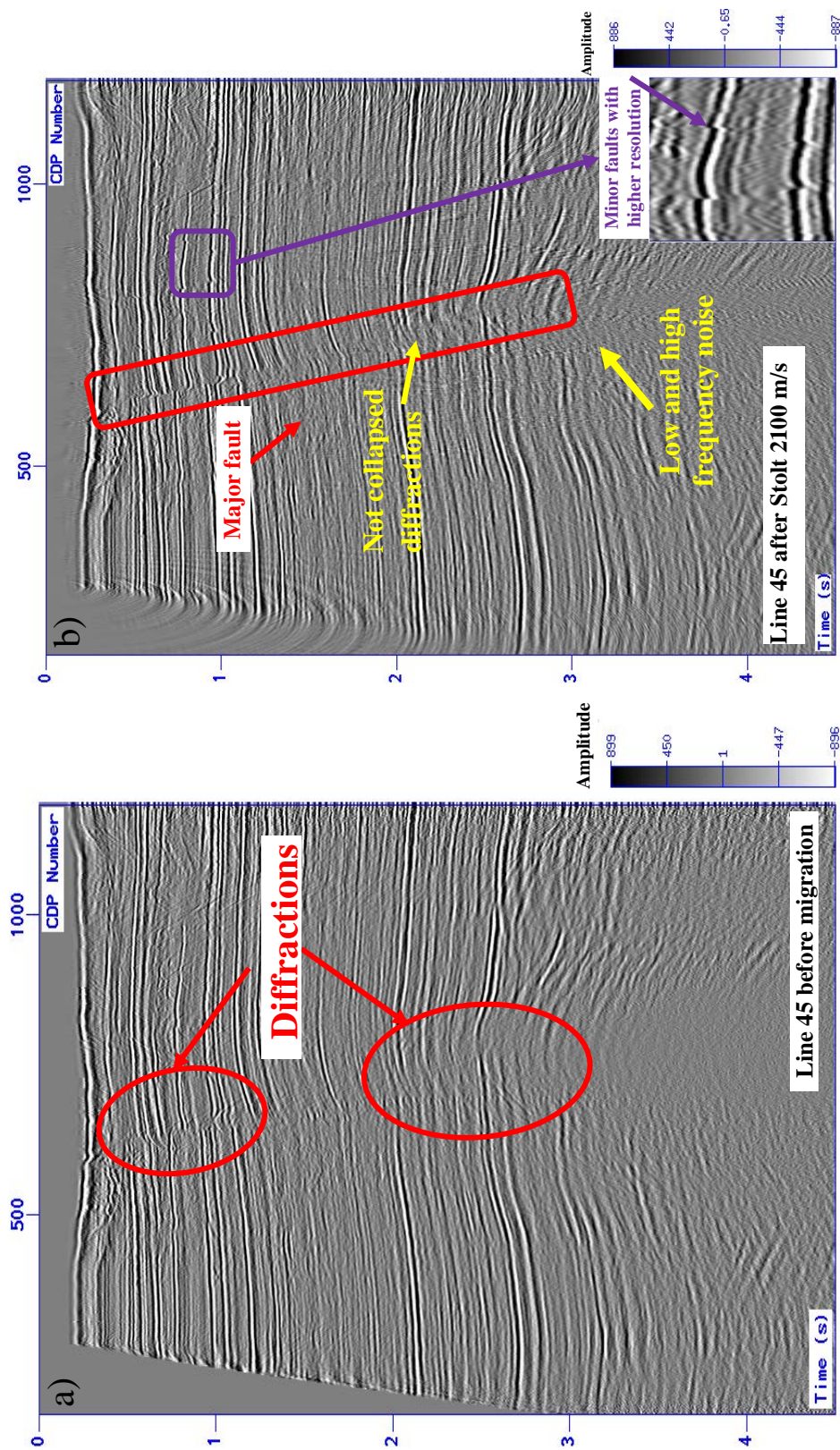


Figure 4.25. Line 45 before and after migration (with a velocity of 2100 m/s). Diffractions at the shallower parts were successfully removed, but the deeper parts still have diffractions around the main fault. Also minor faults at the 0.8 seconds around the 800th cdp are visible with the chosen velocity (Line 45 is 11.9 km long).

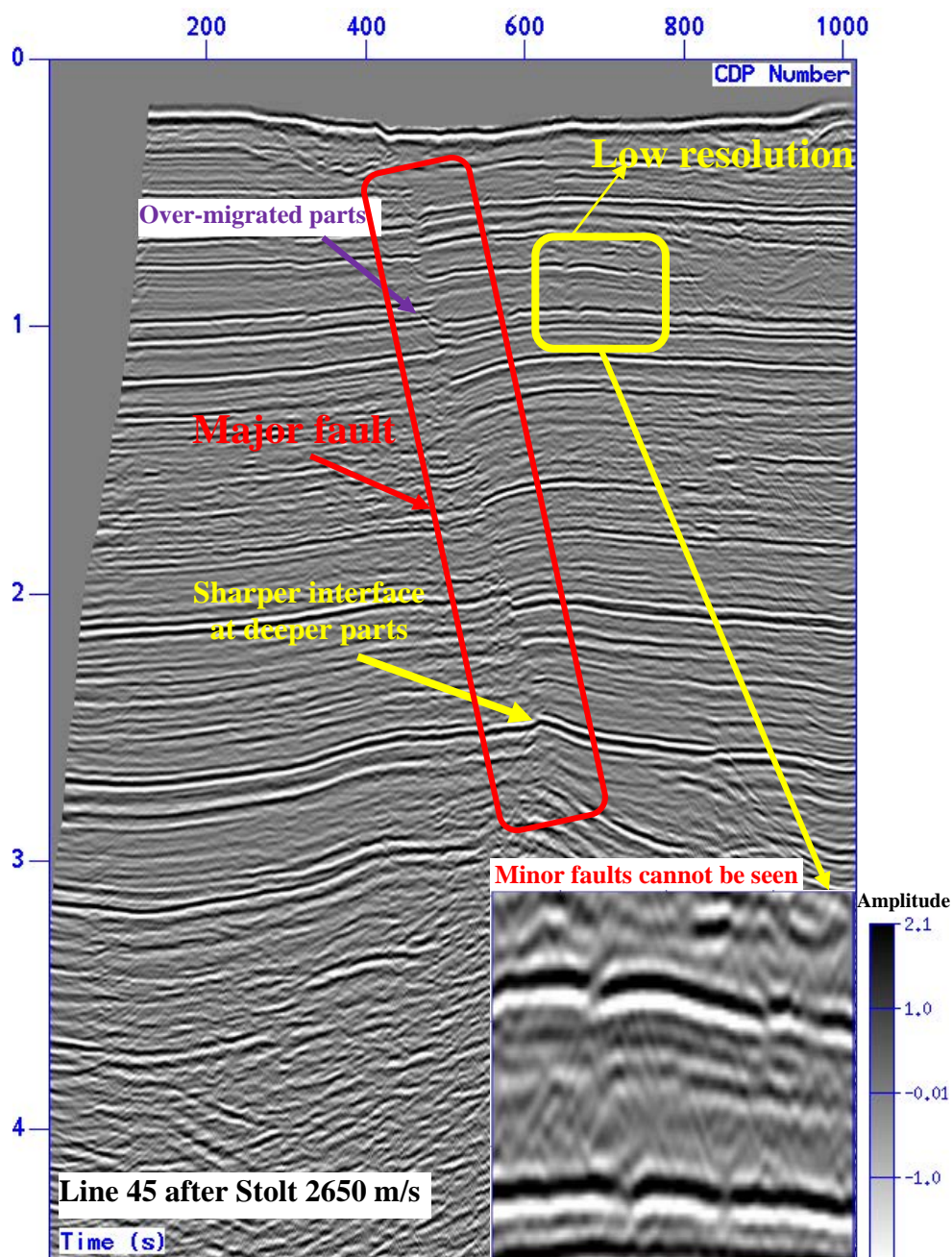


Figure 4.26. Line 45 after Stolt migration with a velocity of 2650 m/s. Diffractions that prevent observing the main fault after 2 seconds were removed successfully. However, shallower events, such as minor faults, were disappeared (Just for comparing purposes, other processing steps were not represented here) (Line 45 is 11.9 km long).

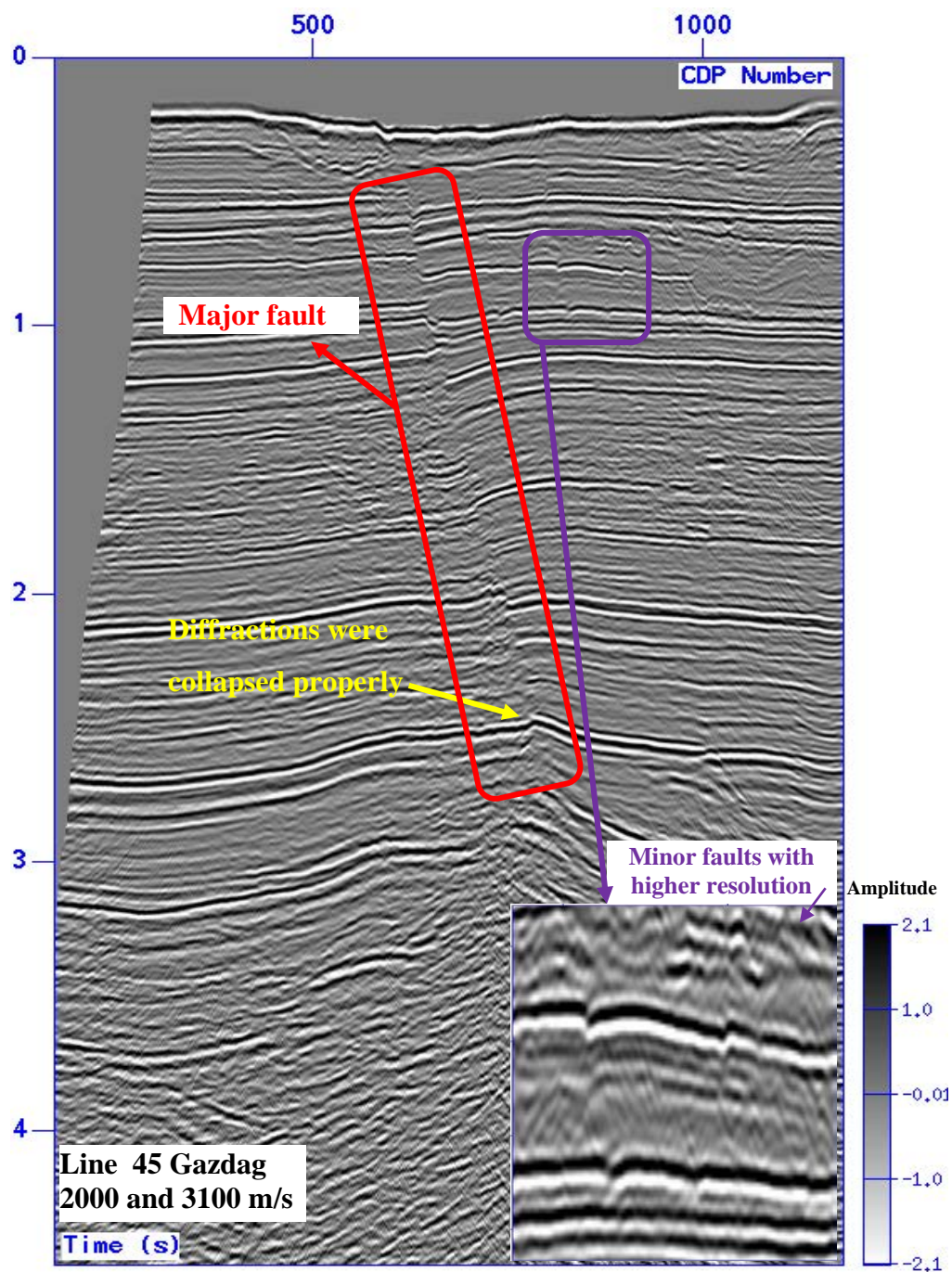


Figure 4.27. Line 45 after the Gazdag migration. The main fault is sharp between 0.5 seconds and 3 seconds (red box). Diffractions were removed successfully and shallow events at 0.8 seconds is revealed properly (yellow box) (Line 45 is 11.9 km long).

4.8. BAND-PASS ZERO PHASE FILTER AND SLOPE FILTER

Filters in the time and frequency domain are used to attenuate disrupting noise, frequency filtering allows the signal to be enhanced so that geological structures may be interpreted more easily.

Frequencies of signal and noise are in different ranges, and determination of the noise frequencies makes it easier to design a frequency filter. The amplitude spectrum versus frequency in Figure 4.28 shows a general approach to frequency ranges of noise and the real signal. Swell noise and cable noise are low-frequency noises, and the noises caused by wind, instrument are high-frequency noises.

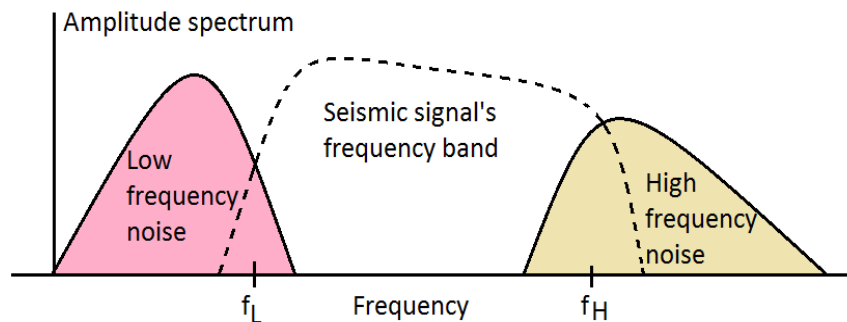


Figure 4.28. The frequency ranges of the noise and signal in an amplitude spectrum. f_L is the intersection of the seismic signal with the low frequency noise and f_H is the intersection of the seismic signal with the high frequency noise.

A band-pass filter is designed using four corner frequencies and it is a conventional method. In addition to band-pass filter, a f-k dip filter were designed and applied to the data to remove dipping noise and to smooth the data.

Slope filtering (f-k dip filter) is done by converting the data from the time domain to the frequency domain. Noise with the angle can be removed using this type of filter.

Seismic data will also have a smoother visualization after slope filtering. The filter was designed as a band-pass slope filter and did not change the frequency content of the data as much as the other filters. However, by smoothing the data, the slope filter made faults, formations, and geological structures more visible. The slopes of this filter were determined using the apparent velocities (Robinson, 2000):

$$\text{Slopes} = dt/dx = 1/V_{\text{app}} \quad (9)$$

Slopes were determined as -2, -0.5, 0, 0.5 and 2. After many trials, selected slopes of the f-k dip filter were applied to entire seismic sections.

Migration created many artifacts because of the low and high-frequency content of Lines 45 and 46 (Figure 4.21). A zero phase sine-squared tapered filter was applied to remove frequencies lower than 10 Hz and higher than 50 Hz, which were occurred as artifacts of the migration. A f-k dip filter was then applied to remove noise with an angle. This procedure was applied to Line 3C before migration because frequency filtering after migration generated a different kind of disruption on Line 3C. All sections were cleared of low and high-frequency noise. Figure 4.29 shows the frequency spectrum of Line 45 before and after filtering. The frequency spectrum of the other two seismic lines were pretty similar. High amplitude frequencies are located between 10 and 50 Hz. Figures 4.30, 4.31, and 4.32 show the seismic sections after filtering for Lines 45, 3C, and 46, respectively.

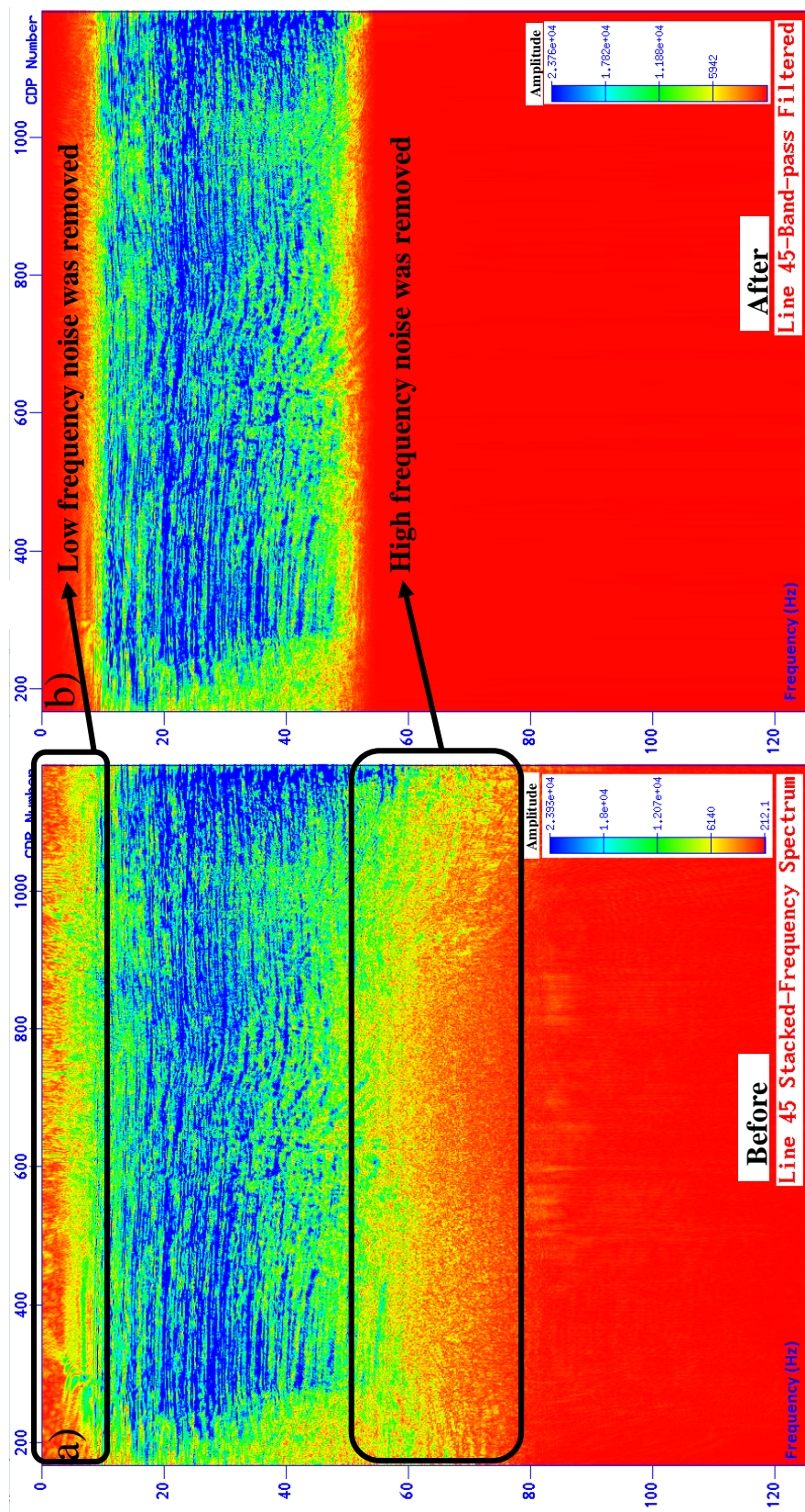


Figure 4.29. The frequency spectrum of Line 45. A: The frequency spectrum of Line 45 before band-pass frequency filter. B: The frequency spectrum after the filter. The frequencies between 10 and 50 Hz were preserved and the other frequencies were interpreted as noise and removed.

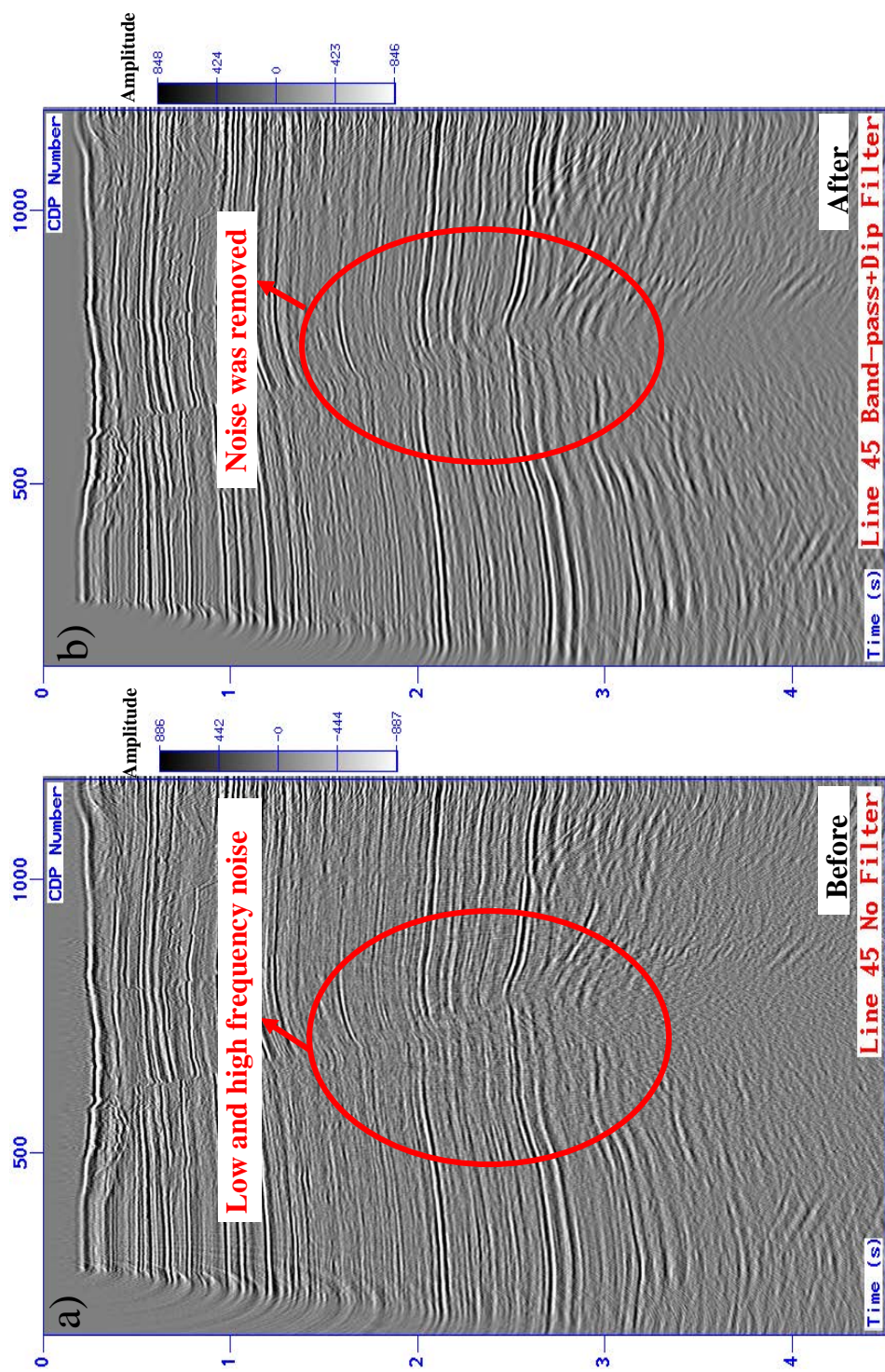


Figure 4.30. Band pass and f-k dip filters for Line 45. A: Line 45 after migration with many vertical scattered noise. B: Line 45 after the application of the band-pass and slope filter. Most of the vertical scattered noise were removed and section was smoothed by slope filter (Line 45 is 11.9 km long).

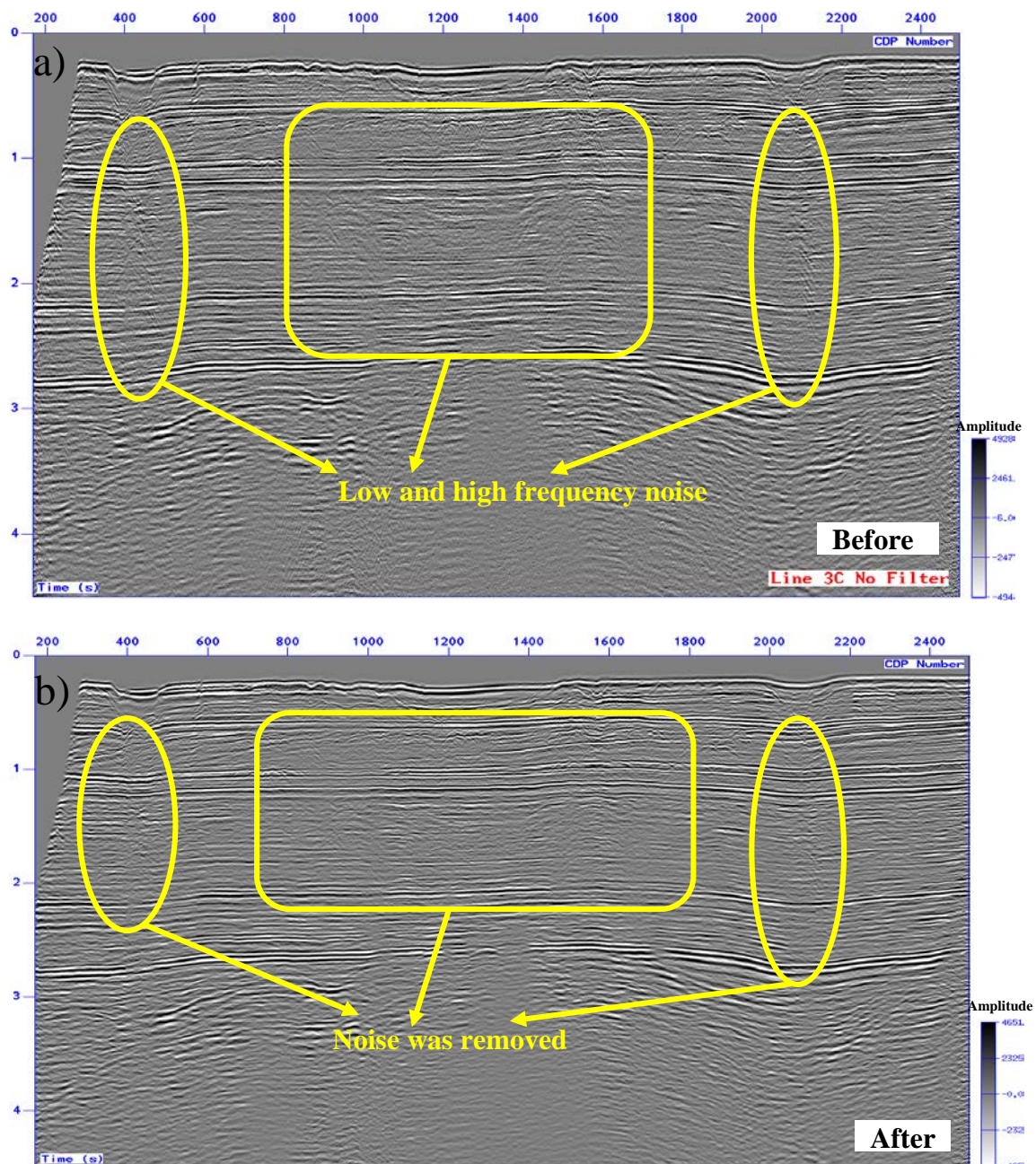


Figure 4.31. Band pass and f-k dip filters in Line 3C. A: Line 3C before application of the filters. B: After filtering. The frequencies lower than 10 Hz and higher than 50 Hz were removed (Line 3C is 29.9 km long).

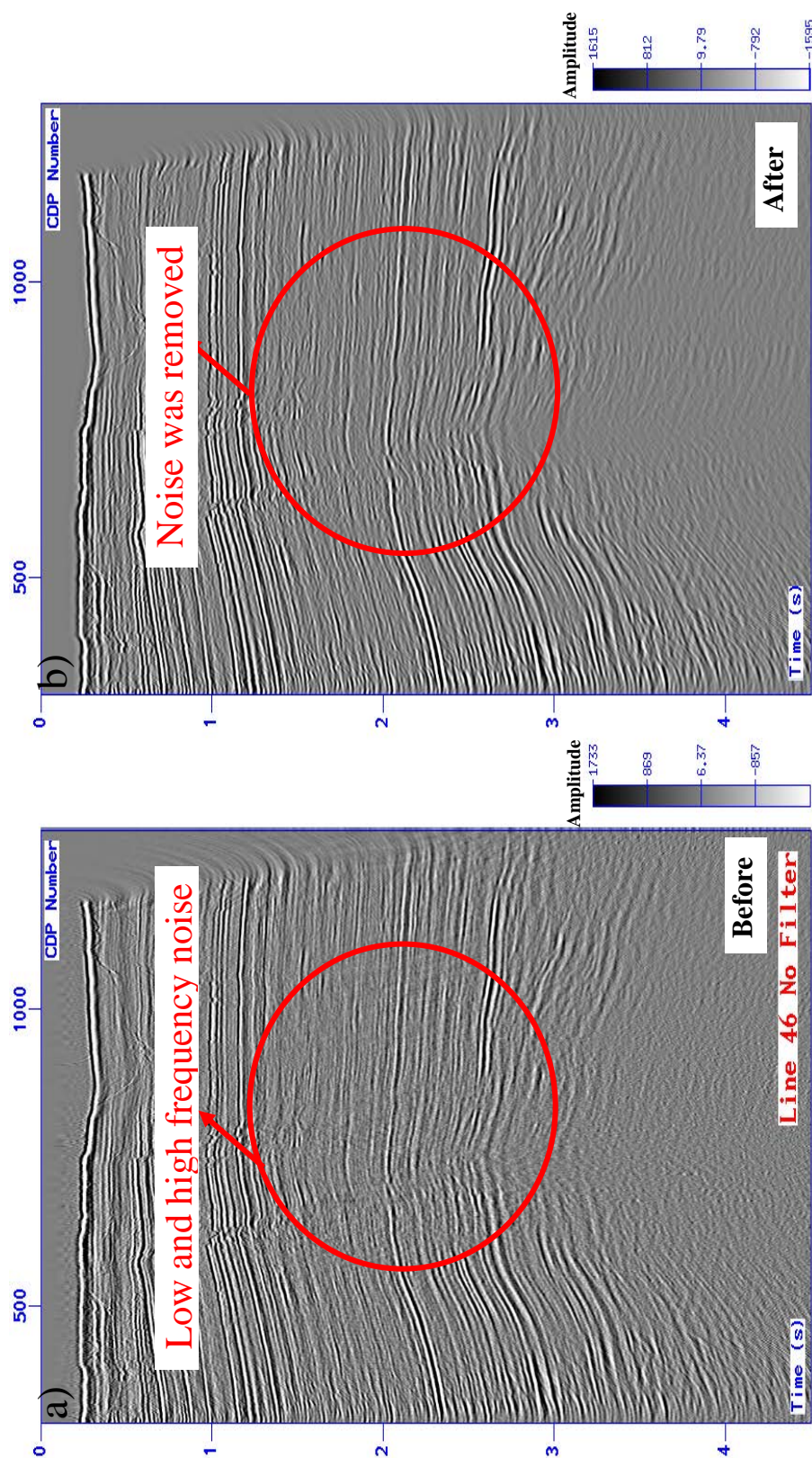


Figure 4.32. Band pass and f-k dip filters for Line 46. A: After migration with lots of vertical scattered noise. B: A band-pass filter and slope filter that were applied to remove the noise. While band-pass filter was removing the noise, slope filter removed angled noise and smoothed the seismic data (Line 46 is 11.7 km long).

4.9. RMS AMPLITUDE AUTOMATIC GAIN CONTROL

The energy of the seismic waves declines with depth. Calculations of the gain recovery for heterogeneous structures have more variables. The gain recovery for earth with a layer is $1/[v^2(t) \cdot t]$ (Newman, 1973). The velocity of the primary reflection which belongs to the single layer, is represented by $v(t)$, and t is the two-way travel time. The gain calculation for a layered earth is:

$$g(t) = [v(t)/v(0)]^2 [t/t(0)] \quad (10)$$

where $v(0)$ is the velocity value at the $t(0)$.

In this study RMS Amplitude Automatic Gain Control was applied. This method is a data dependent method and the software uses the data to scale the amplitudes (Thomas, 1999). Traces of the seismic data were separated to time windows. Amplitudes of each sample in each time window was squared, and the mean of the squared amplitudes of the time window was then calculated. The square root of the mean was computed, and the result was the RMS amplitude of the window. The last step consisted of taking the ratio of a proper RMS amplitude and the real RMS amplitude value. The result is considered as the center gain function of the time window (Yilmaz, 1987). The function for the RMS amplitude automatic gain control is:

$$g(t) = \frac{\text{desired rms}}{\sqrt{\frac{1}{N} \sum_{i=1}^N x_i^2}} \quad (11)$$

where $g(t)$ is the assigned gain function, x_i is the amplitudes of the samples from separated time windows, and N is the number of samples from each time window. Every gain

function value was assigned to the centers of the time windows and interpolated (Yilmaz, 1987).

RMS amplitude AGC (Automatic Gain Control) was applied to all seismic lines to compensate the energy loss that occurred as a result of processing steps, such as NMO correction, PEF, and stacking. The amplitude balancing was applied to the amplitudes for the entire traces (Figure 4.33).

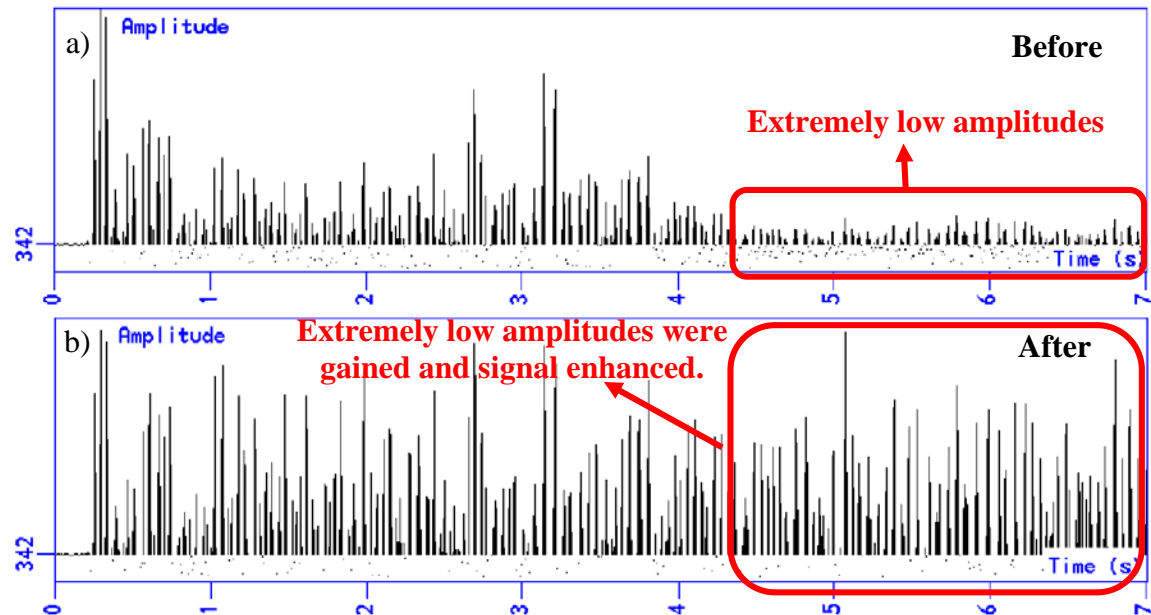


Figure 4.33. Trace 342 from Line 3C post-stack section before and after AGC. A: The amplitudes before AGC. B: The amplitudes after AGC. Extremely low amplitudes were enhanced after gain recovery from 0.2 seconds to 7 seconds.

AGC balances the amplitudes of the seismic lines using an average RMS amplitude value. This is a very fast and effective method to compensate for amplitude loss. Figures 4.34, 4.35, and 4.36 shows Lines 45, 3C, and 46 before and after RMS amplitude AGC. It

can be observed that the amplitudes after AGC are lower than before. It is because that automatic gain control lowers the extremely high amplitudes in a common range and increases the extremely low amplitudes. The reflections on the seismic sections that were blanketed by noise or high amplitude signal were revealed by AGC.

4.10. MUTING

After migration and gain recovery methods, many artifacts occurred at the edges of the seismic sections (Figure 4.37). Muting was applied to edges of all three seismic sections (Figure 4.38). Muting is a cropping process. The cropped parts are not necessary for the interpretation and does not affect the geological formations and structures. For the final step all seismic sections are cut after 4.5 seconds permanently because the resolution was very low after 4.5 s for all sections.

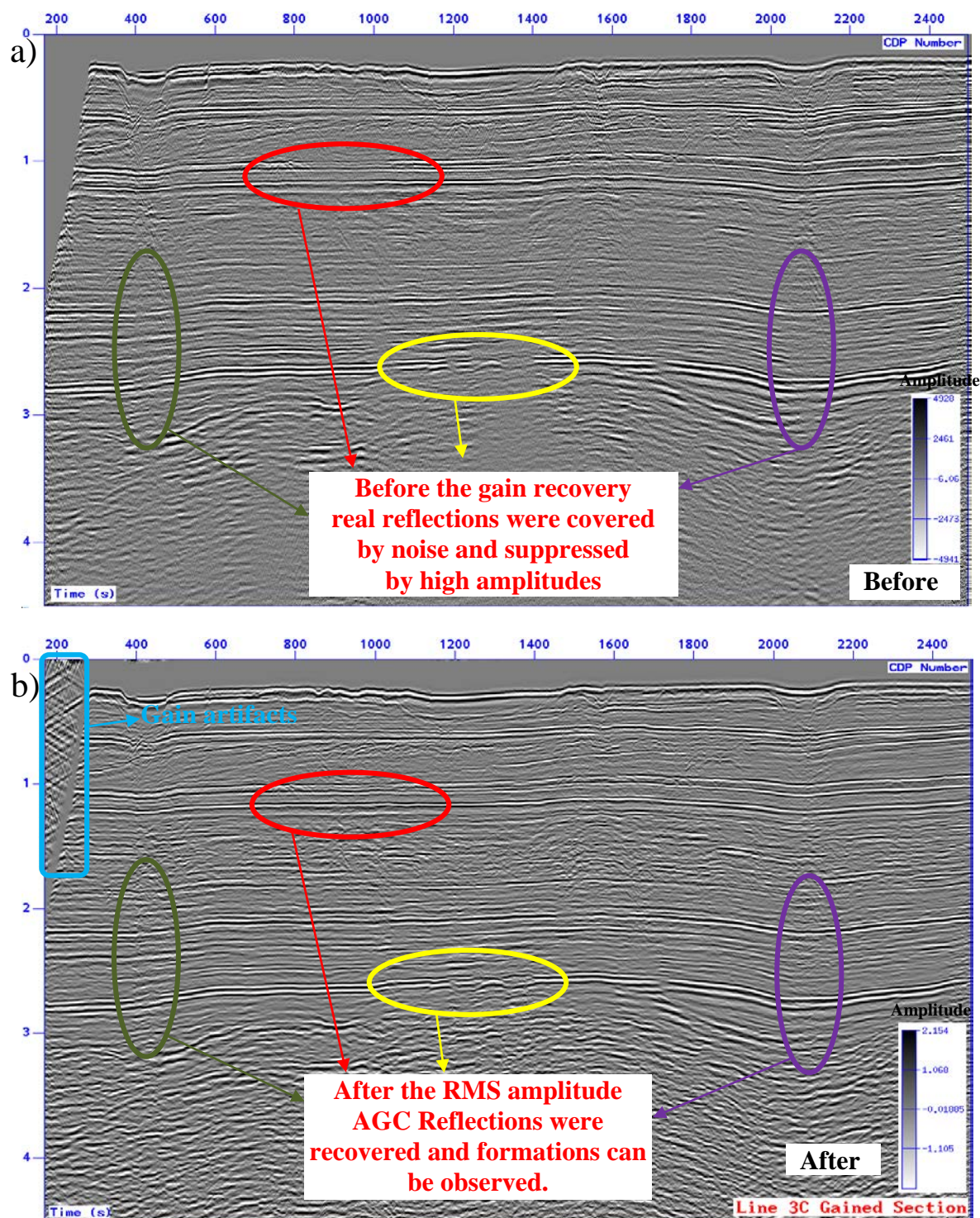


Figure 4.34. RMS amplitude AGC for Line 3C. The marked parts become visible.

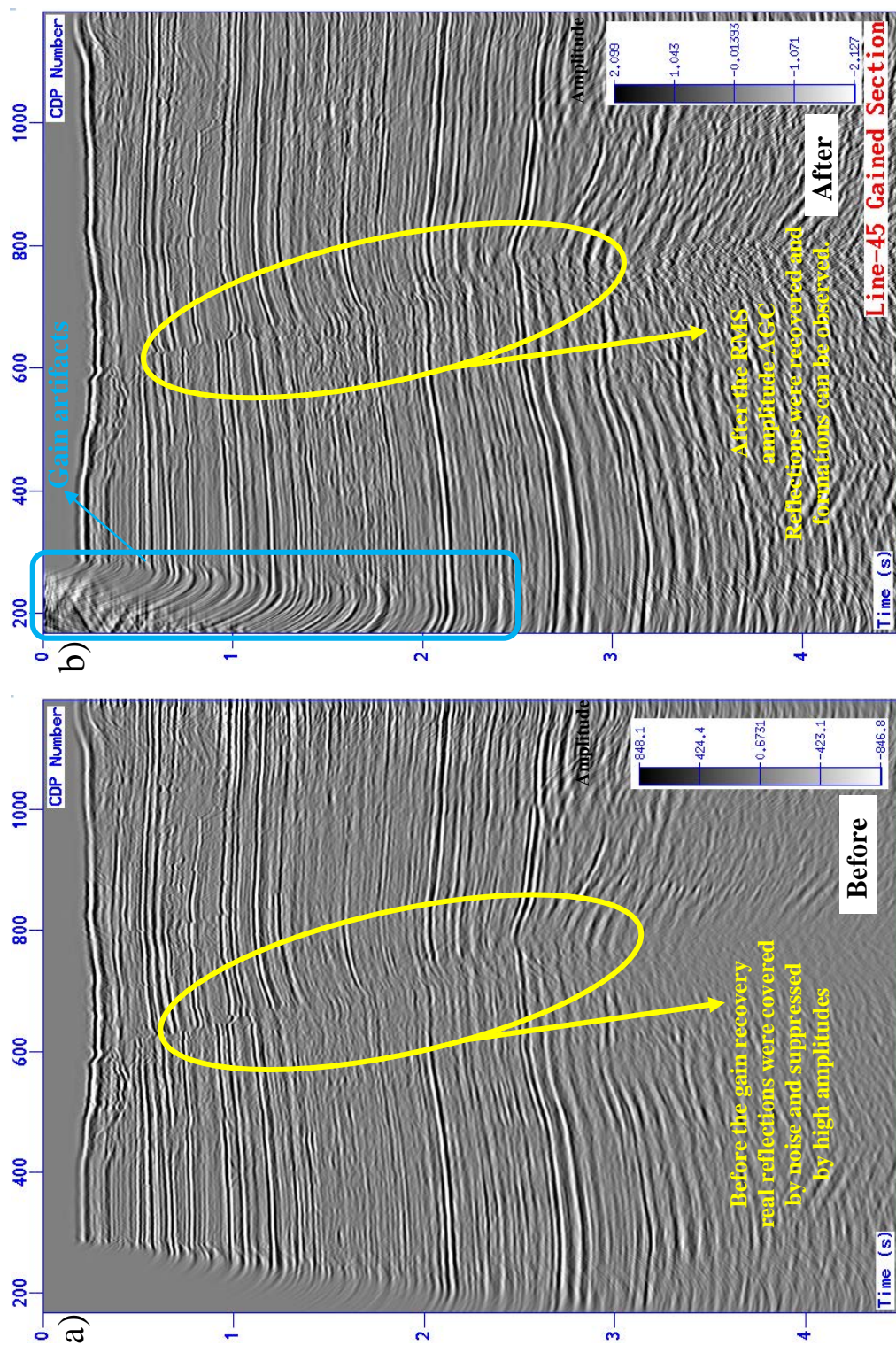


Figure 4.35. RMS amplitude AGC for Line 45. RMS amplitude method recovered the declined and damaged amplitudes.

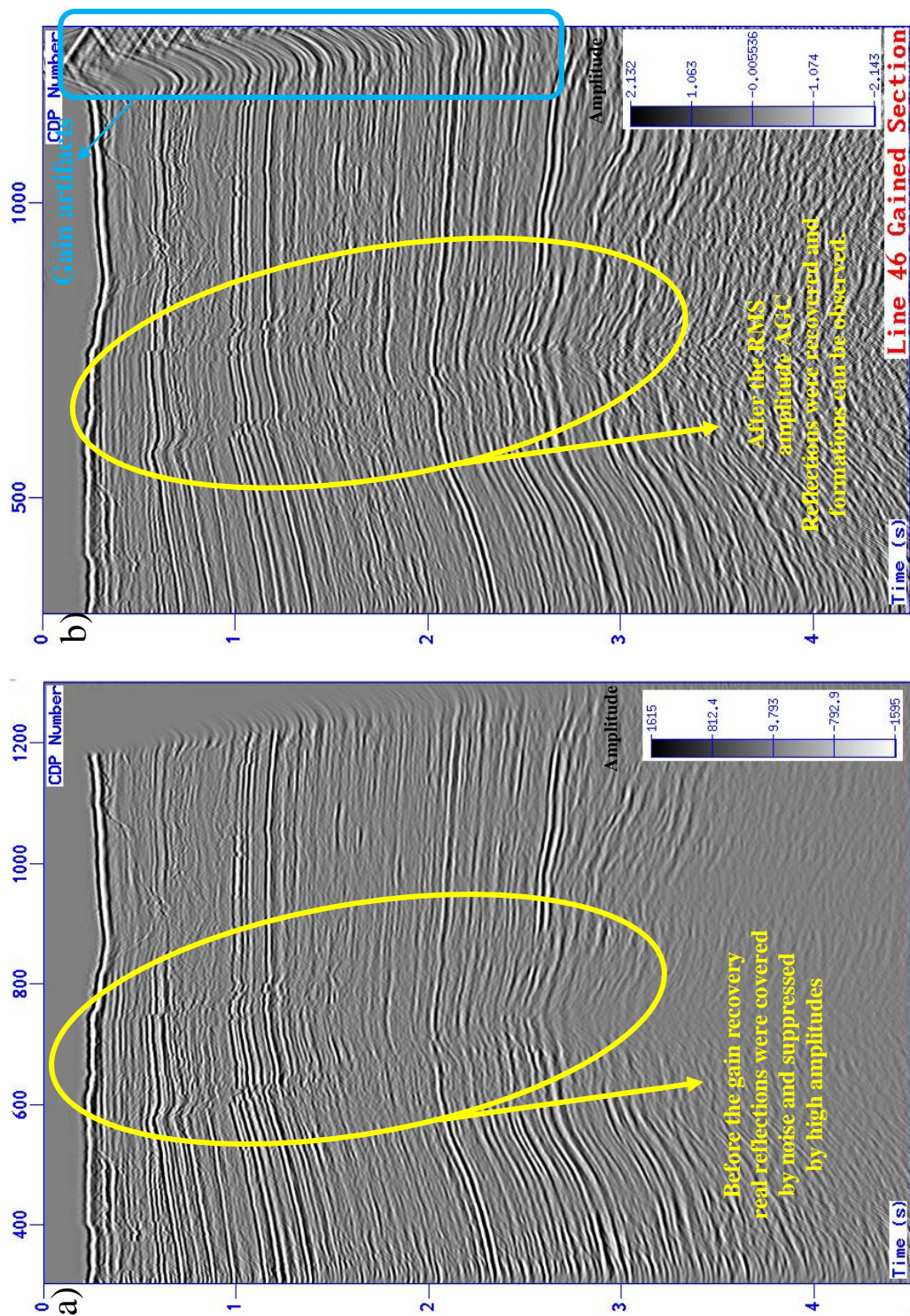


Figure 4.36. RMS amplitude AGC for Line 46. RMS amplitude method recovered the declined and damaged amplitudes.

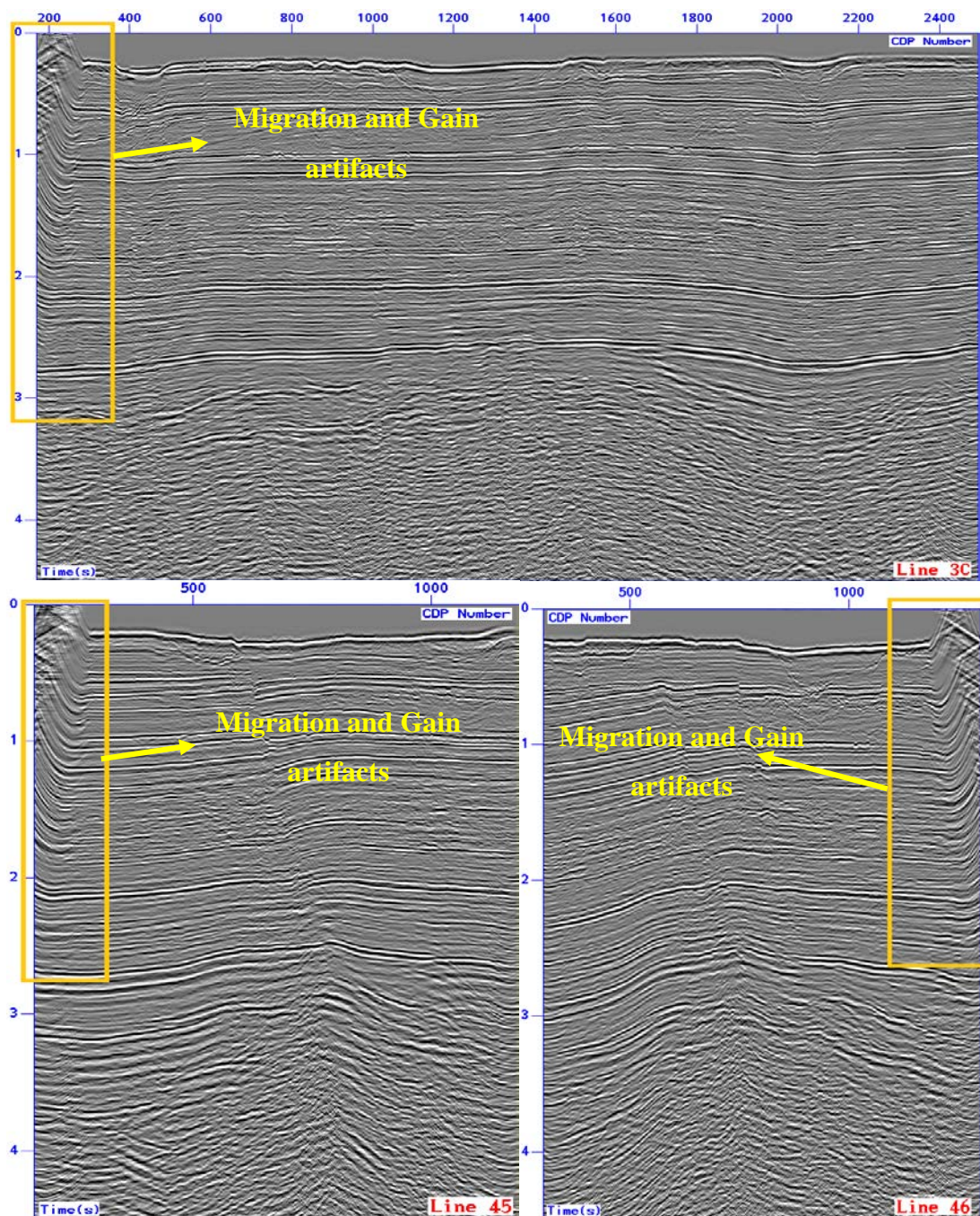


Figure 4.37. Three seismic lines with the processing artifacts. The yellow rectangles highlight the migration and AGC artifacts.

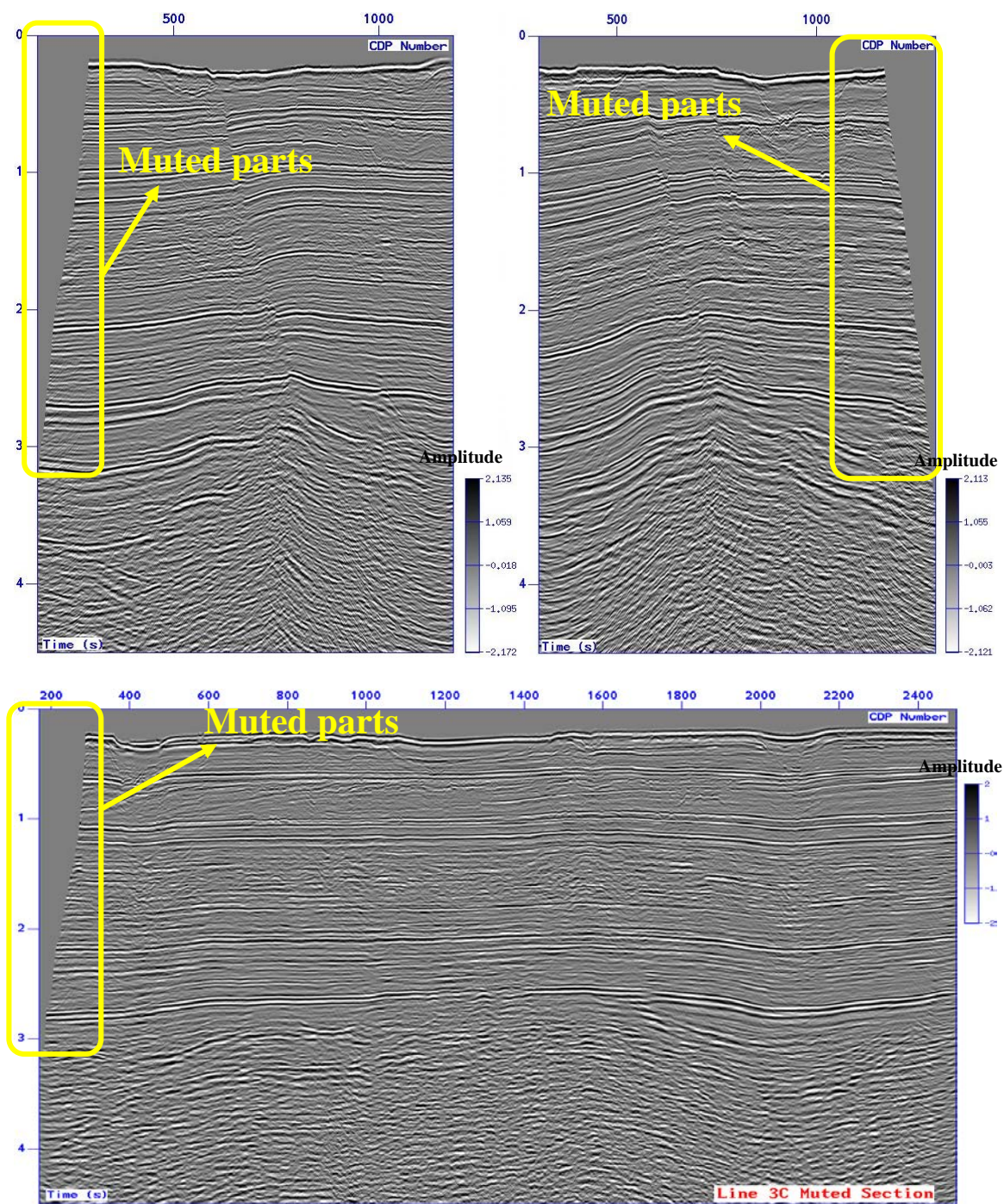


Figure 4.38. Muted Lines 45, 46, and 3C. Mute was applied to all lines to crop the artifacts that occurred as a result of migration.

5. STRUCTURAL INTERPRETATION

5.1. PROCEDURE

The seismic structural interpretation of the Penobscot Parcel-8 area in the Nova Scotia Basin was accomplished using three 2-D reprocessed multichannel post-stack seismic lines and Wells, L-30 and B-41 (Figure 5.1). Kingdom Suite 8.8 and Petrel 2014 were used for the structural interpretation and attribute analysis, respectively.

The three 2-D vertical seismic sections were imported to Kingdom Suite and Petrel. The attribute generation was conducted using Petrel to visualize major and minor faults. A synthetic seismogram was generated to match synthetic trace with the real trace that is extracted from the 2-D seismic lines. Minor and major faults were determined and horizons were interpreted using the synthetic seismogram created from Well L-30.

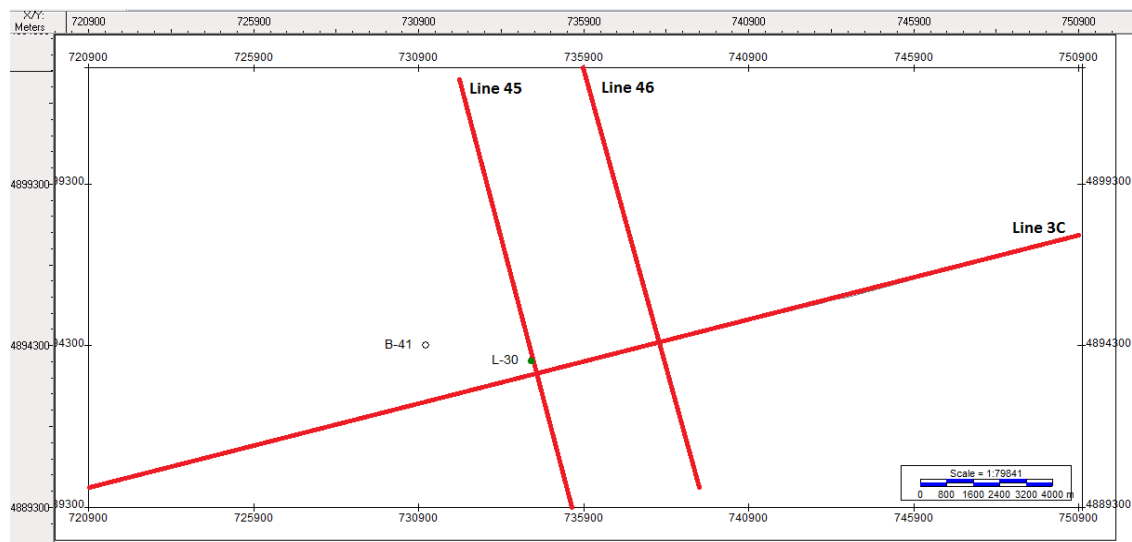


Figure 5.1. The base map of the study area. Three 2-D seismic lines are shown and wells L-30 and B-41 are also represented.

5.2. GENERATION OF THE SYNTHETIC SEISMOGRAM AND MATCHING

The 2-D seismic lines that were used for the interpretation are in the time domain. The well logs and the formation tops are in the depth domain. Because of the domain differences, a match between the units must be done by generating a synthetic seismogram. The time-depth values of horizons that were acquired from the well report were entered in to the Kingdom software. The necessary informations for generating a synthetic seismogram includes a time-depth (T-D) chart, velocity and density logs, a reflection coefficient (RC), and a wavelet.

Well L-30 and its gamma-ray and sonic logs were used. A T-D chart obtained from Well L-30 was used for matching the well and the seismic data. A real seismic trace was extracted from the 2-D seismic lines, and a synthetic seismic trace was generated by convolving with the extracted wavelet and the reflection coefficient values that were taken from the log. Then, the real seismic trace and the synthetic trace were matched (Figure 5.2).

5.3. HORIZON INTERPRETATION

The horizon information that was acquired from the well report was entered in to the Kingdom Suite for horizon picking. Time values of the horizons, determined using the synthetic seismogram, were used to pick horizons. Formations including the Wyandot, Dawson Canyon, Logan Canyon, Upper Missisauga, Base O-Marker, Late Missisauga, Abenaki, and Mid Baccaro were manually picked on Lines 45, 3C, and 46 (Figure 5.3, 5.4, and 5.5). Figure 5.6 represents horizons in 3-D cube.

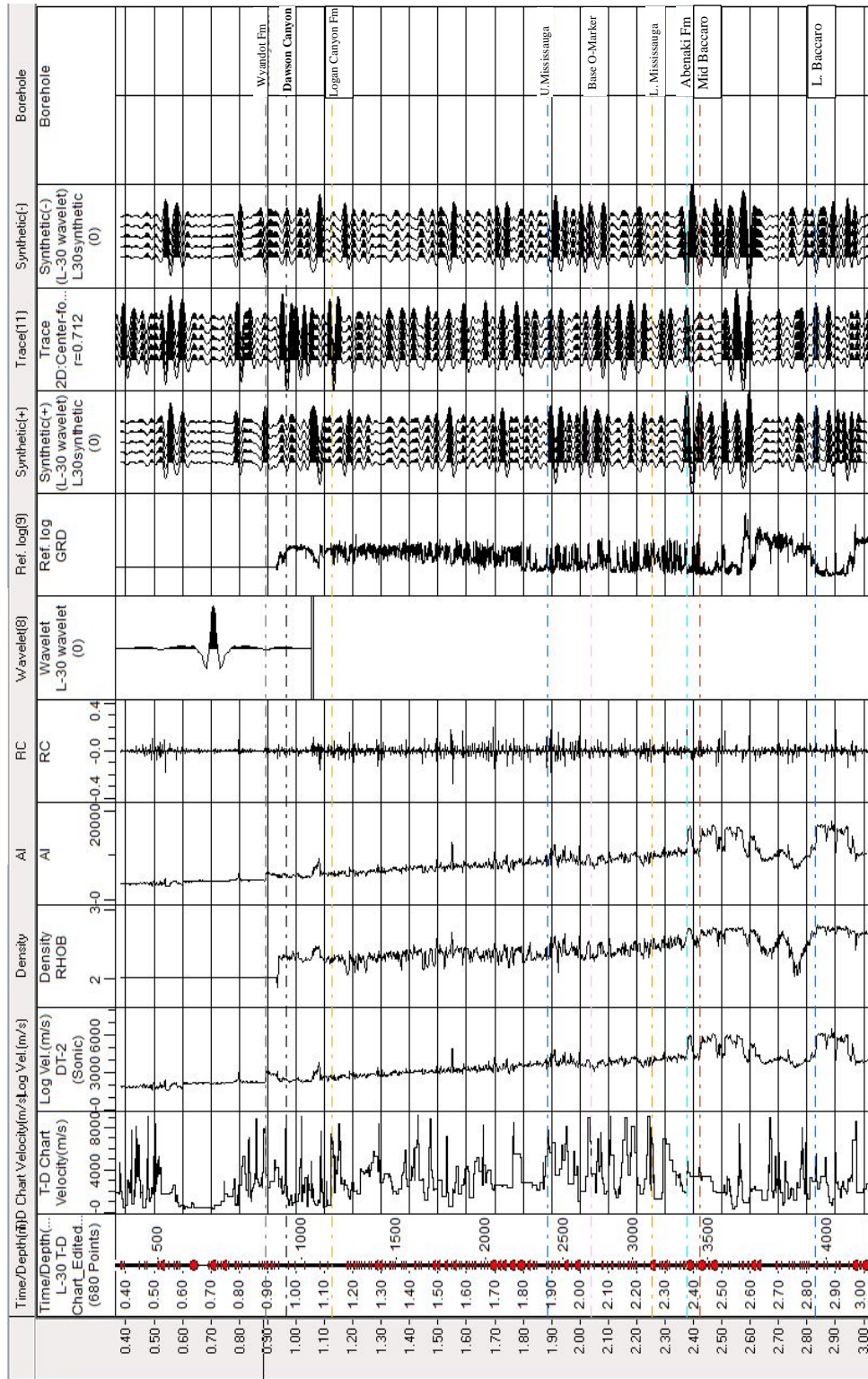


Figure 5.2. The synthetic seismogram and logs from Well L-30. The match between the synthetic trace and the real trace that was extracted from the seismic data is represented.

5.4. FAULT INTERPRETATION

One major fault (Figure 5.3) and four minor faults were interpreted in Line 45, and 5 minor faults and 1 major fault (Figure 5.4) were determined in Line 46. In the Penobscot area, anticlines that were originated from faults act as important traps and major and minor faults act as migration paths for oil accumulation. One major fault (Fault A) (Figures 5.3, 5.4, 5.6) and three of the minor faults were connected in Kingdom Suite and shown in a 3-D cube (Figure 5.6). The accuracy of the connection between minor faults is pretty low because of the lack of the seismic data between Lines 45 and 46.

This major fault structure is a normal fault that lies between the ocean bottom and the Abenaki Formation. However, it is a reverse fault under the Abenaki Formation (Wade & McLean, 1990). This feature can be observed in Line 45 vertical seismic section (Figure 5.3).

According to the information from Well L-30, drilled in 1976 by PetroCanada-Shell, the Missisauga Formation has a reservoir for hydrocarbons. However, Well B-41, drilled in 1977 by Shell-PetroCanada, did not encounter any hydrocarbons. Well L-30 was drilled through a low-relief anticline (Figure 5.3), which was formed by a down-to-basin fault that acted as a hydrocarbon trap.

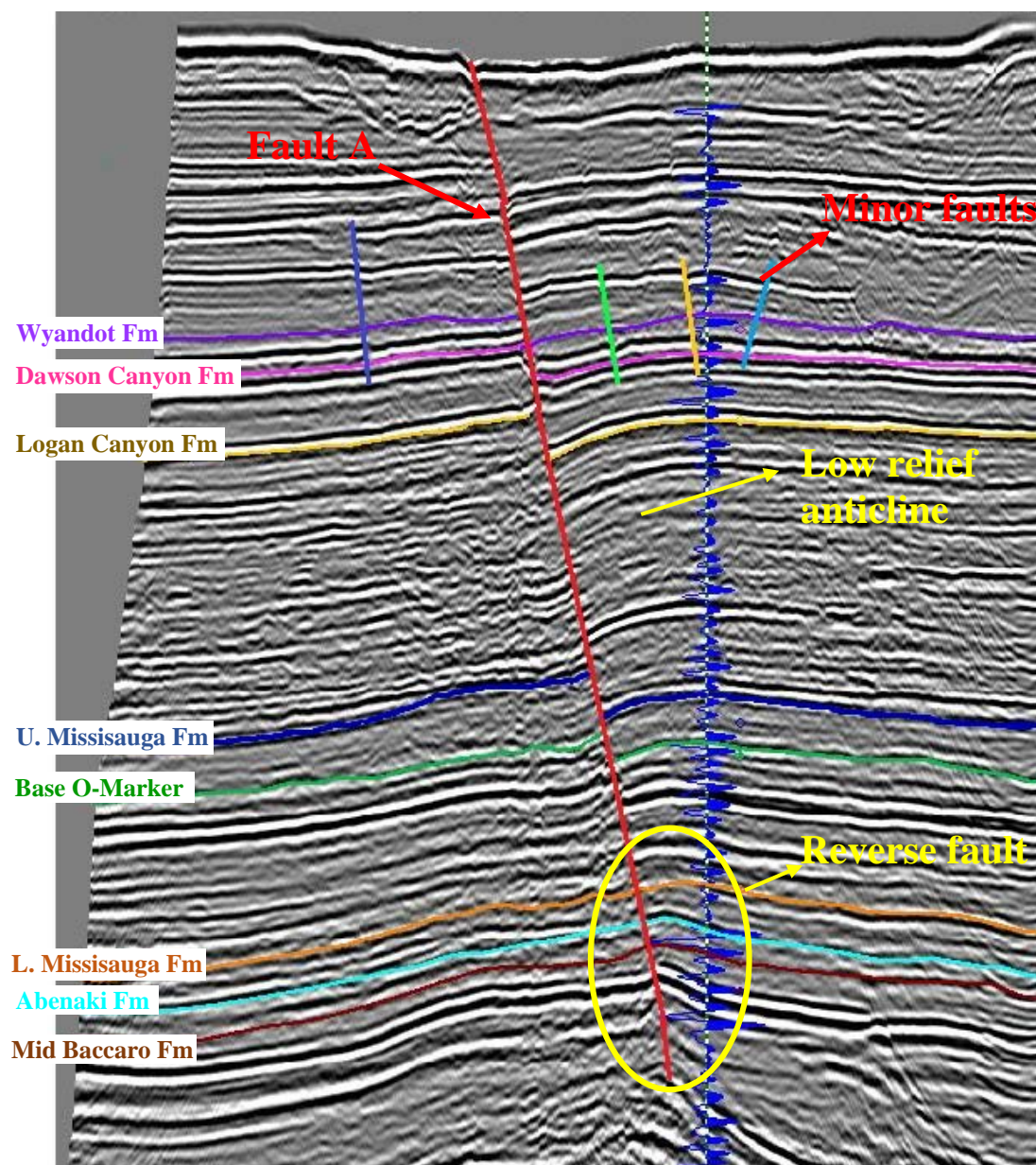


Figure 5.3. Interpreted horizons and faults in Line 45. The Synthetic seismogram from Well L-30 is shown in blue. The red fault is the fault A, which can also be seen in Line 46 as well. From the top to the bottom, the picked horizons are Wyandot Fm, Dawson Canyon Fm, Logan Canyon Fm, Upper Missisauga Fm, Base O-Marker, Late Missisauga Fm, Abenaki Fm, and Mid Baccaro Fm.

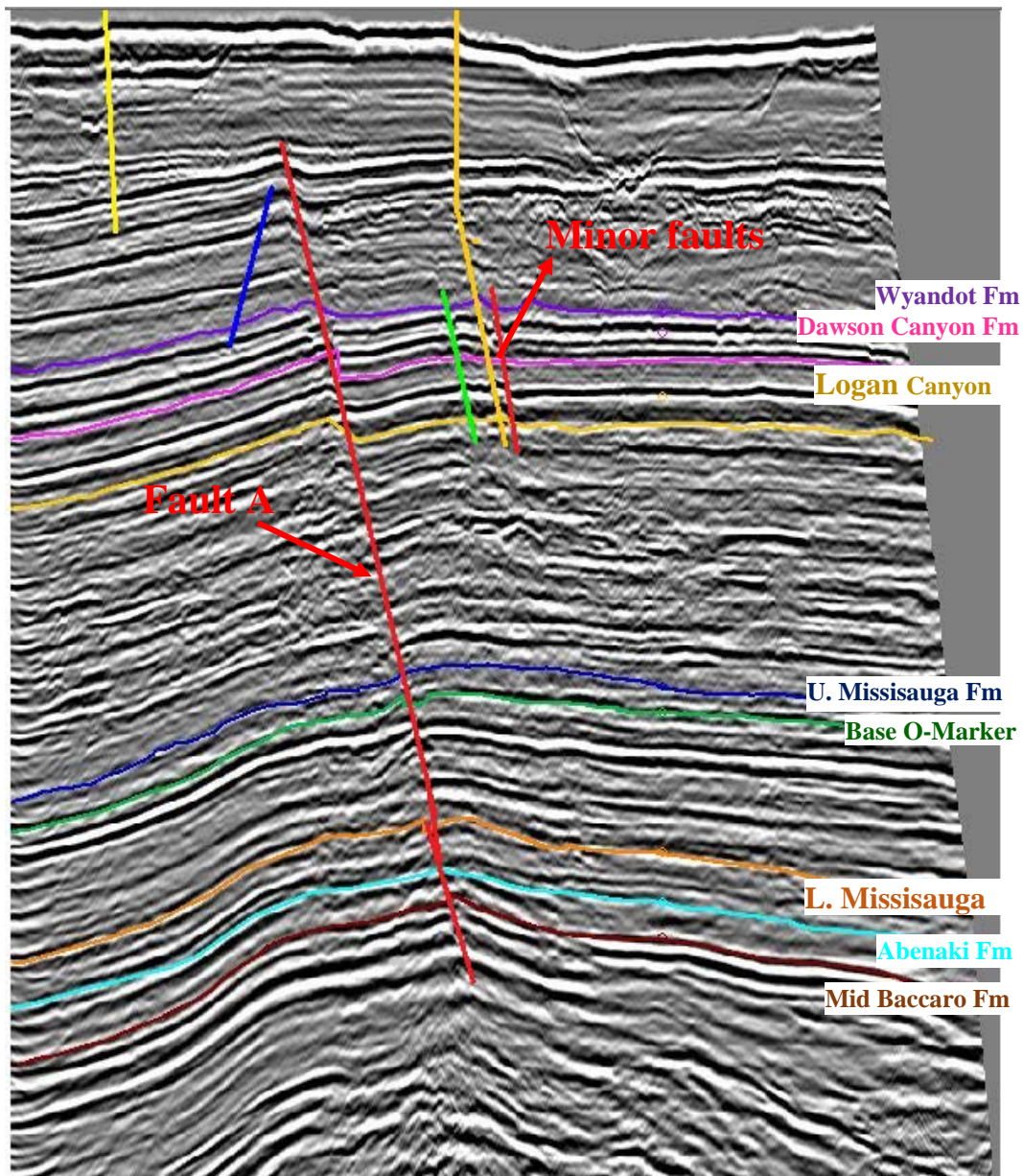


Figure 5.4. Interpreted horizons and faults in Line 46. The fault in red is the major fault and yellow, blue, green, orange and small red lines are minor faults. From top to bottom, the picked horizons are Wyandot Fm, Dawson Canyon Fm, Logan Canyon Fm, Upper Mississauga Fm, Base O-Marker, Late Mississauga Fm, Abenaki Fm, Mid Baccaro Fm, and Late Baccaro.

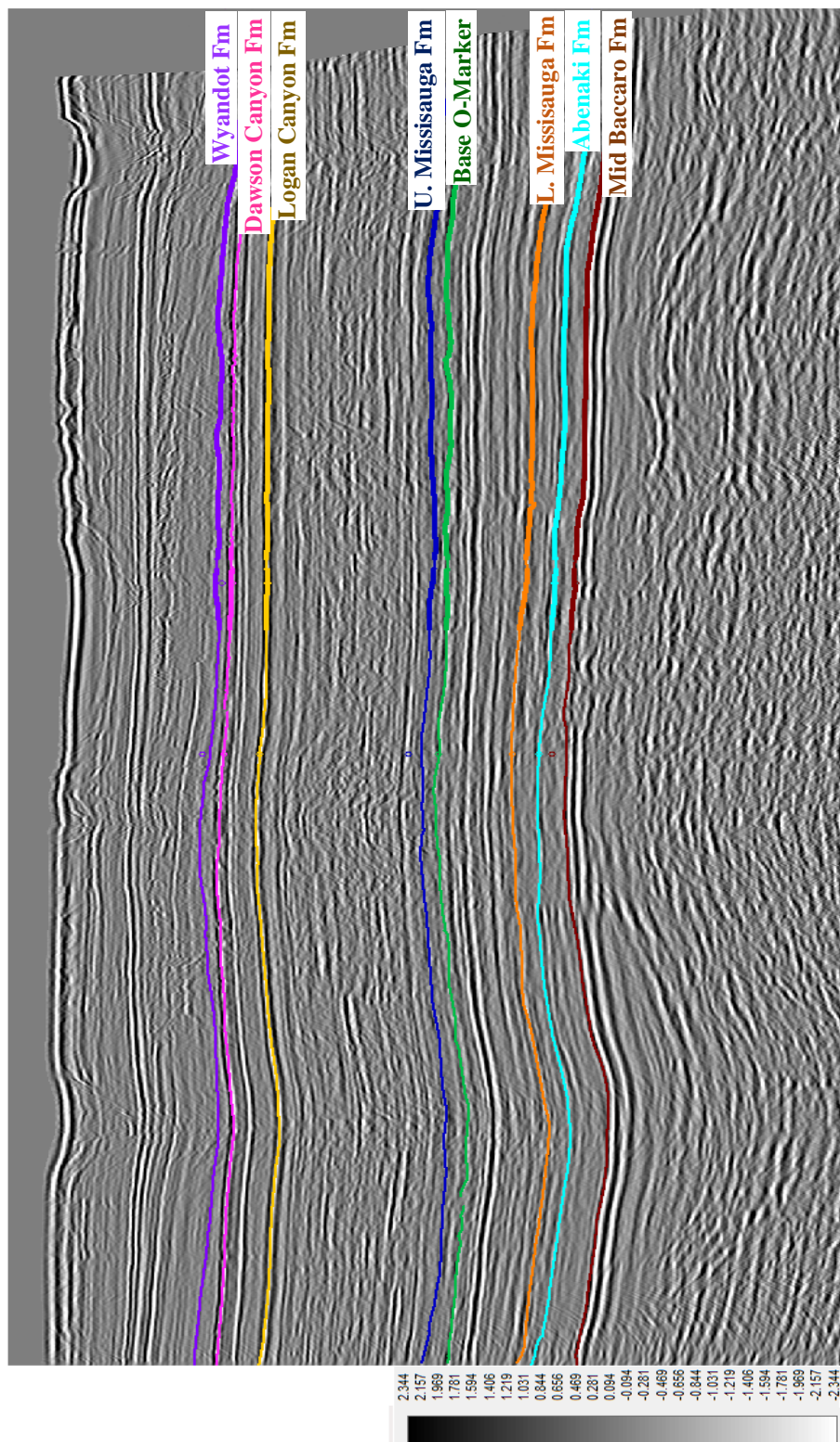


Figure 5.5. Interpreted horizons and faults in Line 3C. No major faults were observed. From top to bottom, the picked horizons are Wyandot Fm, Dawson Canyon Fm, Logan Canyon Fm, Upper Mississauga Fm, Base O-Marker, Late Mississauga Fm, Abenaki Fm, and Mid Baccaro Fm.

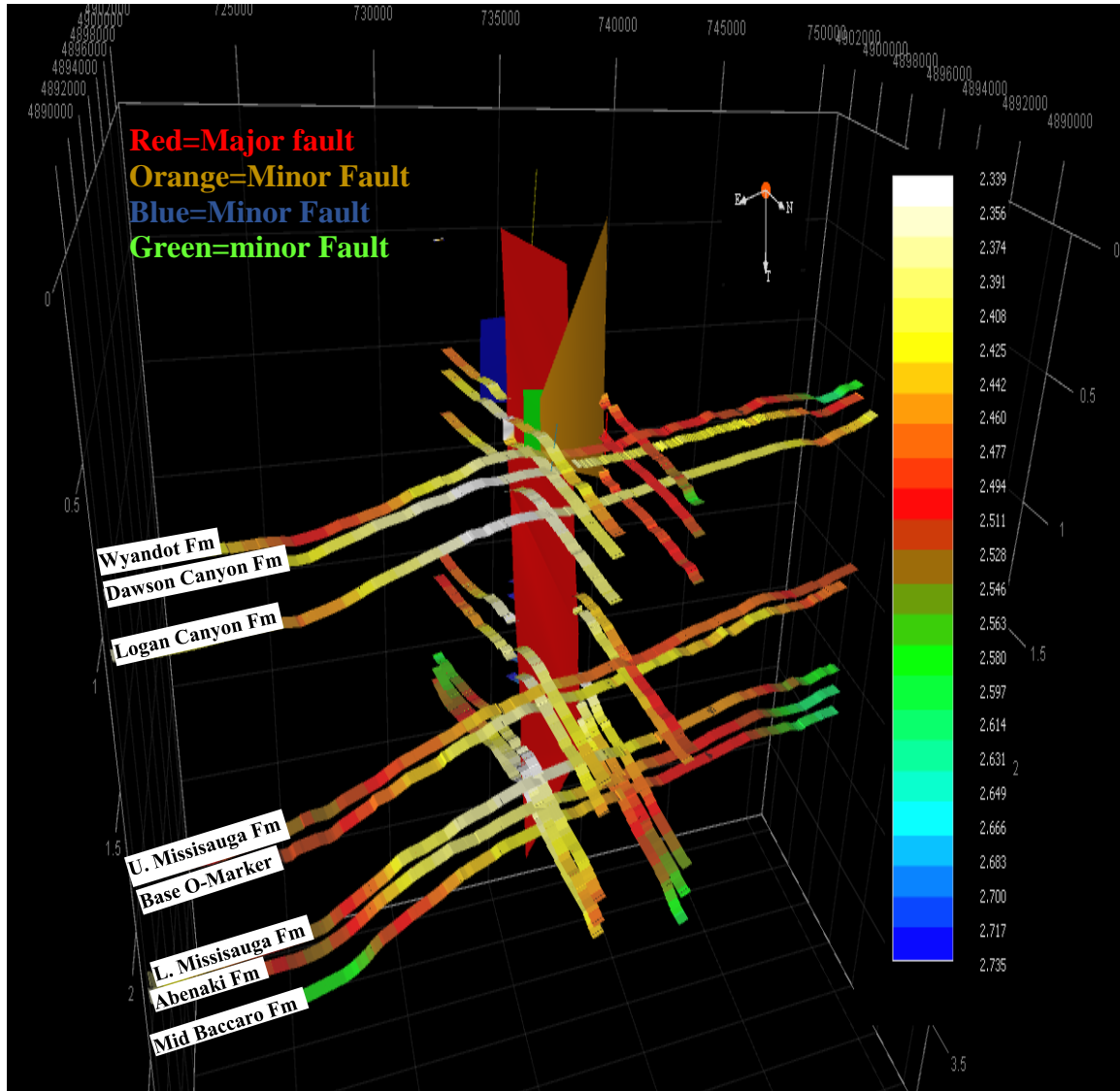


Figure 5.6. Interpreted horizons and faults from Lines 45,46, and 3C. Eight horizons were interpreted manually. From top to bottom, the picked horizons are Wyandot Fm, Dawson Canyon Fm, Logan Canyon Fm, Upper Missisauga Fm, Base O-Marker, Late Missisauga Fm, Abenaki Fm, and Mid Baccaro Fm.

5.5 ATTRIBUTE ANALYSIS

Attributes are calculated from the seismic data itself such as mean amplitude, phase, and other values gathered from the data (Sampson, 2012). Attributes help to observe various features of the data, such as faults, amplitude contrasts, bed thickness, formation

continuity, fluid content (Taner et al., 1979; Taner, 2001). Various attributes are used to reveal specific features of the seismic data. In this study, instantaneous phase and variance (edge method) were used to reveal faults and layer continuity.

5.5.1. Variance (Edge Method). Variance computes the variability from trace to trace. Similar traces show low variability. Discontinuities have high acoustic impedance that can be seen as high variability on variance. Faults and structures that may destroy the continuous layer might be observed by variance attribute (Randen et al., 2001). Petrel's variance (edge method) attribute was used to better observe the faults in Lines 45 and 46 (Figure 5.7 and 5.8). While the major fault was observed successfully, minor faults cannot be detected.

5.5.2. Instantaneous Phase. Instantaneous attributes are computed from complex traces (Taner, 2001) and can be calculated as instantaneous amplitude, phase, frequency, bandwidth, trace envelope, etc.

Phase attributes can also be used to observe physical structures in the seismic section. Instantaneous phase is used to reveal formation continuity, unconformities, and faults (Sacrey&Roden, 2014). Figures 5.9, 5.10, and 5.11 show Lines 3C, 45, and 46 after the generation of the instantaneous phase attribute.

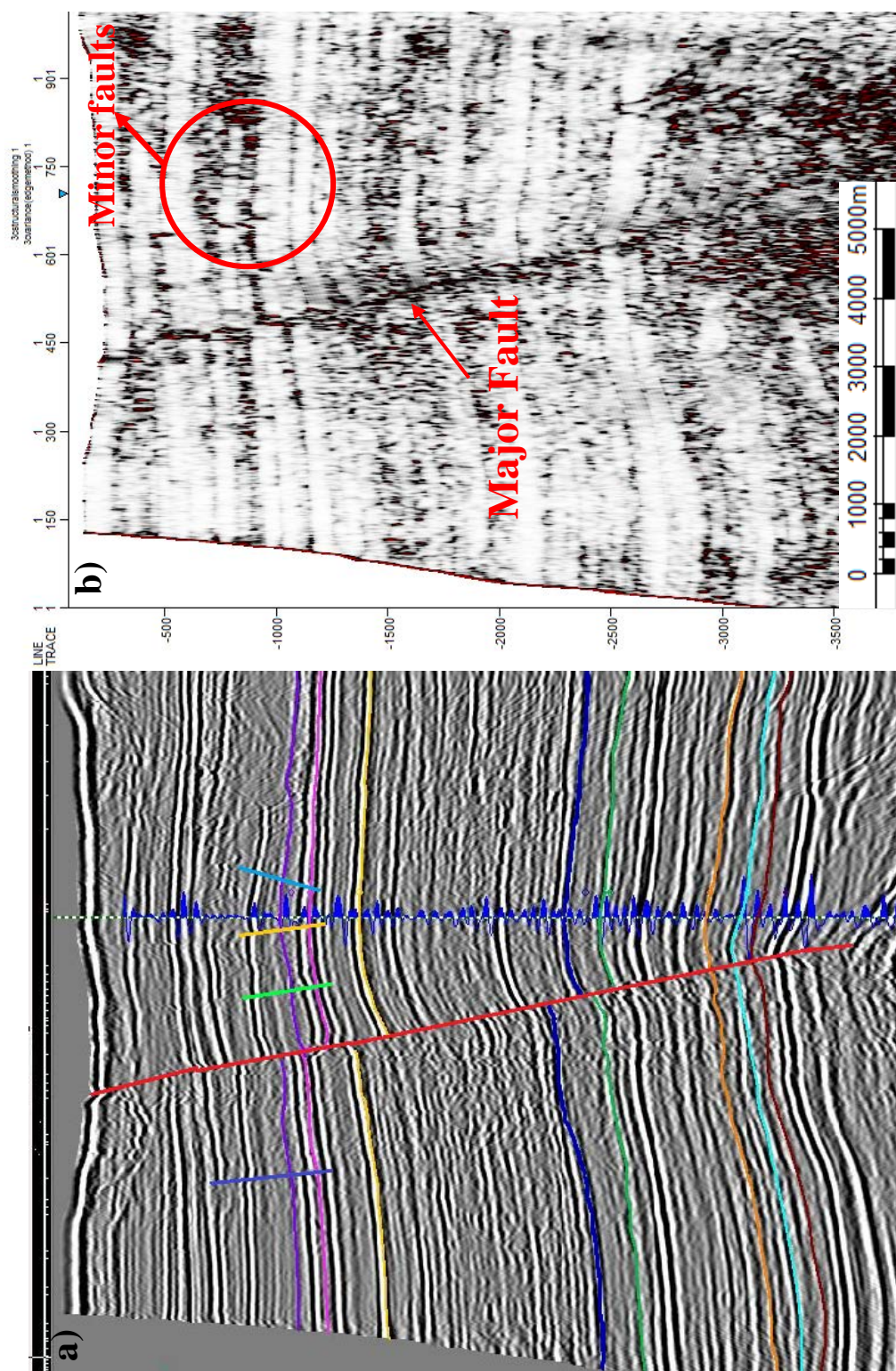


Figure 5.7. The variance (edge method) attribute for Line 45. A: The fault interpretation on Line 45. B: The major fault on Line 45 after the attribute. The variance attribute represented the deeper parts of the major fault better than the seismic section.

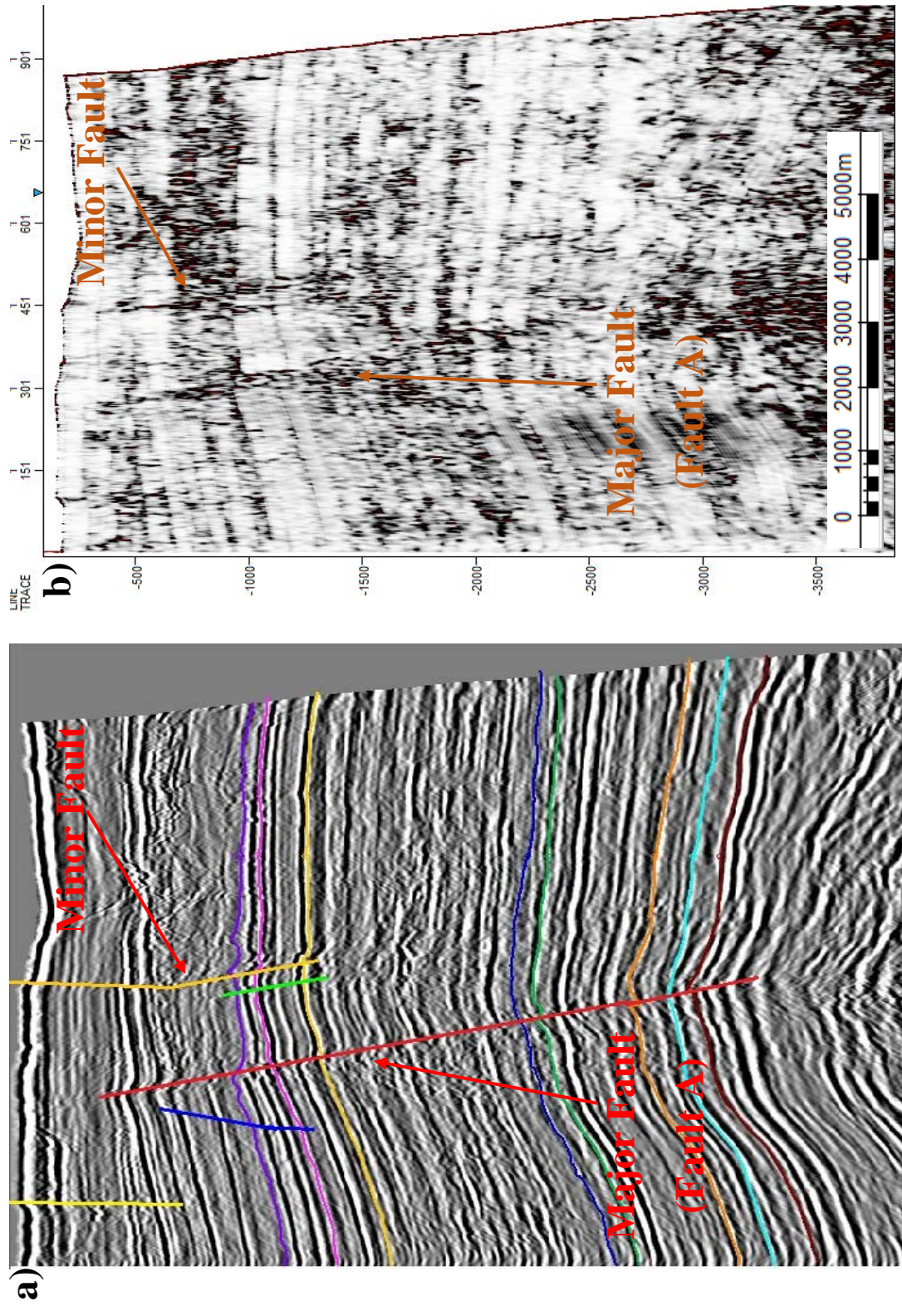


Figure 5.8. The variance (edge method) attribute of Line 46. A: Line 46 before the attribute. B: Line 46 after the attribute.

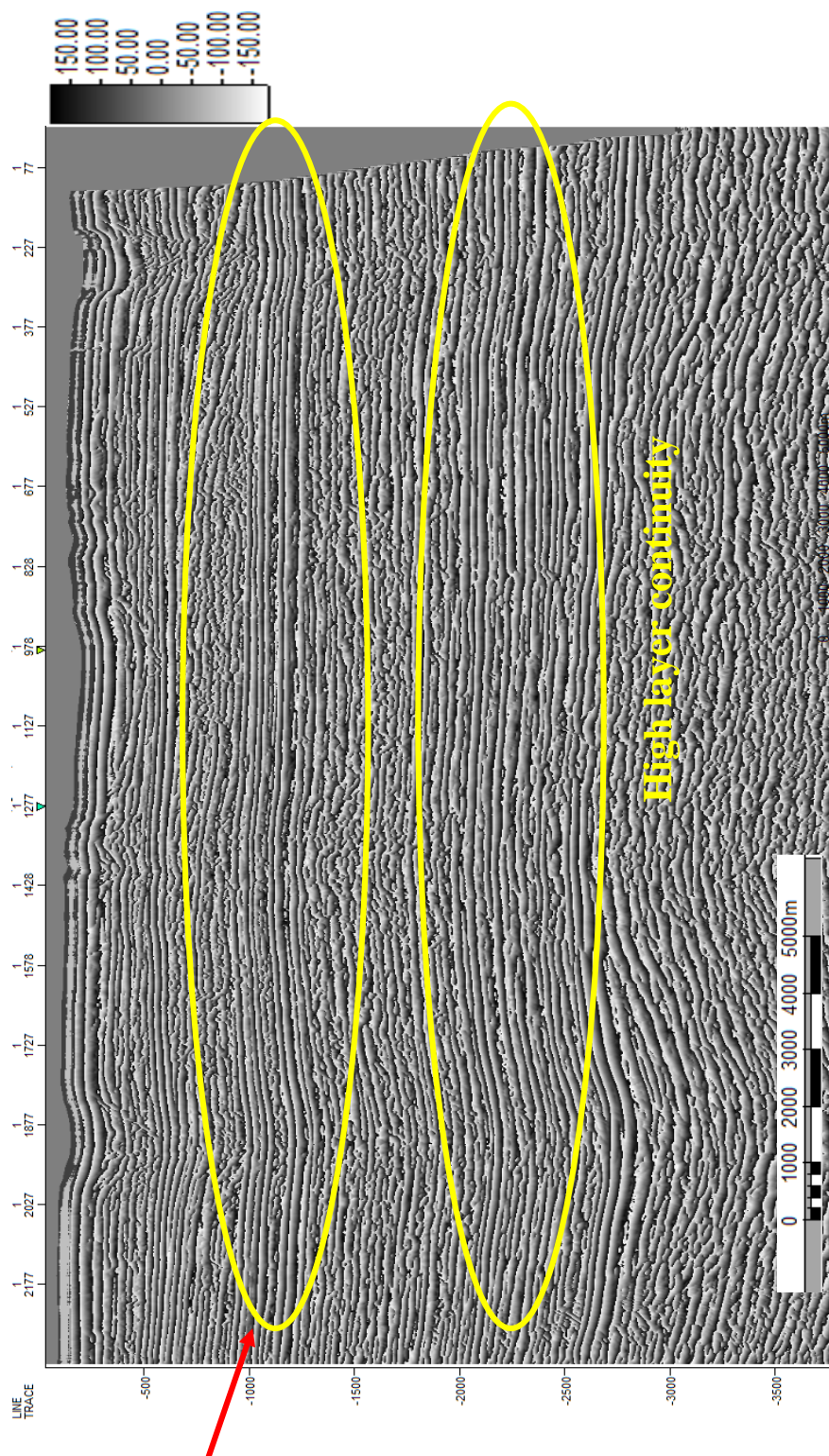


Figure 5.9. Instantaneous phase attribute of Line 3C. The attribute shows the layer continuity. The line does not have any major faults. As a result, layer continuity is not disrupted by major fractures.

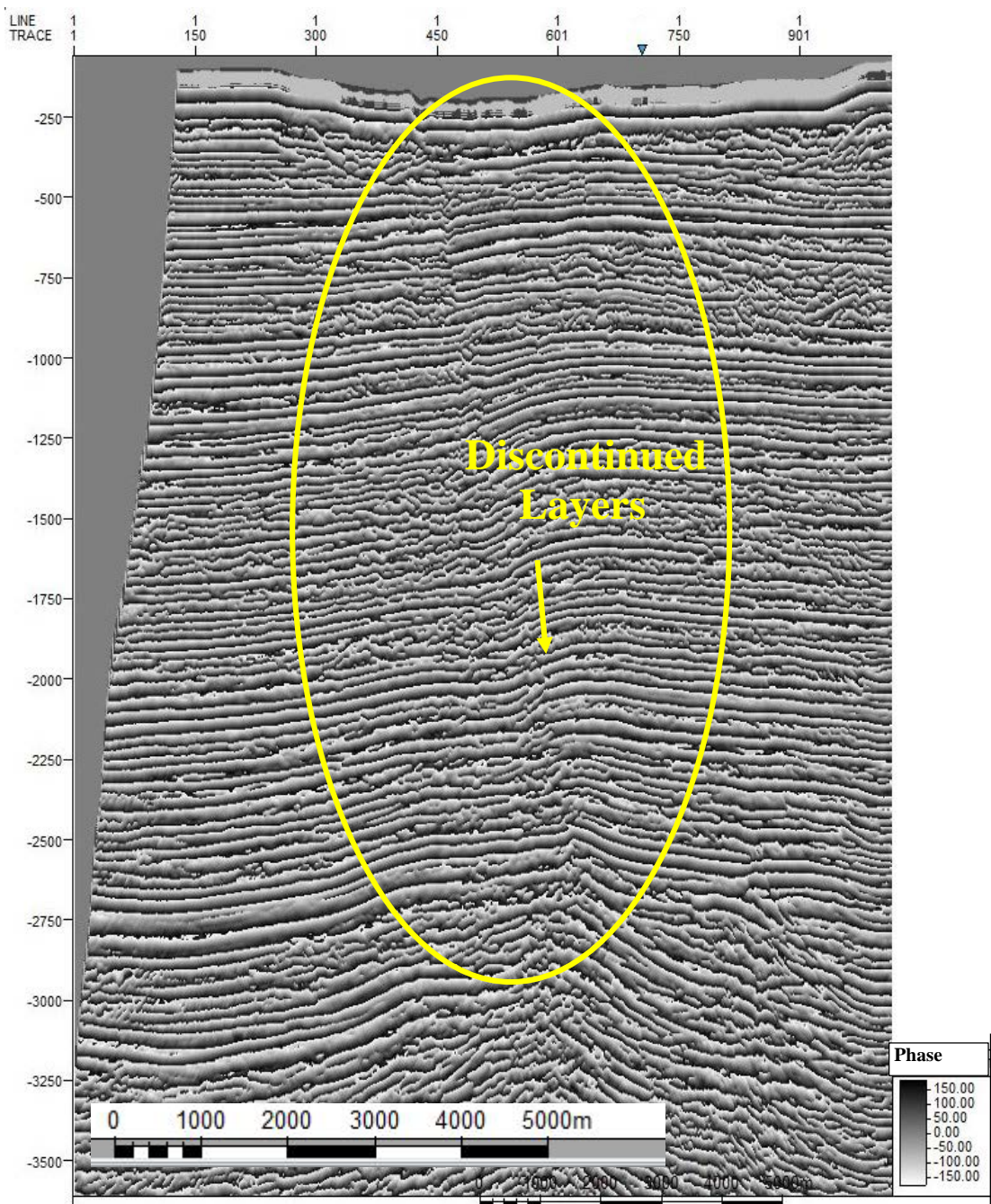


Figure 5.10. Instantaneous phase attribute of Line 45. The layer continuity is disrupted by the major and minor faults.

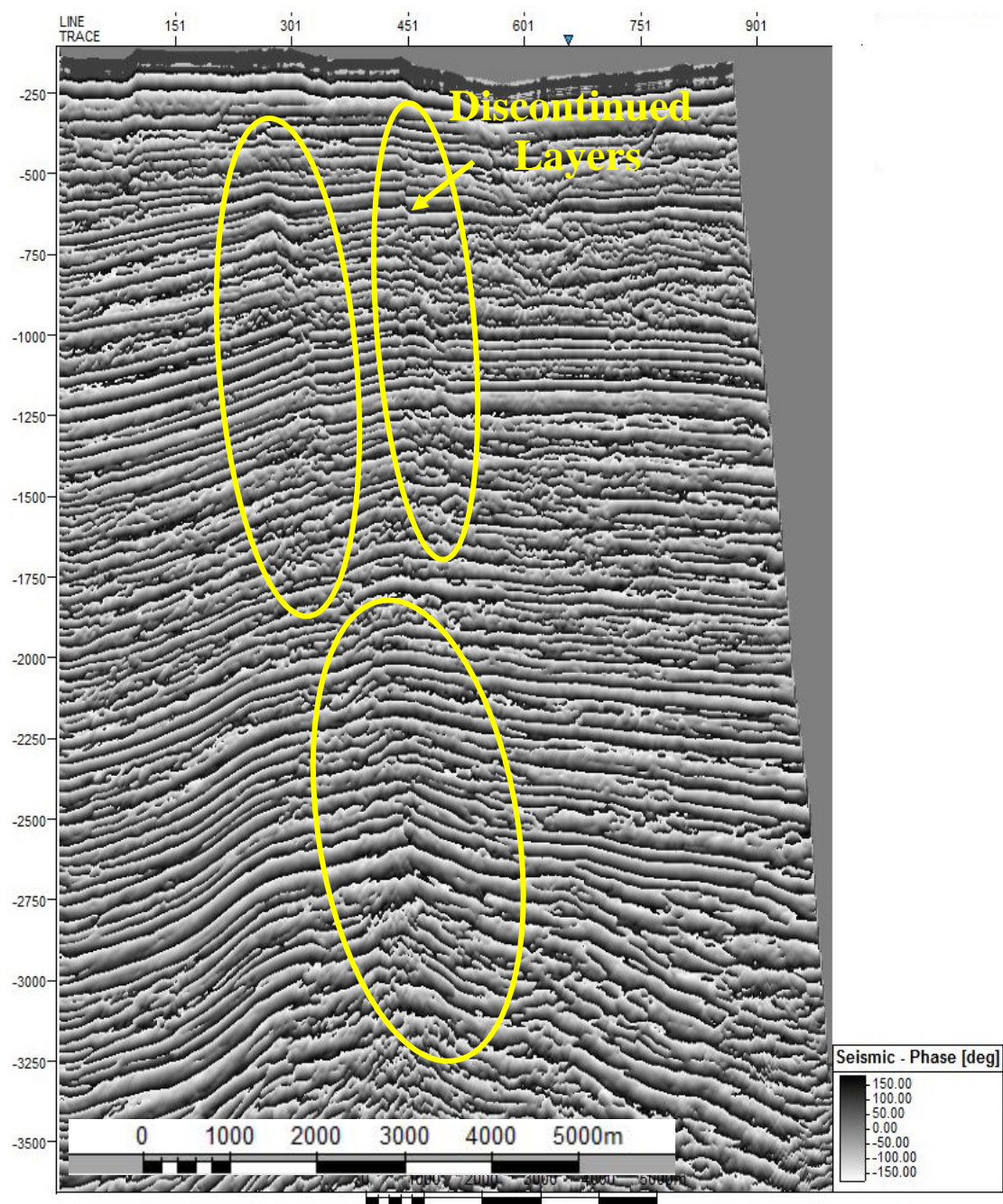


Figure 5.11. Instantaneous phase attribute of Line 46. The layer continuity is disrupted by the major and minor faults.

6. CONCLUSIONS AND RECOMMENDATIONS

Three 2-D multichannel seismic reflection lines were reprocessed using the Seismic Unix software. The main purpose was to increase the signal-to-noise ratio by generating the correct processing flow for each seismic line to prepare the seismic lines for structural interpretation. The study includes the pre-stack and post-stack processing of three seismic lines. Working with 2-D seismic lines helped to understand how to handle the problems that were related to the noise and artifacts of the processing methods. All processing methods aimed to increase the resolution by suppressing multiples, removing noise and artifacts of the processing methods.

The first application for all three seismic lines was the Butterworth minimum phase filter. The Butterworth filter were applied to the pre-stack data because the data was assumed to be minimum phase. Minimum phase filter solved the low amplitude problem of the ocean bottom reflections and enhanced the reflections.

Spiking deconvolution and the prediction error filter were applied to Lines 45 and 46. Pre-stack application of spiking deconvolution and PEF together recovered the low amplitudes between 1 and 2 seconds on velocity semblances and increased the accuracy of velocity picking, which is crucial for NMO correction.

The Stolt migration collapsed diffractions at shallow parts with a constant velocity successfully. However, it failed to collapse diffractions at deep parts properly with the same velocity. When a different velocity used for deeper formations, Stolt created overmigrated sections at the shallow part. As a result, Stolt failed to migrate the shallow and deep formations around a long dipping structure at the same time.

The Gazdag migration removed all diffractions that were occurred in Lines 45 and 46 successfully. Two different velocities were used for each line from 0 to 2 seconds and 2 to 4 seconds. Gazdag migration gave the desired result and removed diffractions in the shallow part and deeper part while simultaneously protecting the resolution of the minor faults at 0.8 seconds. As a result, Gazdag migration were used for structural interpretation because the migration was successful for shallow and the deep parts at the same time, unlike the Stolt migration.

A synthetic seismogram was generated to provide accuracy in picking horizons and the correlation coefficient, r , that indicates the similarity between the generated trace and the real trace was obtained as 0.712, which was a good match. Eight horizons were picked to visualize the subsurface of the study area using the synthetic seismogram and showed in a 3-D cube. The horizons that were picked are Wyandot Fm, Dawson Fm, Logan Canyon Fm, Upper Mississauga Fm, Base O-Marker Fm, Late Mississauga Fm, Abenaki Fm, Mid Baccaro Fm.

Fault picking was conducted in Kingdom Suite and one major down-to-basin fault (fault A) and minor faults were interpreted in both Lines 45 and 46. The major fault has a normal displacement from sea bottom to Abenaki Formation and it becomes a reverse fault after then. This specific situation was interpreted in vertical section of Line 45. In addition, a low relief anticline that is attached to the down-to-basin fault, which hosts hydrocarbons, was visualized in vertical section of Line 45.

Attribute generation was conducted. Variance and instantaneous phase attributes were generated. Variance (edge method) attribute provided convenience to observe the major fault on Lines 45 and 46. The second attribute, instantaneous phase, showed that the

layer continuity of Line 3C was not disrupted by any faults. It was also observed that the highly disturbed structures of Lines 45 and 46 caused a low layer continuity.

Although, the Seismic Unix open source software has many limitations, each processing step provided the necessary improvements. Because Seismic Unix is an environment that works with codes, it gives the opportunity to use many different combinations of the steps with different parameters. However, a more advanced software can provide processing techniques with a developed environment.

Interpretation of 2-D seismic lines were conducted using Kingdom Suite and Petrel software. The lack of data between three seismic lines did not let for a sufficient structural interpretation, a more comprehensive study with a significant number of seismic profiles can be conducted to provide more accurate results.

BIBLIOGRAPHY

- Albertz, M., C. Beaumont, J. Shimeld, S.J. Ings, and Gradmann S., 2010, An investigation of salt tectonics structural styles in the Scotian Basin, offshore Atlantic Canada: 1. Comparison of observations with geometrically simple numerical models, *Tectonics*, v. 29, no. 4.
- Antsey, N.A., 1977, *Seismic Interpretation: The Physical Aspects*, Springer Science Business Media Dordrecht, ISBN 978-94-015-3924-1, 1-641.
- Balkwill, H.R. and Legall, F.D., 1989, Whale Basin, Offshore Newfoundland: Extension and Salt Diapirism. In: A. J. Tankard and J. R. Balkwill (Eds.), "Extensional Tectonics and Stratigraphy of the North Atlantic Margins". *American Association of Petroleum Geologists Memoir* 46, p. 233-246.
- Berryman, J.G., 1979, Long-wave elastic anisotropy in transversely isotropic media, *Geophysics* 44 (5), 896-917.
- Bormann, P., 2013, Seismic Signals and Noise, In: Bormann, P. (Ed.), *New Manual of Seismological Observatory Practice 2 (NMSOP2) Chapter 4*, Potsdam: Deutsches GeoForschungsZentrum GFZ, 1-34.
- Burnett, W. A., R.J. Ferguson, 2008, Reversible Stolt Migration, *CREWES Research Report*, v.20.
- Catuneanu, O., 2006, *Principles of Sequence Stratigraphy*. Elsevier, Canada Nova Scotia Offshore Petroleum Board, Amsterdam. Retrieved May 12, 2015, From: <http://www.cnsopb.ns.ca/geoscience/geoscience-overview/exploration-history>.
- Chun, J.H. and C. Jacewitz, 1981, Fundamentals of frequency-domain migration: *Geophysics*, 46, 717-732.
- CNSOPB (Canada–Nova Scotia Offshore Petroleum Board) (2008), Regional Geology Overview, Retrieved from CNSOPB Web-site: http://www.callforbids.cnsopb.ns.ca/2007/01/regional_geology.html.
- Cochran, M.D., 1973, Seismic signal detection using sign bits, *Geophysics* 38, 1042-1052.
- Colletta, B, F. Monnier, G. Rabary, S. Doublet, P. Letouzey, BeicipFranlab, 2011, Offshore Nova Scotia Play Fairway Analysis: 2D Basin Modeling Results. Offshore Technology Conference, Houston Texas, USA.
- Crosson, R., 2014, ESS522 Data Analysis Course Notes, School of Oceanography University of Washington.

- Cummings, D.I., and R.W.C. Arnott, 2005, Growth-faulted shelf-margin deltas: a new (but old) play type, offshore Nova Scotia, *Bulletin of Canadian Petroleum Geology*, v. 53, p. 211-236.
- Dainty, A.M., C.E. Keen, M.J., and J.E. Blanchard, Review of geophysical evidence on crust and upper-mantle structure on the eastern seaboard of Canada; in the Earth beneath the continents, ed. J.S. Steinhardt and T.J. Smith; *American Geophysical Union*, p. 349-369.
- Etikha, 2012, Postrift deformation of the scotian basin, offshore Nova Scotia and Newfoundland, Canada: insights from 2D and 3D seismic-reflection data, *Master Thesis*, Graduate School-New Brunswick Rutgers, The State University of New Jersey.
- Gazdag, J., 1978, Wave equation migration with the phase-shift method: *Geophysics*, 43, 1342-1351.
- Gazdag, J., and P. Sguazzero, 1984, Migration of seismic data by phase shift plus interpolation: *Geophysics*, 49, 124-131.
- Goodman, D.W., 1985, Final Report of Marine Seismic Survey for Nova Scotia Resources on Scotia Shelf-Sable Island, *Western Geophysical Company of Canada*.
- GSC (Geological Survey of Canada), 1991, East Coast Basin Atlas Series: Scotian Shelf. Atlantic Geoscience Centre, *Geological Survey of Canada*, Ottawa, p. 152.
- Hansen, D. Møller, J.W. Shimeld, M.A. Williamson, H. Lykke-Andersen, 2004, Development of a major polygonal fault system in Upper Cretaceous chalk and Cenozoic mud rocks of the Sable Subbasin, Canadian Atlantic margin, *Marine and Petroleum Geology* 21, p. 1205–1219.
- Ings, S. J. and J.W. Shimeld, 2006, A new conceptual model for the structural evolution of a regional salt detachment on the northeastern Scotian margin, offshore Eastern Canada, *AAPG Bulletin*, v. 90, no. 9, p. 1407 - 1423.
- Jansa, L.F. and J.A. Wade, 1975a, Paleogeography and sedimentation in the Mesozoic and Cenozoic, southeastern Canada; in Canada's Continental Margins and Offshore Petroleum Exploration, ed. C.J. Yorath, E.R. Parker and D.J. Glass; *Canadian Society of Petroleum Geologists*, Memoir 4, p.79-102.
- Jansa, L.F. and J.A. Wade, 1975b, Geology of the continental margin off Nova Scotia and Newfoundland; in Offshore Geology of Eastern Canada, *Geological Survey of Canada*, Paper 74-30, v.2, p. 51-106.
- Keen, C.E., A. Cordsen, 1981, Crustal structure, seismic stratigraphy, and rift processes of the continental margin off eastern Canada; ocean bottom seismic refraction results off Nova Scotia; *Canadian Journal of Earth Sciences*, v. 18, p. 1523-1538.

- Keen, C.E., M.J., D.L. Barrett, and D.E. Heffler, 1975, Some aspects of the ocean-continental transition at the continental margin of eastern North America; in *Offshore Geology of Eastern Canada*, v. 2, Regional geology, ed. W.J.M. van der Linden and J.A. Wade; *Geological Survey of Canada*, Paper 74-30, v. 2, p.189-197.
- Kidston, A.G., D.E. Brown, B. Altheim, and B.M. Smith, 2002, Hydrocarbon Potential of the Deepwater Scotian Slope, *Canada-Nova Scotia Offshore Petroleum Board*, Halifax, CD-ROM, p. 111,
(Also: http://www.cnsopb.ns.ca/Whatsnew/Hydrocarbon_Potential_Scotian_Slope.pdf)
- Kidston, A.G., D.E. Brown, B.M. Smith, B. Altheim, 2005, The Upper Jurassic Abenaki Formation Offshore Nova Scotia: A Seismic and Geologic Perspective, *Canada-Nova Scotia Offshore Petroleum Board*, Halifax, Nova Scotia, p. 168.
- Margrave, G. F., 1998, Direct Fourier Migration for Vertical Velocity Variations, *CREWES Research Report*, v. 10.
- McIver, N.L., 1972, Cenozoic and Mesozoic Stratigraphy of the Nova Scotia Shelf, *Canadian Journal of Earth Sciences*, v.9, p.54-70 (1972).
- Mikulich, W., and D. Hale, 1992, Steep-dip $v(z)$ imaging from an ensemble of Stolt-like migrations: *Geophysics*, 57, 51-59.
- Neidell, N. S., and M.T. Taner, 1971, Semblance and other coherency measures for multichannel data: *Geophysics*, 36, 482-497.
- Newman, P., 1973, Divergence effects in a layered earth: *Geophysics*, 38, p. 481-488.
- Officer, C.B., and M. Ewing, 1954, Geophysical investigations in the emerged and submerged Atlantic Coastal Plain, Part VII. Continental Shelf, continental slope and continental rise south of Nova Scotia; *Bulletin of the Geological Society of America*, v. 65, p. 653-670.
- Peacock, K. L., and S. Treitel, 1969, Predictive deconvolution- Theory and practice. *Geophysics*. 34, p. 155-69.
- Randen, T., S.I. Pedersen, and L. Sonneland, 2001, Automatic extraction of fault surfaces from three-dimensional seismic data. Expanded Abstr., Int. Mtg., *Soc. Exploration Geophys*, p. 551-554.
- Robinson, B., 2000, GEPH316 Seismic Data Processing, *Field Data Workshop 2000*, Lancaster University.
- Robinson, E. A. 1983, Migration of Geophysical Data, Boston International Human Resources Development Corp.

- Sacrey, D., R. Roden, 2014, Understanding Attributes and Their Use in the Application of Neural Analysis-Case Histories Both Conventional and Unconventional, *Search and Discovery Article #41473* (2014)*, Posted October 27, 2014, AAPG©2014.
- Sampson, A., 2012, A seismic attribute study to assess well productivity in the Ninilchik Field, Cook Inlet Basin, Alaska, *Master Thesis*, Louisiana State University and Agricultural and Mechanical College.
- Sayers, J. E., 2013, Enhancement of the Geological Features of the Scotian Basin by the Application of Spectral Inversion, Offshore Nova Scotia, , Master Thesis, Faculty of the Department of Earth and Atmospheric Sciences.
- Sheriff, R. E., 1984, Encyclopedic Dictionary of Exploration Geophysics, 2nd Edition, Tulsa: *Society of Exploration Geophysicists*, pp. 323.
- Sheriff, R.E., 2004, what is Deconvolution? , *Search and Discovery Article #40131*.
- Shimeld, J., 2004, A comparison of salt tectonic subprovinces beneath the Scotian Slope and Laurentian Fan, 24th Annual GCS-SEPM Foundation Bob F. Perkins Research Conference, Houston, p. 291-306.
- Smith, B.M., C. Makrides, K. Kendell, 2015, Call for Bids NS15-1 – Exploration history, geologic setting, and exploration potential: Eastern Region, CNSOPB Geoscience Open File Report, 2015-002MF, 32 p.
- Stolt, R.H., 1978, Migration by Fourier transform: *Geophysics*, 43, 23-48.
- Stolt, R.H. and A.K. Benson, 1986, Seismic migration: theory and practice: Geophysical Press.
- Taner, M.T., 1979, Complex seismic trace analysis. *Geophysics*, v. 44, n. 6, p. 1041-1063.
- Taner, M.T., 2001, Seismic attributes. CSEG Recorder, v. 26, n. 7, p. 49-56.
- Taner, M. T., and F. Koehler, 1969, Velocity spectra – digital computer derivation and applications of velocity functions: *Geophysics*, 34, p. 859–881.
- Thomas, B., 1999, 2D Seismic data processing with Seismic Unix, Michigan Technological University, p. 206.
- Thomsen, 1986, Weak Elastic Anisotropy, *Geophysics*, v. 51, No.10.

- Wade, J. A., 1990, Chapter 5 - The geology of the southeastern margin of Canada, Part 1: The stratigraphy of Georges Bank Basin and relationships to the Scotian Basin. In: M.J. Keen and G.L. Williams (Eds.), *Geology of the continental margin of eastern Canada*, Geological Survey of Canada, Geology of Canada No.2, pp.167-190. (Also Geological Society of America, *The Geology of North America*, v. I-1.
- Wade, J.A., D.E. Brown, R.A. Fensome, and A. Traverse, 1996, The Triassic Jurassic Fundy Basin, Eastern Canada: regional setting, stratigraphy and hydrocarbon potential. *Atlantic Geology*, v. 32, no.3, p. 189-231.
- Welsink, H.J., J.D. Dwyer., and R.J. Knight, 1989, Tectono-Stratigraphy Passive Margin Off Nova Scotia. In: A. J. Tankard and J. R. Balkwill (Eds.), *Extensional Tectonics and Stratigraphy of the North Atlantic Margins*, *American Association of Petroleum Geologists*, Memoir 46, p. 215-231.
- Yilmaz, O., 1987, *Seismic Data Analysis 2-Processing, Inversion and Interpretation of Seismic Data*, *Society of Exploration Geophysicists*.
- Zhou, H.W., 2014, *Practical Seismic Data Analysis*, 1. Seismology – Textbooks. I. Title, ISBN 978-0-521-19910-0.

VITA

Fulya Gizem YAGCI was born in Kocaeli, Turkey, in 1990. She is graduated from Istanbul University, in the Department of Geophysical Engineering in June 2012 and earned her B.S. She joined the internship program of Turkish Petroleum Corporation and completed the internship in August 2011.

She earned a scholar ship from Turkish Petroleum Corporation after graduating from Istanbul University and completed her language program in Houston ELS. She started her master program in Missouri University of Science and Technology in January 2014 in Rolla, Missouri. She studied marine seismic data processing with 2-D seismic profiles from Penobscot, Scotian Basin, Nova Scotia. She received her Master of Science degree in Geology and Geophysics from the Missouri University of Science and Technology in May 2016.